

# **Final Report**

# Research Title: Mathematical Modeling of Electro-Magneto-Hydrodynamics Enhanced Flow and Heat Transfer in Heat Exchangers

Assoc. Prof. Dr. Nat Kasayapanand

**Project Code: RSA5280035** 

## **Final Report**

# Research Title: Mathematical Modeling of Electro-Magneto-Hydrodynamics Enhanced Flow and Heat Transfer in Heat Exchangers

Assoc. Prof. Dr. Nat Kasayapanand (King Mongkut's University of Technology Thonburi)

Supported by the Thailand Research Fund
(The detail in this report is the researcher's opinion; it does not necessarily agree by the Thailand Research Fund)

Project Code: RSA5280035

Research Title: Mathematical Modeling of Electro-Magneto-Hydrodynamics

Enhanced Flow and Heat Transfer in Heat Exchangers

Investigator: Assoc. Prof. Dr. Nat Kasayapanand

(King Mongkut's University of Technology Thonburi)

E-mail Address: nat.kas@kmutt.ac.th

Project Period: March 2009 - March 2012

#### **ABSTRACT**

The objective of this research is to generate mathematical modeling of combination between magnetic field, electric field, flow field, and temperature field. Moreover, this research is to create computer program for calculating air velocity profiles and temperature distributions through the heat exchangers by coupling between magnetohydrodynamics, electrohydrodynamics, and extended surface techniques. The effect of all concerning parameters to the heat transfer coefficient are analyzed such as primary fluid velocity, geometry and dimension of the extended surface, intensity of magnetic field, magnetic pole arrangement, number of magnetic pole, supplied voltage at wire electrode, electrode arrangement, distance between wire electrodes, etc. Finally the superposition between magnetohydrodynamics, electrohydrodynamics, and extended surfaces techniques is obtained.

Keywords: Computational fluid dynamics; Electric field; Heat transfer enhancement; Magnetic field; Mathematical modeling

รหัสโครงการ: RSA5280035

ชื่อโครงการ: แบบจำลองทางคณิตศาสตร์ของการเพิ่มความสามารถในการถ่ายเทความ

ร้อนโดยใช้สนามไฟฟ้าร่วมกับสนามแม่เหล็กในอุปกรณ์แลกเปลี่ยนความ

ร้อน

ชื่อนักวิจัย: รศ. ดร. ณัฏฐ์ กาศยปนันทน์

(มหาวิทยาลัยเทคโนโลยีพระจอมเกล้าธนบุรี)

E-mail Address: nat.kas@kmutt.ac.th

ระยะเวลาโครงการ: มีนาคม 2552 – มีนาคม 2555

#### บทคัดย่อ

งานวิจัยนี้เป็นการสร้างแบบจำลองทางคณิตศาสตร์ของผลเนื่องจากสนามแม่เหล็ก สนามไฟฟ้า สนามการไหล และสนามอุณหภูมิ และสร้างโปรแกรมคอมพิวเตอร์เพื่อคำนวณความเร็วและอุณหภูมิ ของอากาศที่ไหลผ่านอุปกรณ์แลกเปลี่ยนความร้อนโดยวิธีการคำนวณพลศาสตร์ของไหลของ สนามแม่เหล็กและสนามไฟฟ้าร่วมกับเทคนิคการเพิ่มพื้นที่ผิว วิธีที่มีต่อการพาความร้อนแบบ ธรรมชาติและแบบบังคับ ความสัมพันธ์ระหว่างสนามไฟฟ้า สนามการไหล และสนามอุณหภูมิ ผล ของปัจจัยต่าง ๆ ที่มีต่อการไหล การกระจายอุณหภูมิ และการถ่ายเทความร้อนของอุปกรณ์ แลกเปลี่ยนความร้อนแบบติดครีบที่วิเคราะห์ได้แก่ ขนาด รูปร่าง จำนวน และการจัดวางครีบ เงื่อนไข ที่ขอบของครีบ ปริมาณความร้อนที่ถ่ายเท ความเร็วและทิศทางการไหล คุณสมบัติของของไหล ขนาดแรงดันไฟฟ้า ความเข้มของสนามแม่เหล็ก การจัดวางอิเลคโทรดและขั้วแม่เหล็ก ผลการวิจัยพบว่า สนามการไหลและสนามอุณหภูมิของของไหลได้รับผลกระทบ จากสนามไฟฟ้าและสนามแม่เหล็กโดยเฉพาะกรณีที่ความเร็วต่ำ การเพิ่มความสามารถในการถ่ายเท ความร้อนขึ้นกับ รูปร่าง จำนวน และการจัดวางครีบ รวมทั้งจำนวนและการจัดวางอิเลคโทรดและ สนามแม่เหล็ก นอกจากนี้ยังพบว่า ปริมาตรการไหลรวมทั้งค่าสัมประสิทธิการถ่ายเทความร้อนสูงสุด เกิดขึ้นเมื่อจำนวนอิเลคโทรดมีค่าเหมาะสม

คำสำคัญ: การคำนวณพลศาสตร์ของไหล; แบบจำลองทางคณิตศาสตร์; สนามไฟฟ้า; สนามแม่เหล็ก; การเพิ่มความสามารถในการถ่ายเทความร้อน

# **ACKNOWLEDGEMENTS**

The author gratefully acknowledges the financial support provided from the Thailand Research Fund for carrying out this study.

# **CONTENTS**

	Page
English Abstract	2
Thai Abstract	3
Acknowledgements	4
Contents	5
Nomenclature	7
Chapter	
1. Introduction	11
1.1 State of Problems and Background	11
1.2 Objectives	12
1.3 Scopes	12
1.4 Expected Benefit	12
2. Literature Review	13
2.1 Overview	13
2.2 Experimental Researches	18
2.3 Mathematical Researches	27
3. Theoretical Analysis	44
3.1 Fluid Dynamics	44
3.2 Electrostatic	46
3.3 Heat Transfer Characteristic	47
3.4 Grid Generation	47
3.5 General balance laws	51
3.6 Constitutive Equations	54
3.7 Non-Linear Electro-Magneto-Hydrodynamics Model	60

	Page
4. Research Methodology	63
4.1 Research Procedure	63
4.2 Numerical Procedure	63
4.3 Experimental Setup	65
5. Results and Discussion	67
5.1 Channel Configuration	67
5.2 Enclosure Configuration	112
5.3 Open Vertical Channel Configuration	136
5.4 Open Cavity Configuration	150
6. Conclusion and Recommendation	166
6.1 Conclusion	166
6.2 Recommendation	167
7. Output from the Research	168
References	169
Appendix	181

# NOMENCLATURE

Symbol		Unit
AR	aperture size $(a/H)$	
AH	aperture position $(b/H)$	
В	$(= \mu_0(H + M))$ , magnetic flux density	$kg/A/s^2$
$c_p$	specific heat	$J/kg \cdot K$
d	$(=\frac{1}{2}(\nabla v + (\nabla v)'))$ , average rate of deformation tensor	1/s
$\frac{\mathrm{D}}{\mathrm{Dt}}$	$(=\frac{\partial}{\partial t} + \mathbf{v} \cdot \nabla)$ , material derivative	1/s
D	$(=\varepsilon_0 E + P)$ , electric displacement vector	$A s/m^2$
D	diameter	m
$D_e$	charge diffusion coefficient	$m^2/V \cdot s$
$D_p$	charged particle diffusion coefficient	$m^2/s$
Ê	$(=E+v\times B)$ , electromotive intensity	kg m/s <sup>3</sup> /A
$\boldsymbol{E}$	electric field strength	V/m
f	mechanical body force per unit mass	$m/s^2$
$f_D$	aerodynamic drag force	$N/m^3$
$f_u$	under relaxation factor	
$\boldsymbol{F}_{E}$	electrohydrodynamic body force	$N/m^3$
$\boldsymbol{g}$	acceleration due to gravity	$m/s^2$
Gr	Grashof number	
h	heat transfer coefficient	$W/m^2 \cdot K$
H	height	m
Н	magnetic field intensity	A/m
I	unit tensor	
$oldsymbol{J}$	current density	$A/m^2$
k	thermal conductivity	$W/m{\cdot}K$
$l_w$	length between wire electrodes	m
L	channel length	m
m	total mass flux	kg/s

M	total magnetization per unit volume	A/m
$\hat{\boldsymbol{M}}$	$(= M + v \times P)$ , magnetomotive intensity	A/m
n	normal direction to the surface	
$N_e$	number of electrodes	
$N_f$	number of fins	
Nu	Nusselt number	
P	pressure	$N/m^2$
P	total polarization per unit volume	$A s/m^2$
Pe	Peclet number	
Pr	Prandtl number	
q	electric charge density	C/m <sup>3</sup>
$q_h$	heat flux	$W/m^2$
q	conduction heat flux	kg/s <sup>3</sup>
Q	heat transfer rate	W
r	corona wire radius	m
Ra	Rayleigh number	
Re	Reynolds number	
S	entropy per unit mass	$m^2/kg/K/s^2$
S	source term in ion continuity equation	$C/m^3 \cdot s$
t	time	S
t	$(= \varphi \mathbf{I} + \tau)$ , Cauchy stress tensor	$kg/m/s^2$
T	temperature	K
û	internal energy per unit mass	$m^2/s^2$
$u_e$	electric characteristic velocity	m/s
$U_i$	inlet air velocity	m/s
v	fluid velocity	m/s
V	voltage	V
X	Cartesian coordinates	m
у	Cartesian coordinates	m
W	width	m

# Greek symbols

α	thermal diffusivity	$m^2/s$
β	volume expansion coefficient	1/K
β	$(=\varepsilon_0\mu_0V^2)$ , square of electro-magnetic Mach number	
$\mathcal{E}$	fluid permittivity	F/m
$\mathcal{E}$	electric permittivity	$s^4 A^2/kg/m^3$
$\mathcal{E}_0$	$(=8.854\times10^{12})$ , electric permittivity of vacuum	$s^4 A^2/kg/m^3$
$\mathcal{E}_{\mathrm{p}}$	$(=\varepsilon_0\chi_{\rm e})$ , polarization electric permittivity	$s^4 A^2/kg/m^3$
$\mathcal{E}_{ ext{kml}}$	permutation symbol	
γ	ratio of electric current	
η	curvilinear coordinate	m
λ	wave length	m
μ	dynamic viscosity	kg/m/s
$\mu_t$	turbulent viscosity	kg/m/s
$\varphi$	modified hydrostatic pressure	kg/m/s <sup>2</sup>
$\phi$	inclined angle	degree
ν	kinematics viscosity	$m^2/s$
$\theta$	dimensionless temperature	
ρ	density	kg/m <sup>3</sup>
$\sigma_{\!e}$	electrical conductivity	1/ohm⋅m
τ	period	
τ	deviator part of stress tensor	kg/m/s <sup>2</sup>
μ	magnetic permeability	$kg m/A^2/s^2$
$\mu_0$	$(=4\pi \times 10^{-7})$ , magnetic permeability of vacuum	$kg m/A^2/s^2$
$\mu_{ m r}$	$(=\mu/\mu_0)$ , relative magnetic permeability	
$\mu_{\mathrm{m}}$	$(=\mu_0\chi_{\rm B})$ , magnetization magnetic permeability	$kg m/A^2/s^2$
$\omega$	relaxation factor	
ω	vorticity	1/s
ξ	curvilinear coordinate	m

 $\chi_{\rm B} = (= 1 - \mu_{\rm r}^{-1})$  , magnetic susceptibility based on B

 $\chi_{\rm e} = (= \varepsilon_{\rm r} - 1)$ , electric susceptibility

 $\psi$  stream function m<sup>2</sup>/s

 $\psi = (= \hat{\mu} - T s - \hat{E} \cdot P / \rho)$ , generalized Helmholtz energy per unit mass  $m^2/s^2$ 

## Subscripts

- 0 without electric field
- a ambient

EHD based on electrical velocity

- g glass
- *i* indical notation of tensor
- k indical notation of tensor
- L lower subchannel
- U upper subchannel

new updated value

- *m* mean value
- p charged particles
- P at the grounded plate
- t turbulent
- w wall surface

## Superscripts

- *n* iteration number
- \* adjusted value

## CHAPTER 1 INTRODUCTION

### 1.1 State of Problems and Background

Heat exchangers are the key elements in many heat transfer processes and it has been extensively investigated during the past many decades in an effort to develop more economical and efficient unit. However, Heat exchanger is limited in its thermal performance characteristics due to its effectiveness. The strategies to achieve considerable heat transfer improvement are to use extended area by attaching fins, modify flow patterns, or increase fluid velocity. With these techniques, higher pressure drop of fluid flow is obtained and the producing and operating cost is also augmented. The enhancement technique utilizing electric field, which is based on electrostatic force due to space charge or polarization of dielectric fluid, can be one of the most promising methods among various active techniques because of its several advantages. For example, quick responses to control the flow, significant increase in heat transfer rate with very low pressure drop, and small consumption of electric power. Moreover, the advent of superconducting materials paves the way to produce a very strong magnetic field in the laboratory. Extensive investigations are underway to probe the fluid flow and heat transfer of an engineering system under substantial magnetic influence. The behavior of an electrically conducting fluid subjected to the Lorentz force, which leads to magnetohydrodynamics, has been widely studied. However, there is no previous literature relating with the coupling between electro- and magneto-hydrodynamics on the flow and heat transfer enhancements.

The objectives of this research are to determine the flow patterns and the temperature distributions of air flowing through the extended surfaces under magnetic and electric fields and to analyze the effect of all concerning parameters to the heat transfer coefficient such as primary fluid velocity, geometry and dimension of the extended surface, intensity of magnetic field, magnetic pole arrangement, number of magnetic pole, supplied voltage at wire electrode, electrode arrangement, distance between wire electrodes, etc. Finally the optimized heat exchanger design of the superposition between magnetohydrodynamics, electrohydrodynamics, and extended surfaces techniques is obtained.

### 1.2 Objectives

- 1.2.1 To determine the flow patterns and the temperature distributions of air flowing through the extended surfaces under magnetic and electric fields.
- 1.2.2 To analyze the effect of all concerning parameters to the heat transfer coefficient such as primary fluid velocity, geometry and dimension of the extended surface, intensity of magnetic field, magnetic pole arrangement, number of magnetic pole, supplied voltage at wire electrode, electrode arrangement, distance between wire electrodes, etc.
- 1.2.3 To find out the optimized heat exchanger design of the superposition between magnetohydrodynamic, electrohydrodynamics, and extended surfaces techniques.

### 1.3 Scopes

- 1.3.1 This research considers the air as a working fluid.
- 1.3.2 The fluid is single phase flow and the physical properties are assumed to be constant.
- 1.3.3 Flow characteristics are laminar, incompressible, and viscous.
- 1.3.4 The corona discharge occurs only in the vicinity around the wire electrode.
- 1.3.5 The effect of magnetic field is considered.

#### 1.4 Expected Benefit

- 1.4.1 The theoretical modeling can be developed for the future applications.
- 1.4.2 The obtained results can be applied to design electrohydrodynamics and magnetohydrodynamics heat exchanger.

## CHAPTER 2 LITERATURE REVIEW

#### 2.1 Overview

The extended surfaces such as fin, rib, or curved surface are always applied to increase the heat flow per unit of basic surface. The analysis of a continuous plate fin pierced by a regularly spaced array has many engineering applications. In order to simplify the problem considered, the calculation of the standard fin efficiency usually assumes that the heat transfer coefficient is constant over the plate fin. Zabronsky [1] applied the method to obtain the fin efficiency under the assumption of the uniform heat transfer coefficient. However, it is well known that there exists a very complex flow pattern within a plate finned-tube heat exchanger due to its three-dimensional nature and flow separations. For smooth finless circular tube, the fully developed combined forced and free convection had been solved analytically by Morton [2] and investigated numerically by Kemeny and Somers [3]. A classification of natural, forced, and mixed convection regimes were conducted by Metais and Eckert [4]. Initial investigations of mixed convection heat transfer were made on horizontal and inclined plates. Later studies were extended to parallel plates and then to the flow in channels. The study of forced convective heat transfer by Mori and Uchida [5] was being regarded as one of the first studies made on horizontal flat plates. From their theoretical and experimental investigations, they concluded that for sufficiently high temperature differences between the plates the flow became three-dimensional caused by vortex rolls. It was also found that these vortex rolls increased the Nusselt number. Buoyancy effects were included by Cheng et al. [6] in a numerical study of laminar forced convection in horizontal rectangular channels. They reported that the buoyancy effect was negligible up to a certain entry length depending on the magnitude of the Rayleigh number. Saboya and Sparrow [7] and Sparrow et al. [8] demonstrated that there exists the great variation of the heat transfer rate on the fin and tube heat exchanger. The demand for greater compactness was accompanied by a corresponding increase in volumetric and surface power dissipation. There was therefore a current call to pursue better configurations in order to maximize heat transfer rate. In spite of the constant pressure for more efficient heat transfer devices based on known techniques such as natural convection inside a cavity, very few literatures deal with optimization of thermal performance [9]. The flow accelerates around the tube and forms a low-velocity wake region behind the tube. This causes local variations of the heat transfer coefficient, as shown in [10]-[13]. Experiments were performed by [14]-[16] in order to determine the effects of free convection on laminar forced convection flow between horizontal parallel plates under symmetrical and asymmetrical heating conditions. Their experimental measurements showed that the flow at the top was characterized by laminar forced convection, however, conditions at the bottom plate were strongly influenced by buoyancy induced flow. As a result of this buoyancy driven flow, mixed convection coefficients exceeded those associated with pure forced convection by as much as a factor of seven. Although buoyancy effects could significantly enhance heat transfer for laminar forced convection flows, enhancement was typically negligible if the forced flow was turbulent. In order to calculate the heat transfer coefficient of fluid, the longitudinal variation of the Nusselt number was characterized by a decaying oscillation [17]-[18]. Most of the finned research found is of descriptive nature [19]-[20], in none of them, heat transfer augmentation under global constraints was the main concern. Liou et al. [21] performed both the numerical analysis and experimental studies to investigate the heat transfer and fluid flow behavior in a rectangular channel flow with stream wise periodic ribs mounted on one of the principal walls. They concluded that the flow acceleration and the turbulence intensity were two major factors influencing the heat transfer coefficient. The behavior of such finned-enclosure self-driven flows had been reported analytically, experimentally and numerically in several articles [22]-[24]. Chen and liou [25] and Fabbri [26] conducted the numerical method to calculate the optimal aspect ratio of plate fin heat exchanger. Rau et al. [27] experimentally found the optimum pitch to rib height ratio. Hence, these investigations reveal that not only the rib geometry but also its geometrical arrangement play a vital role in enhancing the heat transfer coefficient. The results of optimal fin array were numerically investigated again by [28]-[29]. The applications of adding finnedsurface were found in channel or solar air heater such as [30]-[33]. Lin et al. [34]-[35] used the finite-difference method in conjunction with the linear least-squares scheme to estimate the space-variable heat transfer coefficient on a heated cylinder normal to the laminar and turbulent air streams. Owing to the requirement of the local fin temperature measurements, the estimations of the local heat transfer coefficients on the plate fin under steady-state heat transfer conditions are generally more difficult than that on the boundary surface of a physical geometry. The experimental study [36] in this area has been carried out but very

few attempts of numerical investigation have been made so far due to complexity of flow pattern and computational limitations. An attempt is made to predict numerically the details of both the velocity and temperature fields responsible for heat transfer enhancement. The presence of rib may enhance heat transfer because of interruption of the viscous sub layer, which yields flow turbulence, separation and reattachment leading to a higher heat transfer coefficient. The enhancement of heat transfer by flow separation and reattachment caused by ribs is significantly higher compared to that by the increased heat transfer area due to ribs [37]. Numerical and Experimental works of a design for inserting the extended surface in channel were conducted again by [38]-[41]. Marin et al. [42] and Heggs and Ooi [43] demonstrated that the charts for radial rectangular fins can been used to predict the fin performance ratio for polygon fins. Furthermore, the optimization of fin design is continuously developed by many researchers [44]-[59]. However, there is no previous literature dealing with the electrohydrodynamic or magnetohydrodynamic enhancement of heat transfer coupling with the extended surface technique.

Air as a paramagnetic gas is subjected to a magnetic body force in a gradient magnetic field. Wakayama [60] and Wakayama and Sugie [61] studied the magnetic control of gas flow and combustions. Gray et al. [62] investigated the physics of this magnetic body force and obtained the numerical similarity solutions for the twodimensional plums driven by the interaction of a line heat source and a non-uniform magnetic field. Huang et al. [63,64] studied the stability of the paramagnetic field layer by the action of a non-uniform magnetic field. It is useful to note that all the above studies dealt with the magnetothermal convection in a magnetic dual-pole field. As compared to the magnetic dual-pole, the magnetic quadrupole can efficiently utilize the available magnetic field energy and the dependence of the magnetic force on position is highly regular, so it is commonly used in high gradient magnetic separation (HGMS) and ion cyclotron resonance (ICR). Yang et al. [65] numerically studied the air free convection induced by a magnetic quadrupole field under microgravity and indicated that free convection induced by the centrifugal-form magnetic force presents different flow and heat transfer behavior from the gravitational natural convection. Braithwaite et al. [66] considered facilitation or suppression of buoyancy-driven convection by use of a magnetic field. Wakayama [67,68] demonstrated the analogousness of the roles of magnetizing force and conventional gravity force, which can be utilized to enhance the overall convective heat transfer. Similarly, Tagawa et al. [69-71] presented complete mathematical

formulations for flow of a non-conducting fluid, which include the magnetizing force. A brief scan of these previous efforts [66-71] asserts that the magnetizing force can indeed be utilized like the gravity force, and the global fluid system may be effectively controlled by imposing a magnetic field. The majority of preceding studies have dealt with the steadystate situations. The response of the fluid system to time-dependent magnetizing effect has not been fully examined. This issue is significant from the standpoint of heat transfer enhancement. In ordinary gravity-driven natural convection of a nonmagnetized fluid system, it has been shown that heat transfer augmentation is possible by choosing an appropriate value of frequency in the externally applied time-dependent boundary conditions [72-78]. The crux of the argument is that the convective heat transfer is maximized when a characteristic frequency of the system is excited. This can be accomplished by tuning in a proper value of the forcing frequency of the time-dependent, externally controllable boundary temperature variations. This represents resonance of the system [72-74], and the task is to identify the characteristic frequencies of the system. In the case of a gravity-driven buoyant convection of a non-magnetized fluid at large Rayleigh number, the basic characteristic frequency has been shown to be the internal gravity oscillations [75-78]. The analysis was shown to be consistent with the numerical predictions.

There are some earlier studies relating to the effect of the ionic wind in electrostatic field. In a forced convection field, the EHD induced flow takes place owing to the interaction between the ionic wind and the primary flow increases the convective heat transfer coefficient from the wall surface. Several models have been proposed for the calculation of the electric field and charge density distribution in a wire-plate precipitation system using the finite difference method [79]. Yabe et al. [80] investigated the phenomenon of a corona wind between wire and plate electrodes and found that the interaction between ionic wind and primary flow increased the heat transfer from a wall surface. Velkoff and Godfrey [81] conducted heat transfer over a horizontal flat plate using parallel wire electrodes. The ionic wind promoted mixing of the primary flow, resulting in an increase of the heat transfer coefficient. The mathematical modeling in the electrostatic precipitators was developed by Lawless and Sparks [82]. A computational method applied to an electrostatic precipitator was reported by Yamamoto and Velkoff [83]. The main drawback of the finite difference method is the difficulty in the construction of the computational grid, which should be orthogonal to avoid complexity of the equations, and

also must be significantly finer than the wire radius to produce grid-independent results, especially near the wire [84]. Lean and Domoto [85] investigated the model of the physical of charge transport in steady Navier-Stroke's flow by using a novel algorithm that considered full coupling of the electrostatic and fluid equations and was applicable to arbitrary geometries. Franke and Hogue [86] studied heat transfer from horizontal tube with the corona discharge. The reviewed of past work of EHD enhancement heat transfer in single and two-phase heat transfer was investigated by Allen and Karayiannis [87]. Governing equations of electric field, flow field, and temperature field were also included. Goo and Lee [88] developed the numerical scheme to estimate more exactly the collection efficiency of particles in the wire-plate electrostatic precipitator (ESP). The involved physical phenomena such as corona field, turbulent EHD flow field, particle charging, and turbulent motion of particles were treated simultaneously. Tada et al. [89] studied the theoretical analysis on the enhancement of forced convection heat transfer by applying an electric field. Computational domain was performed in the channel flow where a series of wire electrodes were installed in parallel with the primary flow direction, or installed at right angle to the primary flow direction. It was found that the phenomenon was also performed taking account of momentum transfer between ions and neutral fluid molecules. A mathematical model of electric field strength and space charge density in the ESP was developed by Lami et al. [90]. Talaie et al. [91] presented a new computational scheme that was developed to evaluate current-voltage characteristics of a wire-plate high voltage configuration system applicable for single-stage ESP. Rafiroiu et al. [92] presented an analysis of the corona field for such electrode arrangements. A corona wind associated with a non-ionizing metallic tube connected to the high voltage and facing a grounded plane was an electrode arrangement frequently encountered in electrostatic processes. Anagnostopoulos and Bergeles [93] proposed a numerical simulation methodology for calculating the electric field in wire-duct precipitation systems by using finite differencing in orthogonal curvilinear coordinates to solve the potential equation. Charge density distributions were obtained by the method of characteristics or using a predictioncorrection scheme. Recently, the numerical results of EHD enhanced heat transfer of air flowing were investigated by [94]-[107].

The recently literatures can be grouped in the experimental works and the theoretical works. The details of distinct literatures are described as the followings;

#### 2.2 Experimental Researches

Yabe [108] proposed the characteristics of active heat transfer enhancement technique by applying electric field. Also described were the EHD body force, corresponding governing equations and boundary conditions of EHD phenomena, as well as the relaxation time of an electric charge as shown in Fig. 2.1. Furthermore, the present state of research on EHD heat transfer enhancement techniques was systematically described from the EHD viewpoint. It was found that the convective heat transfer coefficients (with an EHD liquid jet) were enhanced by a factor of over 100 compared to the natural convection heat transfer coefficients. Maximum heat transfer coefficients, exceeding 10<sup>4</sup> W/m<sup>2</sup>K, were related to not only by the forced convection of EHD liquid jet but also by the turbulent heat flux due to its turbulent intensity.

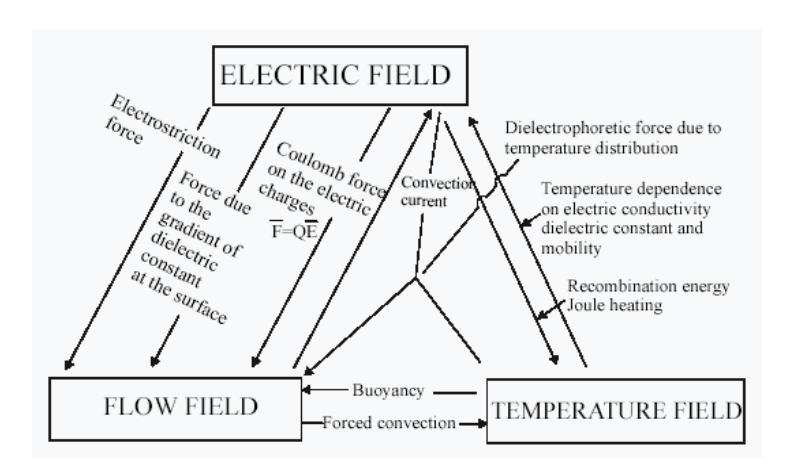


Fig. 2.1 Interactions among electric field, flow field, and temperature field [108].

Ishiguro [109] studied the augmentation effect of EHD induced flow disturbance on forced convection heat transfer in a channel. The applicability of the enhanced heat transfer was determined in a low pressure drop heat exchanger, such as high performance oil cooler. The investigation was mainly based on the study carried out on the unique point where the flow was disturbed actively and controllably by applying electric field between the wall and array of wire electrodes installed near the wall along the main stream. The liquid mixture of R-113 and ethanol was selected in the turbulent flow as well as in the laminar flow, up to a factor of about twenty-three in the case of laminar flow. It was noted that the rate of increase in heat transfer coefficient is larger compared to that in the

pressure drop. From a measurement of velocities by a laser Doppler velocimeter, it was made clear that the EHD brings about large heat transfer coefficients.

Cooper [110] involved in the design of EHD enhanced evaporators, in particular the choices of electrodes and heat transfer surface geometries in Figs. 2.2 and 2.3. For maximum enhancement, the high voltage electrode geometry should be designed such that the maximum field strength was obtained at the heat transfer surface and not in other parts of the system. In addition, heat transfer surface geometry should be such that electric field in homogeneity was maximized in the immediate vicinity of the surface. The presence of intense electric field within the dielectric fluid raised the issue of possible fluid breakdown or chemical charges over prolonged periods of operation.

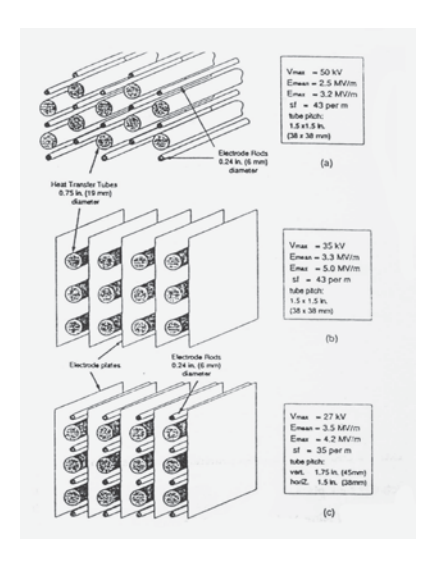


Fig. 2.2 Electrode configurations applicable to EHD shell-and-tube heat exchangers [110].

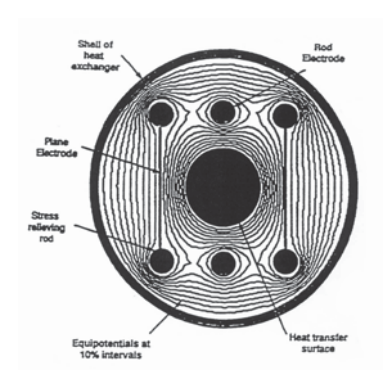


Fig. 2.3 Electric field distributions on a single-tube shell-and-tube heat exchanger [110].

Ogata et al. [111] studied the utilization of EHD boiling augmentation in a tube bundle as shown in Fig. 2.4. R-11 and HCFC-123 were used in this research work. In this test, the boiling heat transfer at a supplied voltage of 18 kV was found to be more than seven times higher than that without an electric field. Moreover, it was found that EHD augmentation of boiling heat transfer in a tube bundle has as effective as in a single tube. The cost calculations suggested that the cost of EHD evaporators is 20-30 % lower than the course of conventional evaporators using low finned or porous tube.

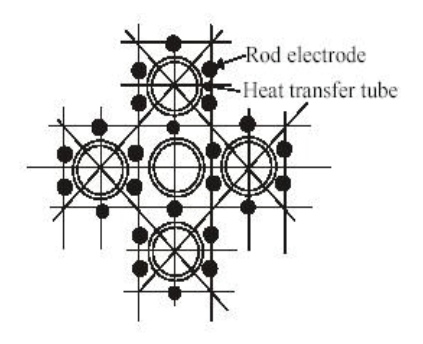


Fig. 2.4 Electrode arrangement around the tube bank [111].

Yeh and Lin [112] investigated the theoretical and experimental work of an effect of collector aspect ratio to the collector efficiency of fiat-plate solar air heater. It was found that with constant collector area, the collector efficiency increases when the collector aspect ratio increases. The theoretical predictions agree reasonably well with experimental results

Allen and Karayiannis [113] reviewed the past work of EHD enhancement heat transfer in single and two-phase heat transfer. Governing equations of electric field, flow field, and temperature field were also included. The three major ways in which EHD can enhance single phase convective heat transfer were corona wind, electrophoresis, and dielectric phoretic forces. It was found that corona wind and electrophoresis gave the highest enhancement ratio, although consideration must be given in the former case to the power consumption and in the latter to the purity and polarity of the medium. A description of the possible practical EHD electrode systems for applications was also presented.

Singh [114] experimentally investigated the EHD technique for in-tube condensation heat transfer enhancement of R-134a. The test section consisted of a horizontally mounted tube-in-tube heat exchanger with refrigerant flowing in the inner tube and water flowing in the outer tube, smooth and microfin copper tubes were tested. Six different electrodes representing various electrode diameters and electrode spacing were used in the apparatus. Up to 640 % improvement in condensation heat transfer coefficient was obtained with the optimum electrode at a maximum EHD power consumption of only 0.08 % of the condenser capacity. The optimum tubes for internal condensation were found to be smooth tubes.

Hachemi [115] introduced the interaction of radiation combined to convection heat transfer. In this effect a flat-plate and two fanned system collectors were selected. The channel back of these collectors was coated in turn by three coverings. In the first a wooden plate only which was the channel back of the collector, in the second and third time a reflecting and a black-painted covering were used, respectively. These were put down on the channel back of collector. The black-painted coating when it was used in the three collectors gives the better improvement followed by the reflecting covering in relation to their respective collectors having uncoated channel back. The greater relative increase of thermal performance was obtained when the flat-plate collector was used and where its channel back was recovered by a black-painted coating.

Karayiannis [116] experimentally studied the heat transfer enhancement of R-132 and R-11 in a shell and tube heat exchanger by using electric field. The test apparatus consisted of five copper tubes as the heat source and four wire electrodes placed around each tube. The range of supplied voltage was 0-25 kV and the heat flux was 5-20 kW/m². It was found that the heat transfer enhancement was 930 % at 16 kV supplied voltage and the heat flux was 5 kW/m². In the range of 0-15 kV supplied voltage, heat transfer enhancement was linearly proportional to the supplied voltage and lowly off when it higher than 15 kV. It was also found that there was insignificant increase of heat transfer coefficient when the heat flux and the supplied voltage were greater than 10 kW/m² and 20 kV, respectively.

Yeh et al. [117] compared the performance of double-flow type solar air heaters, in which air was flowing simultaneously over and under the absorbing plate, which more effective than that of the devices with only one flow channel over or under the absorbing plate because the heat-transfer area in double-flow systems was double. The effect of the fraction of mass flow rate in the upper or lower flow channel of a double-flow device on collector efficiencies had also been investigated theoretically and experimentally. Considerable improvement in collector performance was obtained by employing a double-flow type solar air heater, instead of using a single-flow device, if the mass flow rates in both flow channels were kept the same.

Pottler et al. [118] derived the optimized geometries of solar air heater which shown in Fig. 2.5. As heat transfer augmentation usually increased friction losses, optimum fin geometry had to be found. For a specific air mass flow rate of 70 kg/(m·h), the air gap for smooth absorbers without fins should be about 7 to 8 mm to get a maximized yearly net energy output of about 2680 MJ/m during the heating season from October through April. Finned absorbers performed much better. Continuous aluminum-fins, 0.1 mm thick and spaced about 6 mm apart in a 30-mm-wide air gap yielded about 900 MJ/m yearly net output. Offset strip fins did not showed an improved performance compared to optimally space continuous fins, due to the larger electrical power for this geometry. However, offset strip fins yielded high net energy gains for large fin spacing.

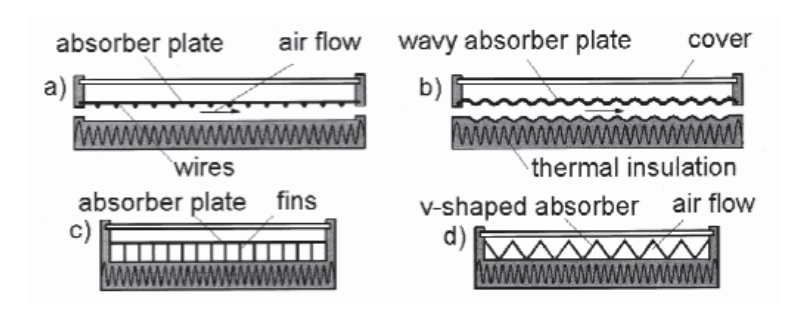


Fig. 2.5 Solar air heaters with heat transfer augmentation [118].

Jiracheewanun et al. [119] studied the heat transfer enhancement and performed flow visualization of air flow through tube bank under electric field. The experimental apparatus consisted of the grounded tube bank of 3x3, 3x6, and 3x9 rows and wire electrodes placed

around each tube. The range of supplied voltage was 0-16 kV. It was found that the heat transfer enhancement was 54 % at 16 kV supplied voltage and the Reynolds number was 213. It was also found that electric field showed effective the heat transfer within 12-16 kV supplied voltage.

Verma and Prasad [120] investigated the artificially roughness in the solar air heaters, which perform better than the plane ones under the same operating conditions. Fig. 2.6 shows the results of various parametric ratios of roughness pitch that effected to the flow patterns. Artificial roughness leaded to even more fluid pressure thereby increasing the pumping power. Roughness and flow parameters composed with relative roughness pitch, relative roughness height, and flow Reynolds number have a combined effect on the heat transfer as well as fluid pressure (friction factor). Investigation for the optimal thermohydraulic performance (i.e. maximum heat transfer for minimum friction loss) of artificially roughness solar air heaters had been carried out. An optimization parameter known as roughness Reynolds number which combines the roughness and flow effect had been considered.

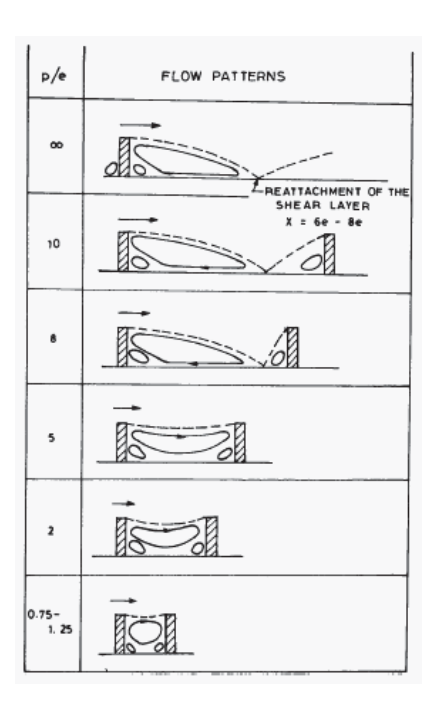


Fig. 2.6 Flow pattern downstream the roughness as a function of pitch [120].

Wangnipparnto et al. [121] studied the airside performance of a thermosyphon heat exchanger with and without the presence of EHD in low Reynolds number region. For the test results without EHD, the predictive ability of the previous correlation significantly under-estimates the present results. With the introduction of EHD, there was significantly increased of heat transfer coefficient when the supplied voltage was higher than 15.5 kV. In the mean time, for a supplied voltage of 17.5 kV, the heat transfer coefficient could be improved by 15% at a Reynolds number of 58. The power consumption relative to the heat transfer rate improvement was within 0.5-20 %.

Yeh et al. [122] Investigated the experimental and analytical works of a design for inserting an absorbing plate to divided the air duct into two channels (the upper and the lower), for double-flow operation in solar air heaters with fins attached over and under the absorbing plate which can illustrated in Figs. 2.7 and 2.8. The present work was restricted to the case where the outside air was being heated directly, and the configuration investigated here will have lower collector efficiency if the inlet-air temperature was substantially higher than the ambient temperature because of the far greater potential for heat loss from the top. However, the double-flow device introduced here was designed for creating a solar collector with heat-transfer area double between the absorbing plate and heated air. This advantage may compensate for the heat loss from the top when the inlet-air temperature is higher than the ambient temperature. The agreement of the theoretical predictions with those measured values from the experimental results was fairly good. Considerable improvement in collector efficiency of solar air heaters with fins attached was obtained by employing such a double-flow device, instead of using a single-flow example and operating at the same total flow rate. Both the theoretical predictions and experimental results showed that the optimal fraction of airflow rate in upper and lower subchannels was around the value of 0.5. The effect of the flow-rate ratio of the two air streams of flowing over and under the absorbing plate on the enhancement of collector efficiency was also investigated.

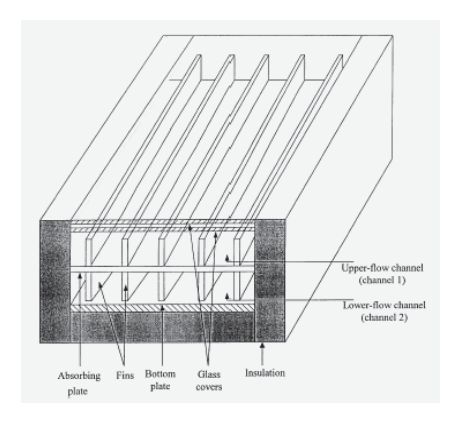


Fig. 2.7 Double-flow solar air heater with fins attached [122].

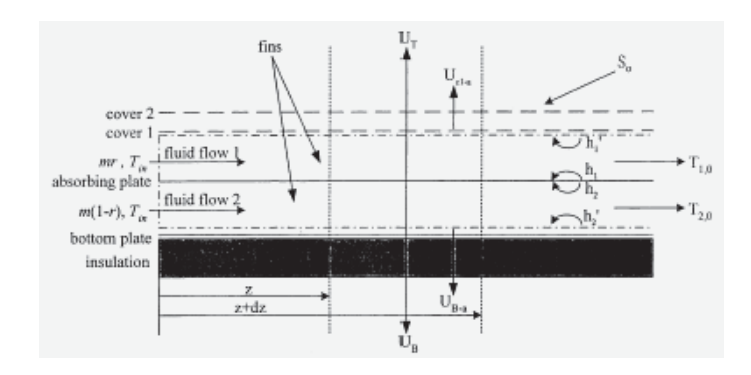


Fig. 2.8 Energy-flow diagram of double-flow solar air heater with fins attached [122].

Momin et al. [123] investigated an experimental work of the effect of geometrical parameters of V-shaped ribs on heat transfer and fluid flow characteristics of rectangular duct of solar air heater with absorbing plate having V-shaped ribs on its underside which represented as Fig. 2.9. The range of parameters for this study had been decided on the basis of practical considerations of the system and operating conditions. The investigation had covered a Reynolds number range of 2500–18000, relative roughness height of 0.02–0.034 and angle of attack of flow of 30–90° for a fixed relative pitch of 10. Results had also been compared with those of smooth duct under similar flow conditions to determine the enhancement in heat transfer coefficient and friction factor. The correlations had been developed for heat transfer coefficient and friction factor for the roughness duct.

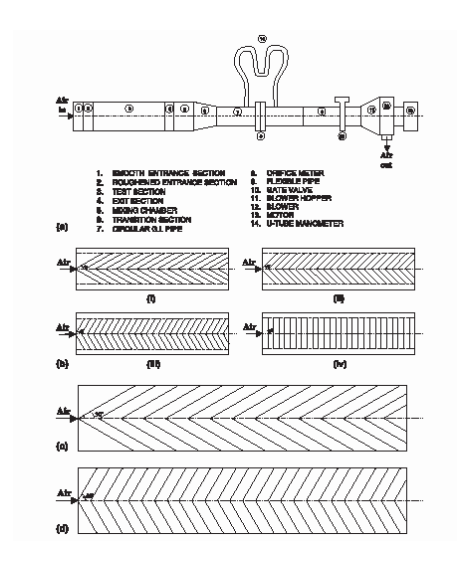


Fig. 2.9 Schematic diagram of experimental setup and roughness elements [123].

Bhagoria et al. [124] performed the experimental study to collect heat transfer and friction data for forced convection flow of air in solar air heater rectangular duct with one broad wall roughness by wedge shaped transverse integral ribs (Fig. 2.10). The experiment encompassed the Reynolds number range from 3000 to 18000, relative roughness height 0.015 to 0.033, and rib wedge angle of 8, 10, 12, and 15°. The effect of parameters on the heat transfer coefficient and friction factor were compared with the result of smooth duct under similar flow conditions. Statistical correlations for the Nusselt number and friction factor had been developed in terms of geometrical parameters of the roughness elements and the flow Reynolds number.

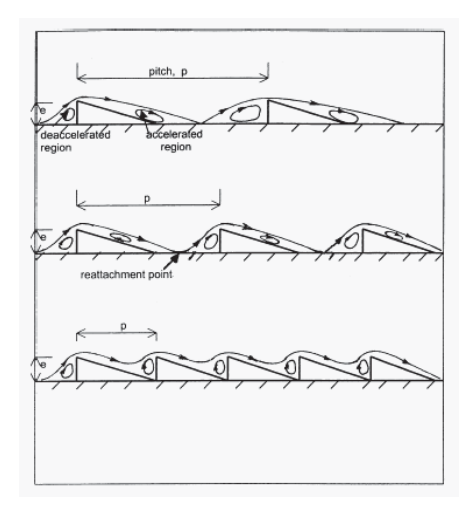


Fig. 2.10 Approximate model of flow patterns for different pitches [124].

#### 2.3 Mathematical Researches

Mathew and Lai [125] presented the numerical results for laminar forced convection in a horizontal channel with two wire electrodes. Attention was also focused on the effect of added electric field on the flow stability. The electric field was generated by positive corona from wire electrodes charged with a DC high voltage between 10-17.5 kV. The Reynolds number considered was in the range of 75-2400. Depending on the EHD number (the ratio between electrical body force and flow inertia), the flow and temperature fields may became steady, periodic, or non-periodic. When the flow inertia was weakened (i.e., a high EHD number), the flow and temperature fields exhibited on oscillatory nature. The oscillation was mainly due to the generation and destruction of multiple recirculation cells. With an increase in the flow velocity, the secondary flow was suppressed and the flow and temperature fields stabilized. The results are illustrated in Figs. 2.11-2.13. It had been shown that an enhancement in heat transfer was possible due to the oscillation of flow field. The maximum enhancement in heat transfer can be as high as six times of that with out the electric field. In addition, it can be observed that the heat transfer enhancement increased with the supplied voltage but decreased with the Reynolds number.

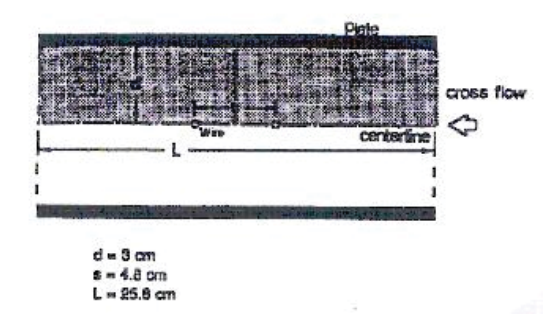


Fig. 2.11 A horizontal channel with two wire electrodes [125].

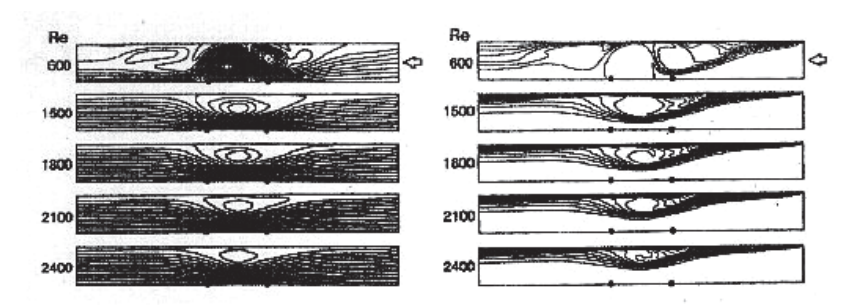


Fig. 2.12 Stable flow and temperature fields for  $V_0 = 12.5 \text{ kV}$  [125].

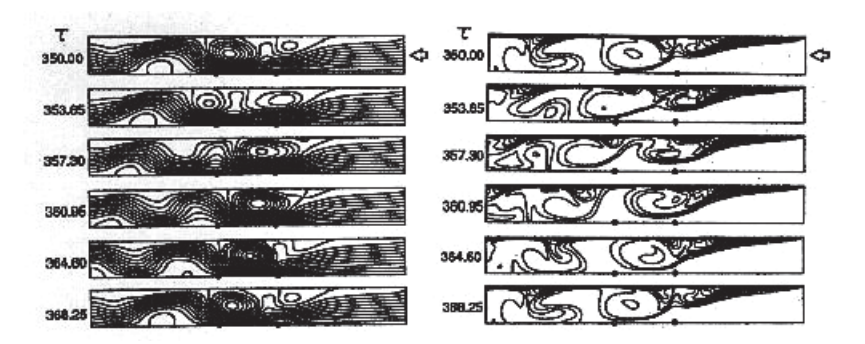


Fig. 2.13 Oscillatory flow and temperature fields for Re = 1200 and  $V_0$  = 12.5 kV [125].

Yadav [126] presented the parametric analysis of a suspended flat plate solar air heater following a transient approach. Fig. 2.14 shows the Schematic diagram of a suspended flat plate solar air heater. An explicit expression for air temperature had been derived as a function of time and the space coordinate. Moreover, explicit expressions were also presented for the glass cover temperature, absorbing plate temperature, useful energy, and efficiency of the proposed system. The effects of several parameters, e.g. space coordinate, mass flow rate, flow velocity, air depth, absorptivity and inlet air temperature on the performance of the proposed system had also been studied. For appreciation of the analytical results, numerical calculations had been made, and the results were shown graphically.

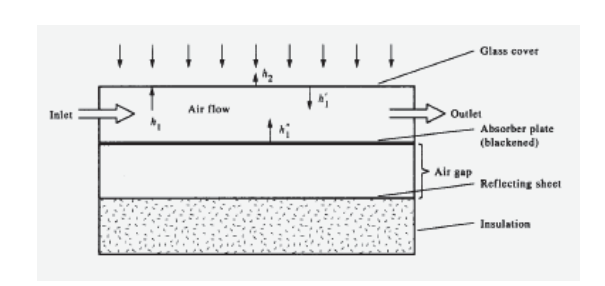


Fig. 2.14 Schematic diagram of a suspended flat plate solar air heater [126].

Goo and Lee [127] developed the numerical scheme to estimate more exactly the collection efficiency of particles in the wire-plate electrostatic precipitator (ESP). The involved physical phenomena such as corona field, turbulent EHD flow field, particle charging, and turbulent motion of particles were treated simultaneously. To overcome the deficiencies of the Eulerian method used up to now, a Lagrangian particle-tracking method coupled with the Monte-Carlo method for simulating the stochastic nature of turbulence was used. With this computational scheme, the characteristics of the ESP were analyzed for a short-length ESP where the effect of developing flow in the entrance region was substantial. The simulation results agreed well with the experimental data, thus it was expected that the characteristics of wire-plate ESP where charging and collection occurs simultaneously can be analyzed using this method without having recourse to a collection efficiency model based on average field characteristics.

Tada et al. [128] studied the theoretical analysis on the enhancement of forced convection heat transfer by applying an electric field. Computational domain was performed in the channel flow where a series of wire electrodes were installed in parallel with the primary flow direction, or installed at right angle to the primary flow direction. It was found that the phenomenon was also performed taking account of momentum transfer between ions and neutral fluid molecules as shown in Figs. 2.15 and 2.16. The enhancement effect of the ionic wind was shown in connection with the operating parameters such as the applied voltage and the primary flow velocity, and the system geometry including the wire electrode arrangement. The application of the ionic wind was considered to be attractive method of enhancing heat transfer in the low Reynolds number where the application of passive method was not effective.

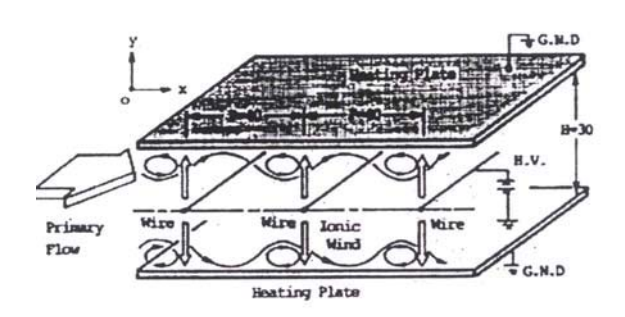


Fig. 2.15 Physical system (cross wire arrangement) [128].

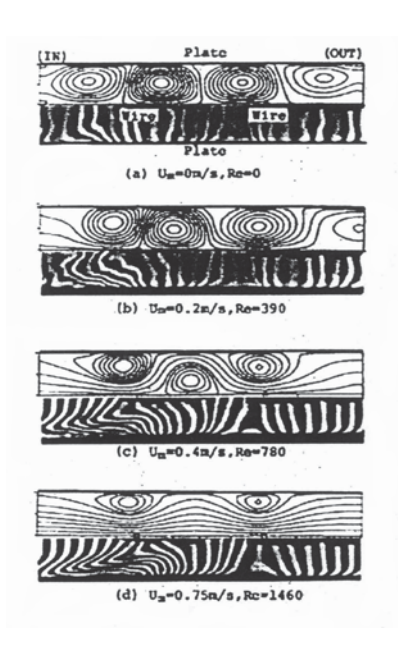


Fig. 2.16 Flow patterns in EHD field ( $V_0 = 12 \text{ kV}$ ) [128].

Yang and Lai [129] performed the numerical examination of the heat transfer enhancement using electric field for natural convection in an enclosure. This work was particularly interested on the effects of Joule heating. Attention had also been focused on the stability of the flow and temperature fields under the influence of electric field. Calculations had covered a wide range of parameters 10-17.5 kV supplied voltage and Rayleigh number was in the range of 10<sup>3</sup>-10<sup>6</sup>, the illustrations are shown in Figs. 2.17-2.19. It was found that Joule heating, although had an additional contribution to heat transfer enhancement at a low Rayleigh number, could result in heat rejection to the hot wall. The effect of Joule heating diminished as the Rayleigh number increases, but the heat

transfer enhancement using electric field also loses its attraction. Therefore, one can concluded that EHD enhanced natural convection was most effective to Rayleigh number in the intermediate range.

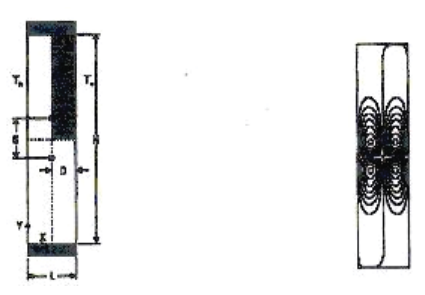


Fig. 2.17 A rectangular enclosure with differentially heated vertical walls and two wire electrodes and the steady flow induced by electric field alone at 15 kV [129].

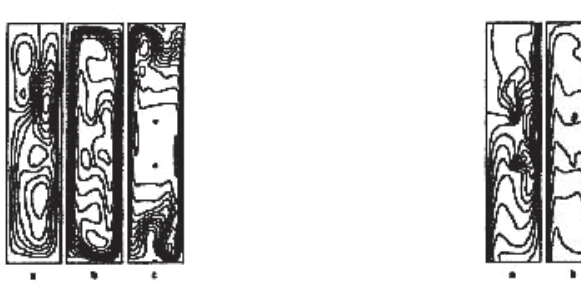


Fig. 2.18 Flow and temperature fields for natural convection with heat generation at the wires, (a)  $Ra = 10^4$ , (b)  $Ra = 10^5$ , (c)  $Ra = 10^6$  [129].

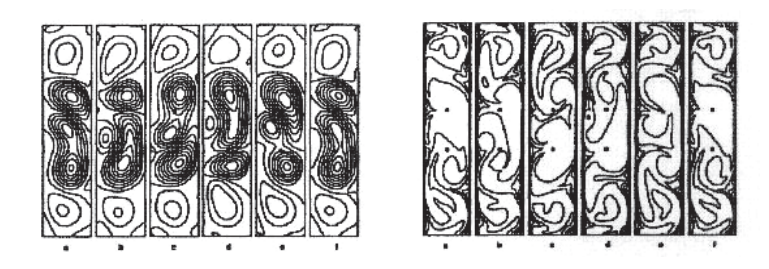


Fig. 2.19 Oscillatory flow and temperature fields at  $V_0 = 10 \text{ kV}$  and Ra = 10 [129].

Badr and Kocabiyik [130] studied the problem of two-dimensional oscillating viscous flow over an elliptic cylinder. The flow was considered incompressible and the free stream oscillations were harmonic. Attention was focused upon only two symmetric flow cases. In the first, flow was symmetric about the major axis whereas in the second, flow was symmetric about the minor axis. The parameters involved were the cylinder axis ratio, Reynolds number, and the oscillation frequency. The major-minor axis ratio of the elliptic cylinder ranges between 1.25 and 2 and the Reynolds number in the range of 500-1000. The methods of solution and numerical scheme were verified by applying them to the special case of an elliptic cylinder starting its constant velocity motion impulsively from rest. The results were compared with the documented translating case, and a good agreement was found. The flow field development was first presented for the two cases of Reynolds number 500 and 1000 in the form of stream line patterns. Comparison between viscous and invicid flow results showed a better agreement for higher values of Reynolds number. Although numerical results were only obtained for harmonic oscillations, the method of solution presented can be applied to free-stream oscillations of any prescribed form.

Lami et al. [131] developed a mathematical model of electric field strength and space charge density in an ESP as

$$q = -\varepsilon \nabla^2 V - q^n - \varepsilon \nabla^2 V^n, \qquad (2.1)$$

$$\frac{\partial q}{\partial t} = b \left( \nabla V^n \cdot \nabla q + \nabla q^n \cdot \nabla V \right) + 2 \frac{b}{\varepsilon} q^n q = -\frac{b}{\varepsilon} \left( q^n \right)^2 + b \nabla V^n \cdot \nabla q^n. \tag{2.2}$$

The model was based upon the time-dependent, governing equations derived from the classical electrostatic equations on two-dimensional domain. A finite difference method was used to solve numerically the constitute equations. The transient, linear system of equations was discrete on a body-fitted coordinate by mean of analytical development. The body-fitted in orthogonal coordinate system provided accurate solution near the wire with a relatively low number of nodes. The reason for such a behavior was due to the nearly natural alignment of electric field to coordinate lines originating from the wire. The grid selected had the advantage to adjust the nodal spacing over the domain to obtain both good

accuracy and economic computer CPU time. Extension of the model to more complicated wire system was also outlined.

Choi and Fletcher [132] studied the behavior of charged particles in turbulent gas flow in ESP as shown in Fig. 2.20 which was crucial information to optimize precipitator efficiency. This work described a strongly coupled calculation procedure for the rigorous computation of particle dynamics during ESP taking into account the statistical particle size distribution which given by

$$\frac{\partial}{\partial x_k} \left( \rho \mathbf{v}_i \mathbf{v}_k - \left( \mu + \mu_t \right) \frac{\partial \mathbf{v}_i}{\partial x_k} \right) = -\frac{\partial P}{\partial x_i} + \mathbf{f}_{D_i} + q \mathbf{E}_i, \tag{2.3}$$

Ion charge density at the wire was adjusted by the iterative process until the calculated electric field agrees with the value calculated from Peek's formula [133]

$$q^* = q^* \left(\frac{E^n}{E_{p_{ock}}}\right)^{\gamma}, \tag{2.4}$$

$$q^{n+1} = (1-\omega)q^n + \omega q^*. {2.5}$$

The gas flow was calculated by using the commercial CFD package FLUENT linked to a finite volume solver for the electric field and ion charge. Particle charge density and the particle velocity were averaged in a control volume to use Lagrangian in calculation.

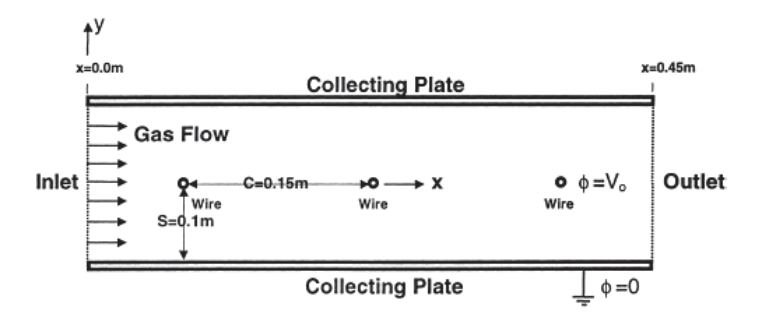


Fig. 2.20 Schematic precipitator geometry [132].

Rafiroiu et al. [134] extended the studied of Peek's formula, which was found to be valid in several simple electrode configuration. The experimental setup specifically modeled the several electrode arrangements. The effect of associating the corona wire to one or several tubular electrodes of various shapes and sizes was investigated. The experimentally determined corona inception voltage was used as input data of a boundary element method program for the electric field computation. The computed values of the electric field were compared with those given by Peek's formula for wire electrodes of same radius. The derived conclusions can be of help in the custom design of the corona electrode arrangements for various electrostatic applications.

Arulanandam et al. [135] determined the unglazed transpired solar collector effectiveness by computational fluid mechanics (CFD), for conditions of no wind. Because of symmetry, the computational domain needed only to extend over a representative element, which included one hole and the region immediately adjacent to it extending to half the distance between holes. Simulations were carried out over a wide range of conditions, and the results are incorporated into a correlation model. Because of the nowind assumptions, the model was of limited direct use, but when combined with experimental data, the model could permitted a wider-ranging correlation equation to be obtained.

Hegazy [136] presented a remarkably simple criterion for determining the channel optimum depth-to-length ratio which effectively maximized the useful energy from collectors that were designed to heat a fixed mass rate of air flow. The engineering accuracy of the analytically derived criterion had been corroborated over a wide range of ambient variables, design parameters and operating conditions as shown in Fig. 2.21. The results demonstrated clearly the decisive role of the ratio in enhancing heater performance. A poor choice of this ratio can significantly affect the thermal conversion efficiency, especially for lower specific mass rates. In contrast, decreasing the ratio beyond the optimal value leads to a slight enhancement in heater efficiency. Of significance was the finding that, by choosing optimized value, it also maximized the air temperature rise. For variable flow operation, the ratio of  $D/L = 2.5 \times 10^{-3}$  was recommended as the optimal. Moreover, the reported results and discussions had provided valuable conceptual insights regarding generalization of the performance curves of conventional solar air heaters. It was

found that the analytically determined channel depth parameter, in conjunction with the air specific mass rate, were quite successful in correlating the performance in general terms.

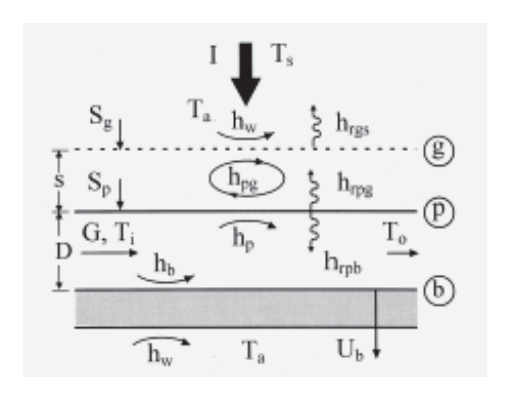


Fig. 2.21 Schematic of conventional solar air heater showing energy balance [136].

Demirel et al [137] studied the characteristics of wall-to-air heat transfer for a fully developed forced convection in a large rectangular packed duct with 160 cm heated length, 40 cm width, and for low bed equivalent diameter to particle diameter ratio. The separation distance between the top and bottom walls was 10 cm. A uniform heat flux was supplied at the top wall, while the bottom wall was insulated. Raschig rings in two and spherical packing in three sizes had been used in the air flow passage to investigate the enhancement of heat transfer due to packing. Temperature profiles for the steady and unsteady states had been measured. In modeling, the Ergun equation and energy equations were solved to calculate the temperature profile for the steady-state only. It was found that the introduction of the packing into the air flow passage increases the wall-to-fluid heat transfer approximately three times compared with that of empty bed. This finding can enhance the rational use of energy from solar air heaters, chemical reactors, electronic cooling and many other engineering applications.

Hilmer et al. [138] developed a method to calculate the short-term dynamic behavior of solar collectors, working with varying fluid-flow rate. It was based on a system of first-order partial differential equations. The method was applied to model a large unglazed collector used for heating a public outdoor swimming-pool in Marburg (Germany). A validation with data measured at this collector showed good short- and long-term accuracy of the model at constant and varying flow rates. Furthermore, the dynamic behavior of the

detailed model was compared to that of several model approximations especially at varying flow rate. In the case of unglazed collectors a simple dynamic model, based on an ordinary differential equation, gives accurate results in most practical applications even at varying flow rate. The extension of the method to flat-plate collectors was demonstrated as well.

Gao et al. [139] conducted a numerical study to investigate the natural convection inside the channel between the flat-plate cover and the sine-wave absorber in a cross-corrugated solar air heater (Fig. 2.22). The effects of major system parameters on the natural convection heat transfer were simulated. These parameters including the difference of average temperatures between the cover and the absorber, the characteristic height ratio of the channel which was defined as the ratio of the channel height to the amplitude height of the wavelike absorber, the characteristic geometric ratio which was defined as the ratio of one-fourth of the wavelength to the amplitude height of the absorber, and the angle of inclination of the heater. The numerical results showed that to suppress the natural convection heat loss effectively, the characteristic height ratio should be larger than 2, the characteristic geometric ratio larger than 1, and the angle of inclination less than 40°.

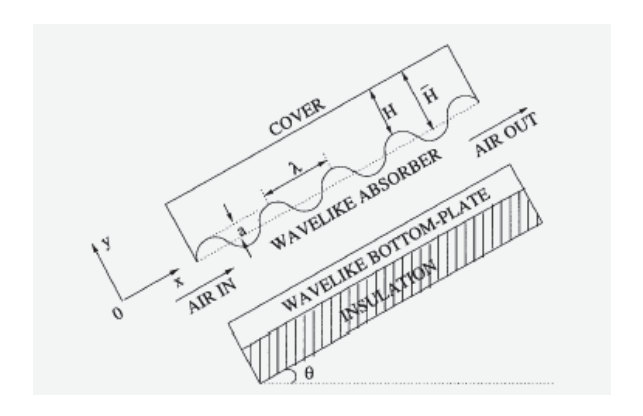


Fig. 2.22 Schematic view of the cross corrugated solar air heater [139].

Talaie et al. [140] presented a new computational scheme that was developed to evaluate current-voltage characteristics of a wire-plate high voltage configuration system applicable for single-stage ESP which was defined such that

$$\frac{\partial \left(qb\boldsymbol{E}_{x}+\boldsymbol{v}q\right)}{\partial x} + \frac{\partial \left(qb\boldsymbol{E}_{y}+\boldsymbol{v}q\right)}{\partial y} + \frac{\partial \left(\boldsymbol{v}_{p}q_{p}\right)}{\partial x} + \frac{\partial \left(\boldsymbol{v}_{p}q_{p}\right)}{\partial y} \\
= D_{e}\left(\frac{\partial^{2}q}{\partial x^{2}} + \frac{\partial^{2}q}{\partial y^{2}}\right) + D_{p}\left(\frac{\partial^{2}q_{p}}{\partial x^{2}} + \frac{\partial^{2}q_{p}}{\partial y^{2}}\right) + S_{i}$$
(2.6)

This new approach was based on the fact that increasing supplied voltage increases the corona sheath radius. The advantage of this new model compared to previous ones was that the model was capable of computing the rate of corona sheath radius augmentation. Ion charge density at corona edge was calculated by using a new equation, which was developed by dimensional analysis. Also, by using this model, the number of grid points and hence CPU computational time was greatly reduced.

Rafiroiu et al. [141] presented an analysis of the corona field for such electrode arrangements. A corona wind associated with a non-ionizing metallic tube connected to the high voltage and facing a grounded plane was an electrode arrangement frequently encountered in electrostatic processes. The two-loop computational algorithm proposed for the study of this electric field configuration was alternatively solved the Poisson's equation and the equation of charge conservation. Finally, Peek's formula [55] for corona onset was fulfilled.

Ozsunar et al. [142] conducted the numerical analysis of mixed convection heat transfer in rectangular channels under various operating conditions. The lower surface of the channel was subjected to a uniform heat flux, sidewalls were insulated and adiabatic, and the upper surface was exposed to the surrounding fluid. Solutions were obtained for Pr=0.7, inclination angles 0-90°, Reynolds numbers of 50-1000, and modified Grashof numbers of  $7x10^5$  to  $4x10^6$ . The three-dimensional elliptic governing equations were solved using a finite volume based computational fluid dynamics (CFD) code. From a parametric study, local Nusselt number distributions were obtained and effects of channel inclination, surface heat flux and Reynolds number on the onset of instability were investigated. Results obtained from the simulations are compared with the literature and a parallel conducted experimental study, from which a good agreement was observed. The onset of instability was found to move upstream for increasing Grashof number. On the

other band, onset of instability was delayed for increasing Reynolds number and increasing inclination angle.

Anagnostopoulos and Bergeles [143] proposed a numerical simulation methodology for calculating the electric field in wire-duct precipitation systems by using finite differencing in orthogonal curvilinear coordinates to solve the potential equation. Charge density distributions were obtained by the method of characteristics or using a prediction-correction scheme which was given by

$$q_{new}^{n+1} = \left[ \frac{1}{q^{(n+1)}} + f_u \left( \frac{1}{q_w^{-(n+1)}} - \frac{1}{q_w^{-(n)}} \right) \right]^{-1}.$$
 (2.7)

A new mesh generation technique produced body-fitted orthogonal grids, thus the requirements in grid nodes were kept low and the implementation of the method of characteristics became a very easy and fast task. The numerical experiments showed that the commonly used criterion of convergence, which was based on the maximum difference in charge density values between two successive iterations, may not correspond to the remaining error in the field equations. Therefore, its value must be kept properly low in order to avoid erroneous results due to the incomplete convergence.

Gunnewiek et al. [144] extended the earlier study of unglazed transpired-plate solar air heaters (which using a computational fluid dynamics (CFD) model, but that study was limited to the case where there was no wind presented) to the case where there was wind. Large collectors are now routinely built that cover the sides of sizeable buildings (Fig. 2.23), and the problem of designing the system so that the flow of the air through the collector face is reasonably uniform and so that there is no outflow over part of the collector face has been seen as a challenging one. Various building orientations were examined, at a wind speed of 5 m/s. Fig. 2.24 shows the effect of wind direction and it was found to reinforce those factors that tend to produce outflow, and in light of this study, the recommended minimum suction velocity required to avoid outflow has been raised from about 0.0125 m/s to about 0.03 m/s, depending on the building shape. On the other hand, there were possible strategies that could be adopted to reduce the effect of wind, and these were discussed.

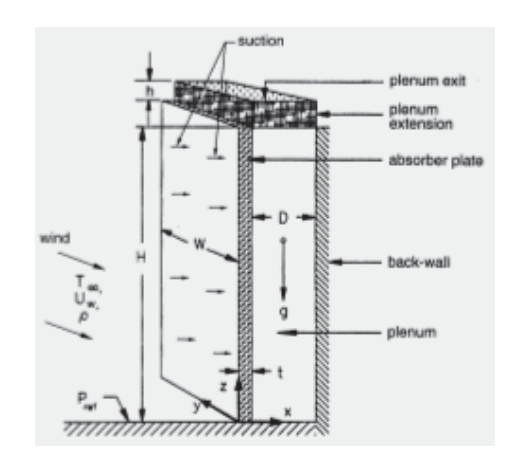


Fig. 2.23 Dimensional sketch of collector's plenum [144].

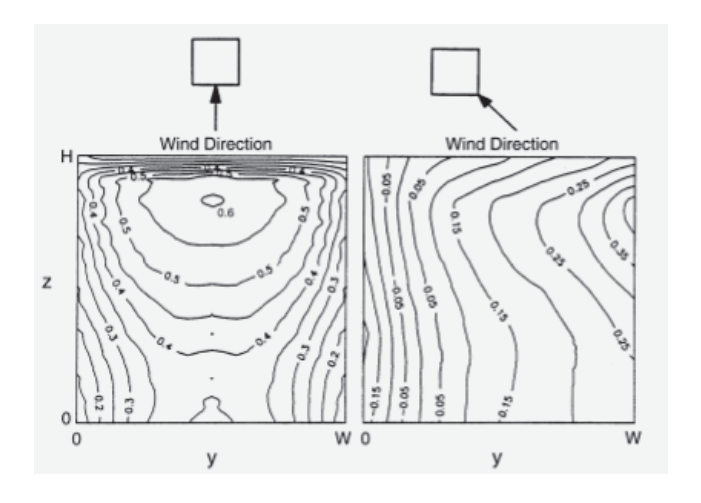


Fig. 2.24 Contour lines of model for the facing directly or quartering wind [144].

Kazeminejad [145] analyzed temperature distribution over the absorbing plate of a parallel flow flat-plate solar collector with one- and two-dimensional steady-state conduction equations with heat generations. The governing differential equations with boundary conditions were solved numerically using a control volume-based finite difference scheme. Comparisons of one- and two-dimensional results showed that the isotherms and performance curve, stated in terms of an effectiveness/number-of-transfer-unit relationship, for one-dimensional analysis slightly deviate from that of two-dimensional analysis, particularly under low mass flow rate conditions. In addition, collector efficiency as a function of operating point was computed and presented

graphically for different collector configuration and various operating conditions. For general engineering purposes, these performance curves may be used for efficient and optimum design of liquid flat-plate solar collectors.

Kasayapanand et al. [146] numerically analyzed the effect of the electrode arrangements in the tube bank on the characteristics of EHD enhanced heat transfer. The numerical modeling of the laminar forced convection includes the interactions among the electric field, flow field, and temperature field. It was found that the heat transfer was significantly enhanced by the EHD at low Reynolds number and the short distance between the wire electrodes and the tube surface from which optimized electrode arrangements were reported for aligned and staggered tube configuration. Moreover, the transformed governing equations could be expressed as;

In the electric field, Poisson equation could be given by

$$\frac{\partial^{2}V}{\partial\xi^{2}} \left[ \left( \frac{\partial\xi}{\partial x} \right)^{2} + \left( \frac{\partial\xi}{\partial y} \right)^{2} \right] + \frac{\partial^{2}V}{\partial\eta^{2}} \left[ \left( \frac{\partial\eta}{\partial x} \right)^{2} + \left( \frac{\partial\eta}{\partial y} \right)^{2} \right] +$$

$$2 \frac{\partial^{2}V}{\partial\xi\partial\eta} \left[ \left( \frac{\partial\xi}{\partial x} \right) \left( \frac{\partial\eta}{\partial x} \right) + \left( \frac{\partial\xi}{\partial y} \right) \left( \frac{\partial\eta}{\partial y} \right) \right] + , \qquad (2.8)$$

$$\frac{\partial V}{\partial\xi} \left[ \frac{\partial^{2}\xi}{\partial x^{2}} + \frac{\partial^{2}\xi}{\partial y^{2}} \right] + \frac{\partial V}{\partial\eta} \left[ \frac{\partial^{2}\eta}{\partial x^{2}} + \frac{\partial^{2}\eta}{\partial y^{2}} \right] = -\frac{q}{\varepsilon}$$

and the corona-current continuity equation could be written as

$$q^{2} = \varepsilon \left[ \left[ \left[ \left( \frac{\partial q}{\partial \xi} \right) \left( \frac{\partial \xi}{\partial x} \right) + \left( \frac{\partial q}{\partial \eta} \right) \left( \frac{\partial \eta}{\partial x} \right) \right] \times \left[ \left( \frac{\partial V}{\partial \xi} \right) \left( \frac{\partial \xi}{\partial x} \right) + \left( \frac{\partial V}{\partial \eta} \right) \left( \frac{\partial \eta}{\partial x} \right) \right] + \left[ \left[ \left[ \left( \frac{\partial q}{\partial \xi} \right) \left( \frac{\partial \xi}{\partial y} \right) + \left( \frac{\partial q}{\partial \eta} \right) \left( \frac{\partial \eta}{\partial y} \right) \right] \times \left[ \left( \frac{\partial V}{\partial \xi} \right) \left( \frac{\partial \xi}{\partial y} \right) + \left( \frac{\partial V}{\partial \eta} \right) \left( \frac{\partial \eta}{\partial y} \right) \right] \right] \right]. (2.9)$$

The vorticity transport equation was converted into the form

$$\frac{\partial \boldsymbol{\omega}}{\partial t} = \left[ \left[ \left( \frac{\partial \boldsymbol{\psi}}{\partial \xi} \right) \left( \frac{\partial \xi}{\partial x} \right) + \left( \frac{\partial \boldsymbol{\psi}}{\partial \eta} \right) \left( \frac{\partial \eta}{\partial x} \right) \right] \times \left[ \left( \frac{\partial \boldsymbol{\omega}}{\partial \xi} \right) \left( \frac{\partial \xi}{\partial y} \right) + \left( \frac{\partial \boldsymbol{\omega}}{\partial \eta} \right) \left( \frac{\partial \eta}{\partial y} \right) \right] - \left[ \left[ \left( \frac{\partial \boldsymbol{\psi}}{\partial \xi} \right) \left( \frac{\partial \xi}{\partial y} \right) + \left( \frac{\partial \boldsymbol{\psi}}{\partial \eta} \right) \left( \frac{\partial \eta}{\partial y} \right) \right] \times \left[ \left( \frac{\partial \boldsymbol{\omega}}{\partial \xi} \right) \left( \frac{\partial \xi}{\partial x} \right) + \left( \frac{\partial \boldsymbol{\omega}}{\partial \eta} \right) \left( \frac{\partial \eta}{\partial x} \right) \right] \right] + \left[ \left[ \left( \frac{\partial \boldsymbol{\psi}}{\partial \xi} \right) \left( \frac{\partial \xi}{\partial x} \right) + \left( \frac{\partial \xi}{\partial y} \right)^{2} \right] + \left( \frac{\partial \boldsymbol{\psi}}{\partial \eta} \right) \left( \frac{\partial \eta}{\partial x} \right) + \left( \frac{\partial \eta}{\partial y} \right)^{2} \right] + \left[ \left( \frac{\partial \eta}{\partial y} \right) \left( \frac{\partial \eta}{\partial y} \right) \right] + \left[ \left( \frac{\partial \boldsymbol{\psi}}{\partial \xi} \right) \left( \frac{\partial \xi}{\partial x} \right) + \left( \frac{\partial \eta}{\partial y} \right) \left( \frac{\partial \eta}{\partial x} \right) + \left( \frac{\partial \xi}{\partial y} \right) \left( \frac{\partial \eta}{\partial y} \right) \right] + \left[ \left( \frac{\partial \boldsymbol{\psi}}{\partial \xi} \right) \left( \frac{\partial \xi}{\partial x} \right) + \left( \frac{\partial \eta}{\partial \eta} \right) \left( \frac{\partial \eta}{\partial x} \right) \right] \times \left[ \left( \frac{\partial \boldsymbol{\psi}}{\partial \xi} \right) \left( \frac{\partial \xi}{\partial y} \right) + \left( \frac{\partial \boldsymbol{\psi}}{\partial \eta} \right) \left( \frac{\partial \eta}{\partial y} \right) \right] - \left[ \left[ \left( \frac{\partial q}{\partial \xi} \right) \left( \frac{\partial \xi}{\partial y} \right) + \left( \frac{\partial q}{\partial \eta} \right) \left( \frac{\partial \eta}{\partial y} \right) \right] \times \left[ \left( \frac{\partial \boldsymbol{V}}{\partial \xi} \right) \left( \frac{\partial \xi}{\partial x} \right) + \left( \frac{\partial \boldsymbol{V}}{\partial \eta} \right) \left( \frac{\partial \eta}{\partial y} \right) \right] - \left[ \left[ \left( \frac{\partial q}{\partial \xi} \right) \left( \frac{\partial \xi}{\partial y} \right) + \left( \frac{\partial q}{\partial \eta} \right) \left( \frac{\partial \eta}{\partial y} \right) \right] \times \left[ \left( \frac{\partial \boldsymbol{V}}{\partial \xi} \right) \left( \frac{\partial \xi}{\partial x} \right) + \left( \frac{\partial \boldsymbol{V}}{\partial \eta} \right) \left( \frac{\partial \eta}{\partial x} \right) \right] \right] \right]$$

$$(2.10)$$

The transformed equation of stream function-vorticity relation could be defined as

$$\frac{\partial^{2} \psi}{\partial \xi^{2}} \left[ \left( \frac{\partial \xi}{\partial x} \right)^{2} + \left( \frac{\partial \xi}{\partial y} \right)^{2} \right] + \frac{\partial^{2} \psi}{\partial \eta^{2}} \left[ \left( \frac{\partial \eta}{\partial x} \right)^{2} + \left( \frac{\partial \eta}{\partial y} \right)^{2} \right] +$$

$$2 \frac{\partial^{2} \psi}{\partial \xi \partial \eta} \left[ \left( \frac{\partial \xi}{\partial x} \right) \left( \frac{\partial \eta}{\partial x} \right) + \left( \frac{\partial \xi}{\partial y} \right) \left( \frac{\partial \eta}{\partial y} \right) \right] + , \qquad (2.11)$$

$$\frac{\partial \psi}{\partial \xi} \left[ \frac{\partial^{2} \xi}{\partial x^{2}} + \frac{\partial^{2} \xi}{\partial y^{2}} \right] + \frac{\partial \psi}{\partial \eta} \left[ \frac{\partial^{2} \eta}{\partial x^{2}} + \frac{\partial^{2} \eta}{\partial y^{2}} \right] = -\boldsymbol{\omega}$$

and the energy equation was described as

$$\frac{\partial T}{\partial t} = \left[ \left[ \left( \frac{\partial \boldsymbol{\omega}}{\partial \xi} \right) \left( \frac{\partial \xi}{\partial x} \right) + \left( \frac{\partial \boldsymbol{\omega}}{\partial \eta} \right) \left( \frac{\partial \eta}{\partial x} \right) \right] \times \left[ \left( \frac{\partial T}{\partial \xi} \right) \left( \frac{\partial \xi}{\partial y} \right) + \left( \frac{\partial T}{\partial \eta} \right) \left( \frac{\partial \eta}{\partial y} \right) \right] \right] - \left[ \left[ \left( \frac{\partial \boldsymbol{\omega}}{\partial \xi} \right) \left( \frac{\partial \xi}{\partial y} \right) + \left( \frac{\partial \boldsymbol{\omega}}{\partial \eta} \right) \left( \frac{\partial \eta}{\partial y} \right) \right] \times \left[ \left( \frac{\partial T}{\partial \xi} \right) \left( \frac{\partial \xi}{\partial x} \right) + \left( \frac{\partial T}{\partial \eta} \right) \left( \frac{\partial \eta}{\partial x} \right) \right] \right] + \left[ \frac{\partial^2 T}{\partial \xi^2} \left[ \left( \frac{\partial \xi}{\partial x} \right)^2 + \left( \frac{\partial \xi}{\partial y} \right)^2 \right] + \frac{\partial^2 T}{\partial \eta^2} \left[ \left( \frac{\partial \eta}{\partial x} \right)^2 + \left( \frac{\partial \eta}{\partial y} \right)^2 \right] + \left[ \frac{\partial^2 T}{\partial \xi \partial \eta} \left[ \left( \frac{\partial \xi}{\partial x} \right) \left( \frac{\partial \eta}{\partial x} \right) + \left( \frac{\partial \xi}{\partial y} \right) \left( \frac{\partial \eta}{\partial y} \right) \right] + \left[ \frac{\partial T}{\partial \xi} \left[ \frac{\partial^2 \xi}{\partial x^2} + \frac{\partial^2 \xi}{\partial y^2} \right] + \frac{\partial T}{\partial \eta} \left[ \frac{\partial^2 \eta}{\partial x^2} + \frac{\partial^2 \eta}{\partial y^2} \right] \right] \right] . \quad (2.12)$$

Ammari [147] presented a mathematical model for computing the thermal performance of a single pass flat-plate solar air collector (Figs. 2.25 and 2.26). Air channels were formed by providing metal slats running along the circulated air passage linking the absorbing plate by the bottom one in an endeavor to enhance the thermal efficiency of the solar air collector. A mathematical model, therefore, was developed by which the influence of the addition of the metal slats on the efficiency of the solar collector was studied. A computer code that employed an iterative solution procedure was constructed to solve for the governing energy equations to estimate the mean temperatures of the collector. The effect of volume airflow rate, collector length, and spacing between the absorber and bottom plates on the thermal performance of the present solar air heater was investigated. The results of the comparison had indicated that better thermal performance was obtained by the modified system.

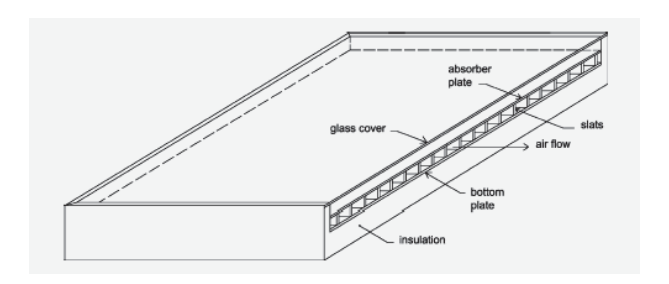


Fig. 2.25 Flat-plate solar air heater with slats [69].

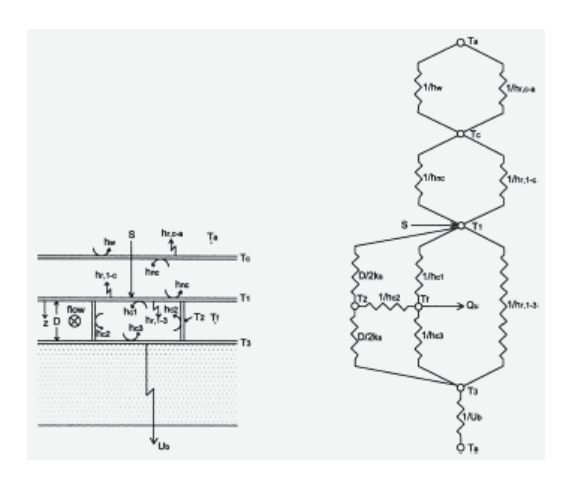


Fig. 2.26 Solar air heater and its thermal network [69].

Abu-Hamdeh [148] developed a mathematical model for predicting thermal efficiency, heat gain, and outlet air temperature of a covered plate attic solar collector under steady conditions. The presented model utilizes the basic principles and relationships of heat transfer was simulated the behavior of the solar air heaters under various conditions. The model was validated by comparing the predicted outlet air temperatures and collector efficiencies to those measured during drying operation of an attic solar collector. The effect of the air speed inside the collector and wind speed above the collector on the collector efficiency were investigated using the mathematical model.

# **CHAPTER 3 THEORETICAL ANALYSIS**

### 3.1 Fluid Dynamics

The governing equations for the, EHD force  $F_E$  per unit volume generated by the electric field with strength E in a fluid of dielectric permittivity  $\varepsilon$ , density  $\rho$ , and uniform temperature T can be expressed as

$$\boldsymbol{F}_{E} = q\boldsymbol{E} - \frac{1}{2}\boldsymbol{E}^{2}\nabla\varepsilon + \frac{1}{2}\nabla\left[\boldsymbol{E}^{2}\left[\frac{\partial\varepsilon}{\partial\rho}\right]_{T}\rho\right],\tag{3.1}$$

In the symbolic notation, vectors are designated by bold-faced letters, while scalars are denoted by italic letters. Where q is the electric charge density in the fluid. The first term of the right qE is the Coulomb force exerted by electric field upon the free charge or electrophoretic component. While the second and the third term corresponds to the dielectrophoretic and electrostrictive forces on and within the fluid.

By assuming, incompressible flow, incorporating Eq. (3.1) into the conservation of momentum is expressed as

$$\rho \frac{d\mathbf{v}}{dt} = \rho \mathbf{g} + \mathbf{F}_E - \nabla P + \mu \nabla^2 \mathbf{v}, \tag{3.2}$$

The vector  $\rho \mathbf{g}$  is the gravitational force per unit volume, P is the local fluid pressure and the last term in the right-hand side of equation represents the viscous terms.

Introducing the vorticity  $\omega$  as

$$\boldsymbol{\omega} = \nabla \times \boldsymbol{v} \,, \tag{3.3}$$

the momentum equation can be rewritten in terms of the vorticity defined above as

$$\frac{\partial \boldsymbol{\omega}}{\partial t} + (\boldsymbol{v} \cdot \nabla) \boldsymbol{\omega} = \boldsymbol{v} \nabla^2 \boldsymbol{\omega} - (\boldsymbol{E} \times \nabla) q. \tag{3.4}$$

The stream function  $(\psi)$  is defined such that

$$\mathbf{v}_{x} = \frac{\partial \psi}{\partial y}, \ \mathbf{v}_{y} = -\frac{\partial \psi}{\partial x},$$
 (3.5)

The vorticity transport equation can be obtained from Eqs. (3.4) and (3.5) further gives

$$\nabla^2 \psi = -\boldsymbol{\omega} \,. \tag{3.6}$$

When attention is brought onto the energy equation of this system, without viscous dissipation effect, the energy equation can be written as

$$\frac{dT}{dt} = \alpha \nabla^2 T + \frac{\sigma_e \mathbf{E}^2}{\rho c_p}.$$
(3.7)

These systems requires appropriate and sufficient boundary conditions for the flow and temperature fields (for example, in a channel) which are given by

$$x = 0; \ \omega = 0, \ \psi = U_i y, \ T = T_i,$$
 (3.8(a))

$$x = L; \frac{\partial \boldsymbol{\omega}}{\partial x} = 0, \frac{\partial \psi}{\partial x} = 0, \frac{\partial^2 T}{\partial x^2} = 0,$$
 (3.8(b))

$$y = 0; \ \boldsymbol{\omega} = -\frac{\partial^2 \psi}{\partial v^2}, \ \psi = 0, \ \frac{\partial T}{\partial v} = 0,$$
 (3.8(c))

$$y = H; \ \boldsymbol{\omega} = -\frac{\partial^2 \psi}{\partial y^2}, \ \psi = U_i H, \ \frac{\partial T}{\partial y} = q_h,$$
 (3.8(d))

at the channel exit, gradients of stream function, vorticity, and heat flux are set to zero. These boundary conditions are less restrictive and are widely accepted.

Where  $\overline{n}$  is the outward perpendicular direction from the wall surface. In addition to the conditions above, a uniform flow is specified at the inlet boundary as well as the non-slip is employed along the surfaces.

### 3.2 Electrostatic

Maxwell equations for the electric field corresponding to the setup are as the followings

$$\nabla \cdot \varepsilon \mathbf{E} = q \,, \tag{3.9}$$

the strength E is given by

$$\boldsymbol{E} = -\nabla V \ . \tag{3.10}$$

As the current is conserved over the domain of calculation, the current continuity equation is given by

$$\nabla \cdot \boldsymbol{J} + \frac{\partial q}{\partial t} = 0, \qquad (3.11)$$

the current density J is given by

$$\mathbf{J} = q\mathbf{v} + \sigma_{e}\mathbf{E} + (\mathbf{v} \cdot \nabla)(\varepsilon \mathbf{E}) - D_{e}\nabla q. \tag{3.12}$$

Combining Eqs. (3.9) with (3.10) and Eqs. (3.11) with (3.12) to eliminate J, one can obtain

$$\nabla^2 V = -\frac{q}{\varepsilon},\tag{3.13}$$

$$q^2 = \varepsilon(\mathbf{E} \cdot \nabla q) \,. \tag{3.14}$$

The boundary conditions required for solving Eqs. (3.13) and (3.14) are

$$V = V_0$$
, at each wire electrodes, (3.15(a))

$$V = 0$$
, along the surface, (3.15(b))

$$E_y = 0$$
, along the symmetry line. (3.15(c))

Electrical potential and space charge density are determined by iterating Eqs. (3.13) and (3.14) starting with an assumed value of space charge density at the wire electrode  $(q_0)$ . The validity of the solution is affirmed by comparing the predicted total current to the measured current at the corresponding voltage. If they are different, Eqs. (3.13) and (3.14) will be recalculated by using the new space charge at the wire electrode. The iteration keeps repeating until the convergence is reached.

#### 3.3 Heat Transfer Characteristic

In terms of heat transmission characteristic, the local heat transfer coefficient in term of the local Nusselt number of the laminar sublayer near surface is simply given by

$$\operatorname{Nu}_{\theta} = \frac{Dh}{k} = \frac{Dq}{k(T_{w} - T_{m})} = \frac{D(\partial T / \partial \overline{n})}{(T_{w} - T_{m})}.$$
(3.16)

#### 3.4 Grid Generation

This mathematical model is dealing with the CFD problem of the complex shapes. To solve the problem, the physical shapes of the computational domain are required to arbitrary irregular meshes. One way to bring the boundaries and the finite-difference mesh into alignment is a coordinate transformation. So the non-uniformly spaced grid can be solved on a uniformly spaced grid by using an appropriate transformation. The transformation relations from Cartesian coordinates (x, y) to a general curvilinear system  $(\xi, \eta)$  is calculated by the Poisson's equation.

The transformation of physical plane into computational plane by using grid generation method is shown in Fig. 3.1. In Fig. 3.1(a), the curve meshes are calculated by Poisson's equation including with constrains along the boundary shapes and at the interior of the computational domain. The computed coordinates (x, y) are mapping to evaluated in

the orthogonal curvilinear coordinates ( $\xi$ ,  $\eta$ ) by using the transformation relations. Finally, all governing equations can be solved on a uniformly spaced grid (Fig. 3.1(b)) that is more reliable, efficient, and simpler than that on a non-uniformly spaced grid.

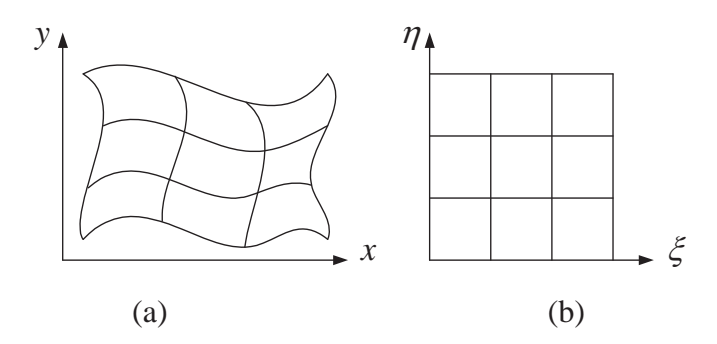


Fig. 3.1 Physical plane and computational plane.

The relationships among the physical plane and computational plane are

$$\frac{\partial \xi}{\partial x} = J \frac{\partial y}{\partial \eta}, \quad \frac{\partial \xi}{\partial y} = -J \frac{\partial x}{\partial \eta}, \quad \frac{\partial \eta}{\partial x} = -J \frac{\partial y}{\partial \xi}, \quad \frac{\partial \eta}{\partial y} = J \frac{\partial x}{\partial \xi}, 
J = \left[ \left( \frac{\partial x}{\partial \xi} \right) \left( \frac{\partial y}{\partial \eta} \right) - \left( \frac{\partial x}{\partial \eta} \right) \left( \frac{\partial y}{\partial \xi} \right) \right] ,$$
(3.17)

where curvilinear coordinates ( $\xi$ ,  $\eta$ ) can be solved by Poisson's equations

$$\alpha \frac{\partial^{2} x}{\partial \xi^{2}} - 2\beta \frac{\partial^{2} x}{\partial \xi \partial \eta} + \gamma \frac{\partial^{2} x}{\partial \eta^{2}} = -I^{2} \left[ P \frac{\partial x}{\partial \xi} + Q \frac{\partial x}{\partial \eta} \right]$$

$$\alpha \frac{\partial^{2} y}{\partial \xi^{2}} - 2\beta \frac{\partial^{2} y}{\partial \xi \partial \eta} + \gamma \frac{\partial^{2} y}{\partial \eta^{2}} = -I^{2} \left[ P \frac{\partial y}{\partial \xi} + Q \frac{\partial y}{\partial \eta} \right]$$
(3.18)

The variables used in the previous equations are given by

$$\alpha = \left[ \left( \frac{\partial x}{\partial \eta} \right)^{2} + \left( \frac{\partial y}{\partial \eta} \right)^{2} \right]$$

$$\beta = \left[ \left( \frac{\partial x}{\partial \xi} \right) \left( \frac{\partial y}{\partial \eta} \right) + \left( \frac{\partial x}{\partial \eta} \right) \left( \frac{\partial y}{\partial \xi} \right) \right]$$

$$\gamma = \left[ \left( \frac{\partial x}{\partial \xi} \right)^{2} + \left( \frac{\partial y}{\partial \xi} \right)^{2} \right]$$

$$P_{boundary}^{n+1} = P_{boundary}^{n} + \tan^{-1} \left( \frac{\theta^{n} - \theta^{*}}{\theta^{*}} \right)$$

$$Q_{boundary}^{n+1} = Q_{boundary}^{n} + \tan^{-1} \left( \frac{\Delta s^{n} - \Delta s^{*}}{\Delta s^{*}} \right)$$

$$\Delta s = \left( \left( x_{i,j-1} - x_{i,j} \right)^{2} + \left( y_{i,j-1} - y_{i,j} \right)^{2} \right)^{1/2}$$

$$\Delta t^{+} = \left( \left( x_{i+1,j} - x_{i,j} \right)^{2} + \left( y_{i+1,j} - y_{i,j} \right)^{2} \right)^{1/2}$$

$$\Delta t^{-} = \left( \left( x_{i,j} - x_{i-1,j} \right)^{2} + \left( y_{i,j} - y_{i-1,j} \right)^{2} \right)^{1/2}$$

$$\frac{dx}{dt} = \left( \frac{1}{\Delta t^{*} + \Delta t^{-}} \right) \left( \left( \frac{\Delta t^{-}}{\Delta t^{*}} \right) \left( x_{i+1,j} - x_{i,j} \right) + \left( \frac{\Delta t^{+}}{\Delta t^{-}} \right) \left( x_{i,j} - x_{i-1,j} \right) \right)$$

$$T_{\xi} = \left( \frac{x_{i,j-1} - x_{i,j}}{\Delta s} \right) i + \left( \frac{y_{i,j-1} - y_{i,j}}{\Delta s} \right) j$$

$$T_{\eta} = \frac{dx}{dt} i + \frac{dy}{dt} j$$

$$\theta = \cos^{-1} \left( \frac{T_{\xi} \cdot T_{\eta}}{|T_{\xi}||T_{\eta}|} \right)$$

$$P(\xi, \eta) = P(\xi, 1) \cdot e^{-a(\eta - 1)/(\eta_{max} - 1)} + P(\xi, \eta_{max}) \cdot e^{-b(\eta_{max} - \eta)/(\eta_{max} - 1)}$$

$$Q(\xi, \eta) = Q(\xi, 1) \cdot e^{-c(\eta - 1)/(\eta_{max} - 1)} + Q(\xi, \eta_{max}) \cdot e^{-d(\eta_{max} - \eta)/(\eta_{max} - 1)}$$

In the electric field, Poisson equation can be given by

$$\frac{\partial^{2}V}{\partial\xi^{2}} \left[ \left( \frac{\partial\xi}{\partial x} \right)^{2} + \left( \frac{\partial\xi}{\partial y} \right)^{2} \right] + \frac{\partial^{2}V}{\partial\eta^{2}} \left[ \left( \frac{\partial\eta}{\partial x} \right)^{2} + \left( \frac{\partial\eta}{\partial y} \right)^{2} \right] + \\
2 \frac{\partial^{2}V}{\partial\xi\partial\eta} \left[ \left( \frac{\partial\xi}{\partial x} \right) \left( \frac{\partial\eta}{\partial x} \right) + \left( \frac{\partial\xi}{\partial y} \right) \left( \frac{\partial\eta}{\partial y} \right) \right] + , \qquad (3.20)$$

$$\frac{\partial V}{\partial\xi} \left[ \frac{\partial^{2}\xi}{\partial x^{2}} + \frac{\partial^{2}\xi}{\partial y^{2}} \right] + \frac{\partial V}{\partial\eta} \left[ \frac{\partial^{2}\eta}{\partial x^{2}} + \frac{\partial^{2}\eta}{\partial y^{2}} \right] = -\frac{q}{\varepsilon}$$

and the corona-current continuity equation can be written as

$$q^{2} = \varepsilon \left[ \left[ \left[ \left( \frac{\partial q}{\partial \xi} \right) \left( \frac{\partial \xi}{\partial x} \right) + \left( \frac{\partial q}{\partial \eta} \right) \left( \frac{\partial \eta}{\partial x} \right) \right] \times \left[ \left( \frac{\partial V}{\partial \xi} \right) \left( \frac{\partial \xi}{\partial x} \right) + \left( \frac{\partial V}{\partial \eta} \right) \left( \frac{\partial \eta}{\partial x} \right) \right] \right] + \left[ \left[ \left[ \left( \frac{\partial q}{\partial \xi} \right) \left( \frac{\partial \xi}{\partial y} \right) + \left( \frac{\partial q}{\partial \eta} \right) \left( \frac{\partial \eta}{\partial y} \right) \right] \times \left[ \left( \frac{\partial V}{\partial \xi} \right) \left( \frac{\partial \xi}{\partial y} \right) + \left( \frac{\partial V}{\partial \eta} \right) \left( \frac{\partial \eta}{\partial y} \right) \right] \right] \right]. (3.21)$$

The vorticity transport equation given by

$$\begin{split} &\frac{\partial \boldsymbol{\omega}}{\partial t} = \left[ \left[ \left( \frac{\partial \boldsymbol{\psi}}{\partial \boldsymbol{\xi}} \right) \left( \frac{\partial \boldsymbol{\xi}}{\partial \boldsymbol{x}} \right) + \left( \frac{\partial \boldsymbol{\psi}}{\partial \boldsymbol{\eta}} \right) \left( \frac{\partial \boldsymbol{\eta}}{\partial \boldsymbol{x}} \right) \right] \times \left[ \left( \frac{\partial \boldsymbol{\omega}}{\partial \boldsymbol{\xi}} \right) \left( \frac{\partial \boldsymbol{\xi}}{\partial \boldsymbol{y}} \right) + \left( \frac{\partial \boldsymbol{\omega}}{\partial \boldsymbol{\eta}} \right) \left( \frac{\partial \boldsymbol{\eta}}{\partial \boldsymbol{y}} \right) \right] \right] - \\ & \left[ \left[ \left( \frac{\partial \boldsymbol{\psi}}{\partial \boldsymbol{\xi}} \right) \left( \frac{\partial \boldsymbol{\xi}}{\partial \boldsymbol{y}} \right) + \left( \frac{\partial \boldsymbol{\psi}}{\partial \boldsymbol{\eta}} \right) \left( \frac{\partial \boldsymbol{\eta}}{\partial \boldsymbol{y}} \right) \right] \times \left[ \left( \frac{\partial \boldsymbol{\omega}}{\partial \boldsymbol{\xi}} \right) \left( \frac{\partial \boldsymbol{\xi}}{\partial \boldsymbol{x}} \right) + \left( \frac{\partial \boldsymbol{\omega}}{\partial \boldsymbol{\eta}} \right) \left( \frac{\partial \boldsymbol{\eta}}{\partial \boldsymbol{x}} \right) \right] \right] + \\ & \left[ \frac{\partial^{2} \boldsymbol{\psi}}{\partial \boldsymbol{\xi}^{2}} \left[ \left( \frac{\partial \boldsymbol{\xi}}{\partial \boldsymbol{x}} \right)^{2} + \left( \frac{\partial \boldsymbol{\xi}}{\partial \boldsymbol{y}} \right)^{2} \right] + \frac{\partial^{2} \boldsymbol{\psi}}{\partial \boldsymbol{\eta}^{2}} \left[ \left( \frac{\partial \boldsymbol{\eta}}{\partial \boldsymbol{x}} \right)^{2} + \left( \frac{\partial \boldsymbol{\eta}}{\partial \boldsymbol{y}} \right)^{2} \right] + \\ & \left[ \frac{\partial^{2} \boldsymbol{\psi}}{\partial \boldsymbol{\xi}^{2}} \left[ \left( \frac{\partial \boldsymbol{\xi}}{\partial \boldsymbol{x}} \right) \left( \frac{\partial \boldsymbol{\eta}}{\partial \boldsymbol{x}} \right) + \left( \frac{\partial \boldsymbol{\xi}}{\partial \boldsymbol{y}} \right) \left( \frac{\partial \boldsymbol{\eta}}{\partial \boldsymbol{\eta}} \right) \right] + \\ & \left[ \frac{\partial \boldsymbol{\psi}}{\partial \boldsymbol{\xi}} \left[ \frac{\partial^{2} \boldsymbol{\xi}}{\partial \boldsymbol{x}^{2}} + \frac{\partial^{2} \boldsymbol{\xi}}{\partial \boldsymbol{y}^{2}} \right] + \frac{\partial \boldsymbol{\psi}}{\partial \boldsymbol{\eta}} \left[ \frac{\partial^{2} \boldsymbol{\eta}}{\partial \boldsymbol{x}^{2}} + \frac{\partial^{2} \boldsymbol{\eta}}{\partial \boldsymbol{y}^{2}} \right] \right] - \\ & \left[ \left[ \left( \frac{\partial \boldsymbol{q}}{\partial \boldsymbol{\xi}} \right) \left( \frac{\partial \boldsymbol{\xi}}{\partial \boldsymbol{x}} \right) + \left( \frac{\partial \boldsymbol{q}}{\partial \boldsymbol{\eta}} \right) \left( \frac{\partial \boldsymbol{\eta}}{\partial \boldsymbol{x}} \right) \right] \times \left[ \left( \frac{\partial \boldsymbol{V}}{\partial \boldsymbol{\xi}} \right) \left( \frac{\partial \boldsymbol{\xi}}{\partial \boldsymbol{y}} \right) + \left( \frac{\partial \boldsymbol{V}}{\partial \boldsymbol{\eta}} \right) \left( \frac{\partial \boldsymbol{\eta}}{\partial \boldsymbol{y}} \right) \right] - \\ & \left[ \left[ \left( \frac{\partial \boldsymbol{q}}{\partial \boldsymbol{\xi}} \right) \left( \frac{\partial \boldsymbol{\xi}}{\partial \boldsymbol{y}} \right) + \left( \frac{\partial \boldsymbol{q}}{\partial \boldsymbol{\eta}} \right) \left( \frac{\partial \boldsymbol{\eta}}{\partial \boldsymbol{y}} \right) \right] \times \left[ \left( \frac{\partial \boldsymbol{V}}{\partial \boldsymbol{\xi}} \right) \left( \frac{\partial \boldsymbol{\xi}}{\partial \boldsymbol{x}} \right) + \left( \frac{\partial \boldsymbol{V}}{\partial \boldsymbol{\eta}} \right) \left( \frac{\partial \boldsymbol{\eta}}{\partial \boldsymbol{y}} \right) \right] - \\ & \left[ \left( \frac{\partial \boldsymbol{q}}{\partial \boldsymbol{\xi}} \right) \left( \frac{\partial \boldsymbol{\xi}}{\partial \boldsymbol{y}} \right) + \left( \frac{\partial \boldsymbol{q}}{\partial \boldsymbol{\eta}} \right) \left( \frac{\partial \boldsymbol{\eta}}{\partial \boldsymbol{y}} \right) \right] \times \left[ \left( \frac{\partial \boldsymbol{V}}{\partial \boldsymbol{\xi}} \right) \left( \frac{\partial \boldsymbol{\xi}}{\partial \boldsymbol{x}} \right) + \left( \frac{\partial \boldsymbol{V}}{\partial \boldsymbol{\eta}} \right) \left( \frac{\partial \boldsymbol{\eta}}{\partial \boldsymbol{y}} \right) \right] \right] - \\ & \left[ \left( \frac{\partial \boldsymbol{q}}{\partial \boldsymbol{\xi}} \right) \left( \frac{\partial \boldsymbol{\xi}}{\partial \boldsymbol{y}} \right) + \left( \frac{\partial \boldsymbol{q}}{\partial \boldsymbol{\eta}} \right) \left( \frac{\partial \boldsymbol{\eta}}{\partial \boldsymbol{y}} \right) \right] \times \left[ \left( \frac{\partial \boldsymbol{\xi}}{\partial \boldsymbol{\xi}} \right) \left( \frac{\partial \boldsymbol{\xi}}{\partial \boldsymbol{\eta}} \right) + \left( \frac{\partial \boldsymbol{\eta}}{\partial \boldsymbol{\eta}} \right) \left( \frac{\partial \boldsymbol{\eta}}{\partial \boldsymbol{\eta}} \right) \right] \right] \right] \right] \right]$$

the transformed equation of stream function-vorticity relation can be written as

$$\frac{\partial^{2} \psi}{\partial \xi^{2}} \left[ \left( \frac{\partial \xi}{\partial x} \right)^{2} + \left( \frac{\partial \xi}{\partial y} \right)^{2} \right] + \frac{\partial^{2} \psi}{\partial \eta^{2}} \left[ \left( \frac{\partial \eta}{\partial x} \right)^{2} + \left( \frac{\partial \eta}{\partial y} \right)^{2} \right] +$$

$$2 \frac{\partial^{2} \psi}{\partial \xi \partial \eta} \left[ \left( \frac{\partial \xi}{\partial x} \right) \left( \frac{\partial \eta}{\partial x} \right) + \left( \frac{\partial \xi}{\partial y} \right) \left( \frac{\partial \eta}{\partial y} \right) \right] +$$

$$\frac{\partial \psi}{\partial \xi} \left[ \frac{\partial^{2} \xi}{\partial x^{2}} + \frac{\partial^{2} \xi}{\partial y^{2}} \right] + \frac{\partial \psi}{\partial \eta} \left[ \frac{\partial^{2} \eta}{\partial x^{2}} + \frac{\partial^{2} \eta}{\partial y^{2}} \right] = -\boldsymbol{\omega}$$
(3.23)

And the energy equation is expressed as

$$\frac{\partial T}{\partial t} = \left[ \left[ \left( \frac{\partial \boldsymbol{\omega}}{\partial \xi} \right) \left( \frac{\partial \xi}{\partial x} \right) + \left( \frac{\partial \boldsymbol{\omega}}{\partial \eta} \right) \left( \frac{\partial \eta}{\partial x} \right) \right] \times \left[ \left( \frac{\partial T}{\partial \xi} \right) \left( \frac{\partial \xi}{\partial y} \right) + \left( \frac{\partial T}{\partial \eta} \right) \left( \frac{\partial \eta}{\partial y} \right) \right] \right] - \left[ \left[ \left( \frac{\partial \boldsymbol{\omega}}{\partial \xi} \right) \left( \frac{\partial \xi}{\partial y} \right) + \left( \frac{\partial \boldsymbol{\omega}}{\partial \eta} \right) \left( \frac{\partial \eta}{\partial y} \right) \right] \times \left[ \left( \frac{\partial T}{\partial \xi} \right) \left( \frac{\partial \xi}{\partial x} \right) + \left( \frac{\partial T}{\partial \eta} \right) \left( \frac{\partial \eta}{\partial x} \right) \right] \right] + \left[ \frac{\partial^2 T}{\partial \xi^2} \left[ \left( \frac{\partial \xi}{\partial x} \right)^2 + \left( \frac{\partial \xi}{\partial y} \right)^2 \right] + \frac{\partial^2 T}{\partial \eta^2} \left[ \left( \frac{\partial \eta}{\partial x} \right)^2 + \left( \frac{\partial \eta}{\partial y} \right)^2 \right] + \left[ \frac{\partial^2 T}{\partial \xi \partial \eta} \left[ \left( \frac{\partial \xi}{\partial x} \right) \left( \frac{\partial \eta}{\partial x} \right) + \left( \frac{\partial \xi}{\partial y} \right) \left( \frac{\partial \eta}{\partial y} \right) \right] + \left[ \frac{\partial T}{\partial \xi} \left[ \frac{\partial^2 \xi}{\partial x^2} + \frac{\partial^2 \xi}{\partial y^2} \right] + \frac{\partial T}{\partial \eta} \left[ \frac{\partial^2 \eta}{\partial x^2} + \frac{\partial^2 \eta}{\partial y^2} \right] \right] \right] . \quad (3.24)$$

### 3.5 General Balance Laws

The general set of balance laws governing single-phase electro-magneto-hydrodynamics flow consists of two groups of equations. One group is for the electromagnetic field, the other is for the thermomechanical field. This set should be supplemented by the material constitutive equations.

The electromagnetic balance laws are represented by the Maxwell's equations. Using a vector operator form, the Maxwell's equations can be written in the rationalized system as follows:

$$\nabla \cdot \mathbf{D} = \mathbf{q}_{e} \text{ (Gauss' law)}, \tag{3.25}$$

$$\nabla \cdot \mathbf{B} = 0$$
 (conservation of magnetic flux), (3.26)

$$\nabla \times \mathbf{E} = -\frac{\partial \mathbf{B}}{\partial t} \text{ (Faraday's law)}, \tag{3.27}$$

$$\nabla \times \mathbf{H} = -\frac{\partial \mathbf{D}}{\partial t} + \mathbf{J} \text{ (Ampere) Maxwell's law)}. \tag{3.28}$$

This set of equations defines the divergence and curl of the electric and magnetic field. It is well known that a vector field can be completely determined if its divergence and curl are known. The relations between flux density and field intensity vectors in the polarizable and magnetizable medium are given by

$$D = \varepsilon_0 E + P, \qquad (3.29)$$

$$B = \mu_0 (H + M). \tag{3.30}$$

Polarization and magnetization strongly depend on the material and can be estimated from the constitutive equations. The electric charge conservation equation is derived from a combination of Gauss' law and Ampere-Maxwell's law as

$$\frac{\partial \mathbf{q}_{e}}{\partial t} + \nabla \cdot \mathbf{J} = 0. \tag{3.31}$$

This equation accounts for all types of charged species together since charge transport takes place by charge carrier motion and by charge jumping from one carrier to another.

The balance laws of the thermomechanical field are comprised of three conservation laws and the second law of thermodynamics. The equations of conservation of mass, linear momentum, and energy are expressed as

$$\frac{\partial \rho}{\partial t} + \nabla \cdot (\rho \mathbf{v}) = 0, \tag{3.32}$$

$$\rho \frac{\mathrm{Dv}}{\mathrm{D}t} = \nabla \cdot \mathbf{t} + \rho \mathbf{f} + \mathbf{F}^{\mathrm{em}}, \tag{3.33}$$

$$\rho \frac{D\hat{\mathbf{u}}}{Dt} = \mathbf{t} : \mathbf{d} + \mathbf{Q}_{h} + \nabla \cdot \mathbf{q} + \rho \hat{\mathbf{E}} \cdot \frac{D(\rho^{-1}P)}{Dt} - \hat{\mathbf{M}} \cdot \frac{DB}{Dt} + \mathbf{J}_{c} \cdot \hat{\mathbf{E}}, \qquad (3.34)$$

respectively. Here, the electromagnetic body force per unit volume is given by

$$F^{em} = q_e E + J \times B + (\nabla E) \cdot P + (\nabla B) \cdot M + \nabla (v(P \times B)) + \frac{\partial}{\partial t} (P \times B).$$
 (3.35)

The final balance law comes from the second law of thermodynamics. This is represented by the Clausius-Duhem inequality

$$\rho \frac{Ds}{Dt} - \nabla \cdot (T^{-1}q) = T^{-1}Q_h \ge 0.$$
 (3.36)

By using the energy conservation (Eq. (3.34)), and by introducing the generalized Helmholtz free energy,

$$\psi = \hat{\mathbf{u}} - \mathbf{T} \mathbf{s} - \rho^{-1} \hat{\mathbf{E}} \cdot \mathbf{P}, \qquad (3.37)$$

the inequality can be rewritten as

$$\rho \gamma = -\rho \left( \frac{D\psi}{Dt} + s \frac{DT}{Dt} \right) + \mathbf{t} : \mathbf{d} + \mathbf{T}^{-1} \mathbf{q} \cdot \nabla \mathbf{T} - \mathbf{P} \cdot \frac{D\hat{\mathbf{E}}}{Dt} - \hat{\mathbf{M}} \cdot \frac{DB}{Dt} + \mathbf{J}_{c} \cdot \hat{\mathbf{E}} \ge 0. \quad (3.38)$$

# 3.6 Constitutive Equations

#### 3.6.1 General Constitutive Relations

In order to completely determine the electromagnetic and thermo mechanical fields, the balance laws must be supplemented by the constitutive equations, since the number of unknowns is larger than the number of balance equations. Given the mechanical body force and the internal heat source, additional information about the polarization and magnetization, stress tensor, electric conduction, and conduction heat transfer are required. The most general theory of constitutive equations has been developed using a continuum approach. Since the second-order model starts with the general non-linear theory, some of the essentials will be reproduced here. For simple rate-dependent, memory-independent, and isotropic fluids, the set of independent variables for the constitutive relations can be chosen to be d,  $\hat{E}$ , B,  $\nabla T$ , T, and  $\rho$ . In other words, any field variable (scalar, vector, and tensor) which must be defined by a constitutive relation can be represented as a function of these variables. Therefore,  $\psi$  takes the form

$$\psi = \psi(d, \hat{E}, B, \nabla T, T, \rho), \qquad (3.39)$$

where the assumption of a medium with purely instantaneous response has been also made. Similar equations with the same arguments are valid for the stress tensor, electric conduction current vector, etc. Substitution of Eq. (3.39) into Eq. (3.38) yields an implication of the following restrictions on the constitutive equations:

$$\frac{\partial \psi}{\partial \mathbf{d}} = 0, \frac{\partial \psi}{\partial \nabla \mathbf{T}} = 0, \mathbf{s} = -\frac{\partial \psi}{\partial \mathbf{T}}, \mathbf{P} = -\rho \frac{\partial \psi}{\partial \hat{\mathbf{E}}}, \hat{\mathbf{M}} = -\rho \frac{\partial \psi}{\partial \mathbf{B}}, \tag{3.40}$$

$$\rho \gamma = \mathbf{t} : \mathbf{d} + \mathbf{T}^{-1} \mathbf{q} \cdot \nabla \mathbf{T} + \mathbf{J}_{c} \cdot \hat{\mathbf{E}} \ge 0, \tag{3.41}$$

where the deviator part of stress tensor and the modified hydrostatic pressure are defined by

$$\mathbf{t} = -\varphi \mathbf{I} + \tau, \varphi = \rho^2 \frac{\partial \psi}{\partial \rho}. \tag{3.42}$$

Then, the only possible dependence of the free energy upon EK and B is through its scalar invariants defined by

$$I_1 = \hat{E} \cdot \hat{E}, I_2 = B \cdot B, I_3 = (\hat{E} \cdot B)^2.$$
 (3.43)

Consequently, the general form of free energy (Eq. (3.39)) changes into

$$\psi = \psi(I_1, I_2, I_3, T, \rho). \tag{3.44}$$

From Eqs. (3.40) and (3.44) the polarization vector and magnetomotive intensity vector can be found as

$$P = -2\rho \left( \frac{\partial \psi}{\partial I_1} \hat{E} + \frac{\partial \psi}{\partial I_3} (\hat{E} \cdot B) B \right) \equiv \varepsilon_0 \chi_e \hat{E} + \lambda (\hat{E} \cdot B) B, \qquad (3.45)$$

$$\hat{\mathbf{M}} = -2\rho \left( \frac{\partial \psi}{\partial \mathbf{I}_2} \mathbf{B} + \frac{\partial \psi}{\partial \mathbf{I}_3} (\hat{\mathbf{E}} \cdot \mathbf{B}) \hat{\mathbf{E}} \right) = \frac{\chi_e}{\mu_0} \mathbf{B} + \lambda (\hat{\mathbf{E}} \cdot \mathbf{B}) \hat{\mathbf{E}}. \tag{3.46}$$

Here, notice that  $\chi_e$ ,  $\chi_B$ , and  $\lambda$  are general functions of  $I_1 - I_3$  and T,  $\rho$ .

Using a similar reasoning, the symmetric deviator stress tensor for a non-linear fluid, which is defined by Eq. (3.42), can be expressed as

$$\begin{split} \tau &= \alpha_0 \mathbf{I} + \alpha_1 \mathbf{d} + \alpha_2 \mathbf{d}^2 + \alpha_3 \hat{\mathbf{E}} \otimes \hat{\mathbf{E}} + \alpha_4 \mathbf{B} \otimes \mathbf{B} + \alpha_5 \nabla \mathbf{T} \otimes \nabla \mathbf{T} + \alpha_6 (\hat{\mathbf{E}} \otimes \mathbf{d} \cdot \hat{\mathbf{E}})_{\mathrm{S}} + \\ \alpha_7 (\hat{\mathbf{E}} \otimes \mathbf{d}^2 \cdot \hat{\mathbf{E}})_{\mathrm{S}} + \alpha_8 (\nabla \mathbf{T} \otimes \mathbf{d} \cdot \nabla \mathbf{T})_{\mathrm{S}} + \alpha_9 (\nabla \mathbf{T} \otimes \mathbf{d}^2 \cdot \nabla \mathbf{T})_{\mathrm{S}} + \alpha_{10} (\mathbf{d} \cdot \mathbf{W})_{\mathrm{S}} + \\ \alpha_{11} \mathbf{W} \cdot \mathbf{d} \cdot \mathbf{W} + \alpha_{12} (\mathbf{d}^2 \cdot \mathbf{W}) + \alpha_{13} (\mathbf{W} \cdot \mathbf{d} \cdot \mathbf{W}^2) + \alpha_{14} (\hat{\mathbf{E}} \otimes \nabla \mathbf{T})_{\mathrm{S}} + \\ \alpha_{15} (\mathbf{W} \cdot \hat{\mathbf{E}} \otimes \mathbf{W} \cdot \hat{\mathbf{E}}) + \alpha_{16} (\hat{\mathbf{E}} \otimes \mathbf{W} \cdot \hat{\mathbf{E}})_{\mathrm{S}} + \alpha_{17} (\mathbf{W} \cdot \hat{\mathbf{E}} \otimes \mathbf{W}^2 \cdot \hat{\mathbf{E}})_{\mathrm{S}} + \\ \alpha_{18} (\mathbf{W} \cdot \nabla \mathbf{T}) \otimes (\mathbf{W} \cdot \nabla \mathbf{T}) + \alpha_{19} \nabla \mathbf{T} \otimes (\mathbf{W} \cdot \nabla \mathbf{T}) + \alpha_{20} ((\mathbf{W} \cdot \nabla \mathbf{T}) \otimes (\mathbf{W}^2 \cdot \nabla \mathbf{T}))_{\mathrm{S}} + \\ \alpha_{21} (\mathbf{d} \cdot (\hat{\mathbf{E}} \otimes \nabla \mathbf{T} - \nabla \mathbf{T} \otimes \hat{\mathbf{E}}))_{\mathrm{S}} + \alpha_{22} (\mathbf{W} \cdot (\hat{\mathbf{E}} \otimes \nabla \mathbf{T} - \nabla \mathbf{T} \otimes \hat{\mathbf{E}}))_{\mathrm{S}}. \end{split}$$

In this expression, W is a skew-symmetric tensor defined by,  $W_{kl} = \varepsilon_{kml} B_m$ , and the subscript S means the symmetric part of a dyadic. Electric conduction current and conduction heat flux in the most general case can be expressed as

$$\begin{split} &J_{e} = \sigma_{1}\hat{E} + \sigma_{2}d\cdot\hat{E} + \sigma_{3}d^{2}\cdot\hat{E} + \sigma_{4}\nabla T + \sigma_{5}d\cdot\nabla T + \sigma_{6}d^{2}\cdot\nabla T + \sigma_{7}\hat{E}\times B + \\ &\sigma_{8}\nabla T\times B + \sigma_{9}(d\cdot(\hat{E}\times B) - (d\cdot\hat{E})\times B) + \sigma_{10}(B\cdot\hat{E})B + \sigma_{11}(B\cdot\nabla T)B + \\ &\sigma_{12}(d\cdot(\nabla T\times B) - (d\cdot\nabla T)\times B), \end{split} \tag{3.48}$$

$$\begin{split} \mathbf{q} &= \kappa_{1} \nabla \mathbf{T} + \kappa_{2} \mathbf{d} \cdot \nabla \mathbf{T} + \kappa_{3} \mathbf{d}^{2} \cdot \nabla \mathbf{T} + \kappa_{4} \hat{\mathbf{E}} + \kappa_{5} \mathbf{d} \cdot \hat{\mathbf{E}} + \kappa_{6} \mathbf{d}^{2} \cdot \hat{\mathbf{E}} + \kappa_{7} \nabla \mathbf{T} \times \mathbf{B} + \kappa_{8} \hat{\mathbf{E}} \times \mathbf{B} + \kappa_{9} (\mathbf{d} \cdot (\nabla \mathbf{T} \times \mathbf{B}) - (\mathbf{d} \cdot \nabla \mathbf{T}) \times \mathbf{B}) + \kappa_{10} (\mathbf{B} \cdot \nabla \mathbf{T}) \mathbf{B} + \kappa_{11} (\mathbf{B} \cdot \hat{\mathbf{E}}) \mathbf{B} + \kappa_{12} (\mathbf{d} \cdot (\hat{\mathbf{E}} \times \mathbf{B}) - (\mathbf{d} \cdot \hat{\mathbf{E}}) \times \mathbf{B}), \end{split}$$
(3.49)

respectively. All of the physical properties of the media in Eqs. (3.47)-(3.49) are functions of the scalar invariants and thermodynamic states. Specifically,

$$\alpha_{i} = \alpha_{i}(I_{n}, T, \rho), \sigma_{j} = \sigma_{j}(I_{n}, T, \rho), \kappa_{j} = \kappa_{j}(I_{n}, T, \rho)$$

$$(i = 0, 1, ..., 22, j = 0, 1, ..., 12, n = 0, 1, ..., 27).$$
(3.50)

The irreducible set of joint scalar invariants, which can be constructed from d,  $\hat{E}$ , B,  $\nabla T$  including the three already defined by Eq. (3.43), consists of 27 invariants:

$$\begin{split} &\mathbf{I}_{4} = \operatorname{tr}(\mathbf{d}) = \nabla \cdot \mathbf{v}, \mathbf{I}_{5} = \operatorname{tr}(\mathbf{d}^{2}), \mathbf{I}_{6} = \operatorname{tr}(\mathbf{d}^{3}), \mathbf{I}_{7} = \nabla \mathbf{T} \cdot \nabla \mathbf{T}, \mathbf{I}_{8} = \hat{\mathbf{E}} \cdot \nabla \mathbf{T}, \\ &\mathbf{I}_{9} = \hat{\mathbf{E}} \cdot \mathbf{d}^{2} \cdot \hat{\mathbf{E}}, \mathbf{I}_{10} = \hat{\mathbf{E}}^{2} \cdot \mathbf{d}^{2} \cdot \hat{\mathbf{E}}, \mathbf{I}_{11} = \nabla \mathbf{T} \cdot \mathbf{d} \cdot \nabla \mathbf{T}, \mathbf{I}_{12} = \nabla \mathbf{T} \cdot \mathbf{d}^{2} \cdot \nabla \mathbf{T}, \\ &\mathbf{I}_{13} = \mathbf{B} \cdot \mathbf{d} \cdot \mathbf{B}, \mathbf{I}_{14} = \mathbf{B} \cdot \mathbf{d}^{2} \cdot \mathbf{B}, \mathbf{I}_{15} = \mathbf{B} \cdot ((\mathbf{d} \cdot \mathbf{B}) \times (\mathbf{d}^{2} \cdot \mathbf{B})), \mathbf{I}_{16} = (\mathbf{B} \cdot \nabla \mathbf{T})^{2}, \\ &\mathbf{I}_{17} = \hat{\mathbf{E}} \cdot \mathbf{d} \cdot \nabla \mathbf{T}, \mathbf{I}_{18} = \hat{\mathbf{E}} \cdot \mathbf{d}^{2} \cdot \nabla \mathbf{T}, \mathbf{I}_{19} = \hat{\mathbf{E}} \cdot (\nabla \mathbf{T} \times \mathbf{B}), \mathbf{I}_{20} = (\hat{\mathbf{E}} \cdot \mathbf{B})(\nabla \mathbf{T} \cdot \mathbf{B}), \\ &\mathbf{I}_{21} = \hat{\mathbf{E}} \cdot (\mathbf{B} \times (\mathbf{d} \cdot \hat{\mathbf{E}})), \mathbf{I}_{22} = \nabla \mathbf{T} \cdot (\mathbf{B} \times (\mathbf{d} \cdot \nabla \mathbf{T})), \mathbf{I}_{23} = \hat{\mathbf{E}} \cdot (\mathbf{B} \times (\mathbf{d}^{2} \cdot \hat{\mathbf{E}})), \\ &\mathbf{I}_{24} \nabla \mathbf{T} \cdot (\mathbf{B} \times (\mathbf{d}^{2} \cdot \nabla \mathbf{T})), \mathbf{I}_{25} = (\hat{\mathbf{E}} \cdot \mathbf{B}) \hat{\mathbf{E}} \cdot (\mathbf{B} \times (\mathbf{d} \cdot \mathbf{B})), \\ &\mathbf{I}_{26} = (\nabla \mathbf{T} \cdot \mathbf{B}) \nabla \mathbf{T} \cdot (\mathbf{B} \times (\mathbf{d} \cdot \mathbf{B})), \mathbf{I}_{27} = \hat{\mathbf{E}} \cdot (\mathbf{B} \times (\mathbf{d} \cdot \nabla \mathbf{T})) + \nabla \mathbf{T} \cdot (\mathbf{B} \times (\mathbf{d} \cdot \hat{\mathbf{E}})). \end{split}$$

### 3.6.2 Second-Order Theory of Constitutive Equations

Because so many joint invariants are involved in the constitutive equations for the stress tensor, conduction current, and heat flux vector, they cannot be used in the general form for practical applications. While the linear theory is relatively simple, it is inconsistent and inappropriate for cases where non-linear and/or cross effects are important.

A fully consistent non-linear combined electro-magneto-hydrodynamics model, with a somewhat reduced complexity, may be called a second-order theory. The underlying assumption is that the electromagnetic fields, rate of strain, and temperature gradient are relatively small. More precisely, the following two assumptions will be made in the constitutive equations. First, only the terms up to second order in d,  $\hat{E}$ , B,  $\nabla T$  will be retained. Second, terms of second order and higher in d will be neglected as in the case of conventional Newtonian fluids. The application of these assumptions to the general form of the previous section causes the constitutive equations for  $\psi$ , P,  $\hat{M}$ , and  $\varphi$  to simplify as follows:

$$\psi = \psi(\mathbf{I}_1, \mathbf{I}_2, \mathbf{T}, \rho) = \psi_0 - \frac{1}{2\rho} \left( \varepsilon_0 \chi_e \mathbf{I}_1 + \frac{\chi_e}{\mu_0} \mathbf{I}_2 \right), \tag{3.52}$$

$$\varphi = \rho^2 \frac{\partial \psi_0}{\partial \rho} - \frac{\varepsilon_0 \rho^2}{2} \frac{\partial}{\partial \rho} \left( \frac{\chi_e}{\rho} \right) I_1 - \frac{\rho^2}{2\mu_0} \frac{\partial}{\partial \rho} \left( \frac{\chi_B}{\rho} \right) I_2 \equiv \varphi_0 + \varphi_e + \varphi_m, \qquad (3.53)$$

$$P = \varepsilon_0 \chi_e \hat{E} = \varepsilon_p \hat{E}, \hat{M} = \frac{\chi_B}{\mu_0} B = \frac{B}{\mu_m}.$$
 (3.54)

This indicates a medium with purely instantaneous response. Here,  $\psi_0$ ,  $\chi_e$ ,  $\chi_B$  and  $\varphi_0$ ,  $\varphi_e/I_1$ ,  $\varphi_m/I_2$  depend on T and  $\rho$  only. By the same reasoning, the deviator part of the Cauchy stress tensor, electric conduction current, and conduction heat flux can be consistently simplified as follows:

$$\tau = (\alpha_{00} + \alpha_{01}I_{1} + \alpha_{02}I_{2} + \alpha_{04}I_{4} + \alpha_{07}I_{7} + \alpha_{08}I_{8})I + \alpha_{1}d + \alpha_{3}\hat{E} \otimes \hat{E} + \alpha_{4}B \otimes B + \alpha_{5}\nabla T \otimes \nabla T + \alpha_{10}(d \cdot W)_{5} + \alpha_{14}(\hat{E} \otimes \nabla T)_{5},$$
(3.55)

$$\begin{split} &J_{e} = (\sigma_{1} + \sigma_{1b}I_{4})\hat{E} + \sigma_{2}d \cdot \hat{E} + (\sigma_{4} + \sigma_{4b}I_{4})\nabla T + \sigma_{5}d \cdot \nabla T + \sigma_{7}\hat{E} \times B + \\ &\sigma_{8}\nabla T \times B, \end{split} \tag{3.56}$$

$$q = (\kappa_1 + \kappa_{1b}I_4)\nabla T + \kappa_2 d \cdot \nabla T + (\kappa_4 + \kappa_{4b}I_4)\hat{E} + \kappa_5 d \cdot \hat{E} + \kappa_7 \nabla T \times B + \kappa_2 \hat{E} \times B.$$
(3.57)

Here, all coefficients denoted with  $\alpha$ ,  $\sigma$ ,  $\kappa$  are general functions of T and  $\rho$ . Note that Eq. (3.42) still holds with Eqs. (3.53) and (3.55).

The possible restrictions imposed on the coefficients can be sought through the inequality. First, one of the immediate implication of Eq. (3.41) is

$$\tau = 0 \text{ when } d = 0, \hat{E} = 0, \nabla T = 0.$$
 (3.58)

From Eq. (3.55) it follows that this implies

$$\alpha_{00} = \alpha_{02} = 0, \, \alpha_4 = 0. \tag{3.59}$$

Hence, when d,  $\hat{E}$ , B, and  $\nabla T$  are not zero, the nonnegative irreversible entropy generation function can be computed as

$$\rho \gamma = (\alpha_{1}d : d + \alpha_{04}(tr(d))^{2}) + (\sigma_{1}(\hat{E} \cdot \hat{E}) + (T^{-1}\kappa_{4} + \sigma_{4})(\hat{E} \cdot \nabla T) + T^{-1}\kappa_{1}(\nabla T \cdot \nabla T)) + (\alpha_{3} + \sigma_{2})(\hat{E} \cdot d \cdot \hat{E}) + (\alpha_{5} + T^{-1}\kappa_{2}) \times (\nabla T \cdot d \cdot \nabla T) + \alpha_{10}(d \cdot W)_{s} : d + ((\alpha_{01} + \sigma_{1b})(\hat{E} \cdot \hat{E}) + (\alpha_{08} + T^{-1}\kappa_{4b} + \sigma_{4b})(\hat{E} \cdot \nabla T) + (\alpha_{07} + T^{-1}\kappa_{1b}) \times (\nabla T \cdot \nabla T))tr(d) + (\alpha_{14} + T^{-1}\kappa_{5} + \sigma_{5}) \times (\hat{E} \cdot d \cdot \nabla T) + (T^{-1}\kappa_{8} - \sigma_{8})\nabla T \cdot (\hat{E} \times B).$$
(3.60)

Note that the two expressions in braces of the first line are quadratic in d and  $\hat{E}$ ,  $\nabla T$ , while each of the remaining scalar terms are cubic in d,  $\hat{E}$ , B,  $\nabla T$ . In order that

this function should be non-negative definite for any values of d,  $\hat{E}$ , B,  $\nabla T$ , the following relations among the physical properties must be satisfied:

$$\alpha_{1} \geq 0, 3\alpha_{04} + \alpha_{1} \geq 0, \sigma_{1} \geq 0, \kappa_{1} \geq 0, (T^{-1}\kappa_{4} - \sigma_{4})^{2} \leq 4T^{-1}\kappa_{1}\sigma_{1}, \alpha_{3} = -\sigma_{2},$$

$$\alpha_{5} = -T^{-1}\kappa_{2}, \alpha_{10} = 0, \alpha_{01} = -\sigma_{1b}, \alpha_{08} = -T^{-1}\kappa_{4b} - \sigma_{4b}, \alpha_{07} = -T^{-1}\kappa_{1b},$$

$$\alpha_{14} = -T^{-1}\kappa_{5} - \sigma_{5}, \alpha_{8} = -T^{-1}\kappa_{8}.$$
(3.61)

Therefore, the final expression for the deviator part of the Cauchy stress tensor simplifies to

$$\tau = -(\sigma_{1b}I_{1} - \alpha_{04}I_{4} + T^{-1}\kappa_{1b}I_{7} + (T^{-1}\kappa_{4b} + \sigma_{4b})I_{15})I + \alpha_{1}d - \sigma_{2}\hat{E} \otimes \hat{E} - T^{-1}\kappa_{2}\nabla T \otimes \nabla T - (T^{-1}\kappa_{5} + \sigma_{5})(\hat{E} \otimes \nabla T)_{S}.$$
(3.62)

There is a slight change in the expression for the electric conduction current from Eq. (3.56) into

$$\begin{aligned} \mathbf{J}_{e} &= (\sigma_{1} + \sigma_{1b}\mathbf{I}_{4})\hat{\mathbf{E}} + \sigma_{2}\mathbf{d} \cdot \hat{\mathbf{E}} + (\sigma_{4} + \sigma_{4b}\mathbf{I}_{4})\nabla\mathbf{T} + \sigma_{5}\mathbf{d} \cdot \nabla\mathbf{T} + \sigma_{7}\hat{\mathbf{E}} \times \mathbf{B} + \\ \mathbf{T}^{-1}\kappa_{8}\nabla\mathbf{T} \times \mathbf{B}, \end{aligned} \tag{3.63}$$

while the conduction heat flux, Eq. (3.57), remains unchanged.

## 3.6.3 Constitutive Equations for Incompressible Flows

In the case of an incompressible fluid, all terms that contain  $I_4 = (= \operatorname{tr}(d) = \nabla \cdot v)$  reduce to zero. This means that in electro-magneto-hydrodynamics, there is no dependence of physical properties upon density. The equation for the modified hydrostatic pressure u can be written as

$$\varphi = \rho^2 \frac{\partial \psi_0}{\partial \rho} - \frac{\varepsilon_0 \chi_e}{2} (\hat{\mathbf{E}} \cdot \hat{\mathbf{E}}) + \frac{\chi_B}{2\mu_0} (\mathbf{B} \cdot \mathbf{B}) \equiv p_0 + p_e + p_m, \qquad (3.64)$$

while the expressions for the polarization and magnetization (Eq. (3.54)) remain unchanged. Similarly, the deviator part of the stress tensor and conduction vectors reduces from Eqs. (3.62), (3.63) and (3.57) to

$$\tau = 2\mu_{v}d - \sigma_{2}\hat{\mathbf{E}} \otimes \hat{\mathbf{E}} - \mathbf{T}^{-1}\kappa_{2}\nabla\mathbf{T} \otimes \nabla\mathbf{T} - (\mathbf{T}^{-1}\kappa_{5} + \sigma_{5})(\hat{\mathbf{E}} \otimes \nabla\mathbf{T})_{S}, \qquad (3.65)$$

$$J_{e} = \sigma_{1}\hat{E} + \sigma_{2}d \cdot \hat{E} + \sigma_{4}\nabla T + \sigma_{5}d \cdot \nabla T + \sigma_{7}\hat{E} \times B + T^{-1}\kappa_{8}\nabla T \times B, \qquad (3.66)$$

$$q = \kappa_1 \nabla T + \kappa_2 d \cdot \nabla T + \kappa_4 \hat{E} + \kappa_5 d \cdot \hat{E} + \kappa_7 \nabla T \times B + \kappa_8 \hat{E} \times B.$$
 (3.67)

Here, the coefficient of fluid viscosity is defined as  $\mu_v = \sigma_1/2$ . Notice that in the electro-magneto-hydrodynamics, the physical properties of the media,  $\chi_e$ ,  $\chi_e$ ;  $\mu_v$ ;  $\sigma_1$ ,  $\sigma_2$ ,  $\sigma_4$ ,  $\sigma_5$ ,  $\sigma_7$ ;  $\kappa_1$ ,  $\kappa_2$ ,  $\kappa_4$ ,  $\kappa_5$ ,  $\kappa_7$ ,  $\kappa_8$ , can be either constants or functions of temperature only. The pressure, p, must be determined such that the incompressibility condition,  $\nabla \cdot \mathbf{v} = 0$ , should be satisfied everywhere in the flow-field. The magnetic field intensity H and the total magnetization vector M can be readily determined by substituting Eq. (3.54) into Eq. (3.30).

# 3.7 Non-Linear Electro-Magneto-Hydrodynamics Model

A full system of governing equations for the incompressible flows under the combined effect of electromagnetic forces is described in this section by using the constitutive equations which have been derived through the second-order theory. A slight modification, which is called the Boussinesq approximation, of the conservation laws is needed to be compatible with incompressible flows. In the Boussinesq approximation, the variation of density is kept only in the gravity force of the momentum equation. A linear dependence of density on temperature is assumed there. If the thermal buoyancy is the only mechanical body force acting on the fluid, the linear momentum equation can be rewritten

$$\rho \frac{\mathrm{D}\mathbf{v}}{\mathrm{D}t} = \rho^{-1} (\nabla \cdot \mathbf{t} + \mathrm{F}^{\mathrm{em}}) - \mathrm{g}(1 - \alpha (\mathrm{T} - \mathrm{T}_0)) \mathbf{i}_3. \tag{3.68}$$

Here,  $\alpha$  is the coefficient of thermal expansion of the fluid, and  $i_3$  is the unit vector directing vertically upward. It is a common practice to neglect the thermal buoyancy, and to use  $\alpha = 0$  in forced convection studies. For incompressible flows, the energy conservation (Eq. (3.34)) can be rewritten in terms of temperature, T, as

$$\rho C_{p} \frac{DT}{Dt} = \frac{Dp}{Dt} + \mathbf{t} : d + Q_{h} + \nabla \cdot \mathbf{q} + \hat{\mathbf{E}} \cdot \frac{DP}{Dt} - \hat{\mathbf{M}} \cdot \frac{DB}{Dt} + \mathbf{J}_{c} \cdot \hat{\mathbf{E}} . \tag{3.69}$$

By substituting the relevant constitutive equations into all balance laws, the following system of governing equations can be obtained.

Maxwell's equations (Eqs. (3.25)-(3.28)):

$$\nabla \cdot (\varepsilon_0 \mathbf{E} + \varepsilon_p \hat{\mathbf{E}}) \mathbf{B} = \mathbf{q}_e \,, \tag{3.70}$$

$$\nabla \cdot \mathbf{B} = 0, \tag{3.71}$$

$$\nabla \times \mathbf{E} = -\frac{\partial \mathbf{B}}{\partial t},\tag{3.72}$$

$$\nabla \times \left(\frac{\mathbf{B}}{\mu} + \varepsilon_{p} \mathbf{v} \times \hat{\mathbf{E}}\right) = \frac{\partial}{\partial t} (\varepsilon_{0} \mathbf{E} + \varepsilon_{p} \hat{\mathbf{E}}) + \mathbf{q}_{e} \mathbf{v} + \sigma_{1} \hat{\mathbf{E}} + \sigma_{2} \mathbf{d} \cdot \hat{\mathbf{E}} + \sigma_{4} \nabla \mathbf{T} + \sigma_{5} \mathbf{d} \cdot \nabla \mathbf{T} + \sigma_{7} \hat{\mathbf{E}} \times \mathbf{B} + \mathbf{T}^{-1} \kappa_{8} \nabla \mathbf{T} \times \mathbf{B}.$$
(3.73)

Navier-Stokes equations:

$$\nabla \cdot \mathbf{v} = 0, \tag{3.74}$$

$$\rho \frac{\mathrm{D} \mathrm{v}}{\mathrm{D} t} = -\rho \mathrm{g} (1 - \alpha (\mathrm{T} - \mathrm{T}_{0})) \mathrm{i}_{3} - \nabla (\mathrm{p}_{0} + \mathrm{p}_{e} + \mathrm{p}_{m}) + \nabla \cdot (\mu_{\mathrm{v}} (\nabla \mathrm{v} + \nabla \mathrm{v}^{\mathrm{t}})) - \nabla \cdot (\sigma_{2} (\hat{\mathrm{E}} \otimes \hat{\mathrm{E}})) - \nabla \cdot (\mathrm{T}^{-1} \kappa_{2} (\nabla \mathrm{T} \otimes \nabla \mathrm{T})) - \nabla \cdot (\mathrm{T}^{-1} \kappa_{5} + \sigma_{5}) (\hat{\mathrm{E}} \otimes \nabla \mathrm{T})_{\mathrm{S}} + q_{e} \hat{\mathrm{E}} + \sigma_{1} \hat{\mathrm{E}} \times \mathrm{B} + \sigma_{2} \mathrm{d} \cdot \hat{\mathrm{E}} \times \mathrm{B} + \sigma_{4} \nabla \mathrm{T} \times \mathrm{B} + \sigma_{5} \mathrm{d} \cdot \nabla \mathrm{T} \times \mathrm{B} + \sigma_{7} (\hat{\mathrm{E}} \times \mathrm{B}) \times \mathrm{B} + \mathrm{T}^{-1} \kappa_{8} (\nabla \mathrm{T} \times \mathrm{B}) \times \mathrm{B} + \varepsilon_{\mathrm{p}} (\nabla \mathrm{E}) \cdot \hat{\mathrm{E}} + (\nabla \mathrm{B}) \cdot \left( \frac{\mathrm{B}}{\mu_{\mathrm{m}}} + \varepsilon_{\mathrm{p}} \mathrm{v} \times \hat{\mathrm{E}} \right) + \frac{\mathrm{D}}{\mathrm{D} t} (\varepsilon_{\mathrm{p}} (\hat{\mathrm{E}} \times \mathrm{B})), \tag{3.75}$$

$$\rho C_{p} \frac{DT}{Dt} = Q_{h} + \nabla \cdot (\kappa_{1} \nabla T + \kappa_{2} d \cdot \nabla T + \kappa_{4} \hat{E} + \kappa_{5} d \cdot \hat{E} + \kappa_{7} \nabla T \times B + \kappa_{8} \hat{E} \times B) + 
\sigma_{1} \hat{E} \cdot \hat{E} + \sigma_{4} \hat{E} \cdot \nabla T - \frac{\kappa_{2}}{T} \nabla T \cdot d \cdot \nabla T - \frac{\kappa_{5}}{T} \hat{E} \cdot d \cdot \nabla T + \frac{\kappa_{8}}{T} \hat{E} \cdot (\nabla T \times B) + 
\hat{E} \cdot \frac{D(\varepsilon_{p} \hat{E})}{Dt} - \frac{B}{\mu_{m}} \cdot \frac{DB}{Dt}.$$
(3.76)

In the above system, the equation of electric charge conservation is omitted because it can be readily obtained by combining the first and fourth of the Maxwell's equations. The viscous dissipation term and the unsteady pressure term on the right side of the energy conservation (Eq. (3.76)) have been neglected, as is usually done in incompressible viscous flow modeling.

# CHAPTER 4 RESEARCH METHODOLOGY

#### 4.1 Research Procedure

- 4.1.1 Study theory and literature review.
- 4.1.2 Generate mathematical modeling of combination between magnetic field, electric field, flow field, and temperature field.
- 4.1.3 Create computer programming for calculating air velocity profiles and temperature distributions through the fin under magnetic and electric fields by coupling between magnetohydrodynamic, electrohydrodynamics, and extended surface techniques.
- 4.1.4 Analyze the effect of all parameters to the heat transfer coefficient comprising; primary fluid velocity, geometry and dimension of the extended surface, intensity of magnetic field, magnetic pole arrangement, number of magnetic poles, supplied voltage at wire electrode, electrode arrangement, distance between wire electrodes, etc.
- 4.1.5 Experimental setup to verify the numerical results.
- 4.1.6 Bring the calculated results to design MHD-EHD finned heat exchanger.
- 4.1.7 Discussion and conclusion.
- 4.1.8 Submit the report.

## **4.2** Numerical Procedure

Because of the extreme complexity of the complete, non-linear, fully coupled electro-magneto-hydrodynamics model, it is practically difficult to contemplate development of a numerical simulation package for its integration. Thus, there is no previous literature dealing with the numerical simulation of a couple of electro-magneto-hydrodynamics application. Consequently, the complete general electro-magneto-hydrodynamics model should be simplified for particular circumstances. This simplification must be performed in a consistent manner starting from the general electro-magneto-hydrodynamics model. Elimination of certain terms could be justified by an order of magnitude analysis that is most efficiently accomplished by performing a complete non-

dimensionalization of the model. Thus all flow field, electric field, and magnetic field parameters and all physical properties will be non-dimensionalized which are not representing here due to the lengthy expressions.

This numerical modeling conducts grid generation method to convert the physical plane in Cartesian coordinates into the computational plane in curvilinear coordinates by Poisson's equation. In electric field, the first radial discrete value is computed using geometrical progression in such a way to allow high nodal density near the wire and the remaining region being subdivided into equispaced nodes. The starting conic coincides with a wire, for greater distance from the wire, the circular symmetry changes gradually fitting into Cartesian reference at a grounded surface and a symmetrical axis. At increasing distances from a wire, the mesh sizes increase as the computation marches into regions where sharp gradients are of lesser likelihood. The obtained charge and potential distributions are converted into polynomial function of quadrilaterals. This function must pass through the values of charge and potential distributions at the rectangular nodes and the results can be expressed by interpolation functions. Finally, these values are mapped into a non-uniform mesh sizes in Cartesian coordinate for calculating velocity and temperature.

Thus, the computer code is developed for calculating the coupled electro-magneto-hydrodynamics model. The discretization of non-linear equations is solved by a numerical method based on finite volume approximations. First, the system of Maxwell's equations is solved to calculate electric field, electric charge density, and magnetic flux density in a computational domain. The velocity at each time step is hence calculated in accordance with the obtained electric field, electric charge density, and magnetic flux density by SIMPLEC pressure-velocity coupling algorithm together with the QUICK third-order discretization scheme for the advection terms. Finally, the temperature field is finally acquired. The above mentioned procedures are repeated until the convergence criterion is reached. A convergence criterion is selected when the results are in steady state, periodic state, or non-periodic state.

# 4.3 Experimental Setup

To verify the value of current density, experiment setup is conducted. Fig. 1 shows an experimental system, the plate and fin heat sinks are made of aluminum with a thermal conductivity of 121 W/m·K. A channel has two horizontal opening at the top and bottom with respective dimensions of 5 cm in width, 40 cm in height, and 100 cm in depth. The experimental vertical channel is located between the super-conducting magnets. The experimental channel is heated by an electric wire with DC power supply for which electric current and voltage are measured with ammeter and voltmeter. The constant temperature bath is employed to keep the experimental apparatus at a fixed temperature. This experiment conducts on both natural and forced convections. A high voltage DC power supply is used to charge the electrode. The seven wire electrodes are made of carbon-steel with a diameter of 0.3 mm. They are installed at cross angle of a test section and charged with a positive DC high voltage. The heated wall and fins are grounded. The current density distribution is measured on a collecting electrode. To prevent the heat loss outside of the channel, fiberglass and bakelite insulations are used. The following measures are undertaken by varying the supplied voltage from 0 to 15 kV. The temperature inside the enclosure is measured by K-type thermocouples recorded in the PC-computer with a data acquisition system.

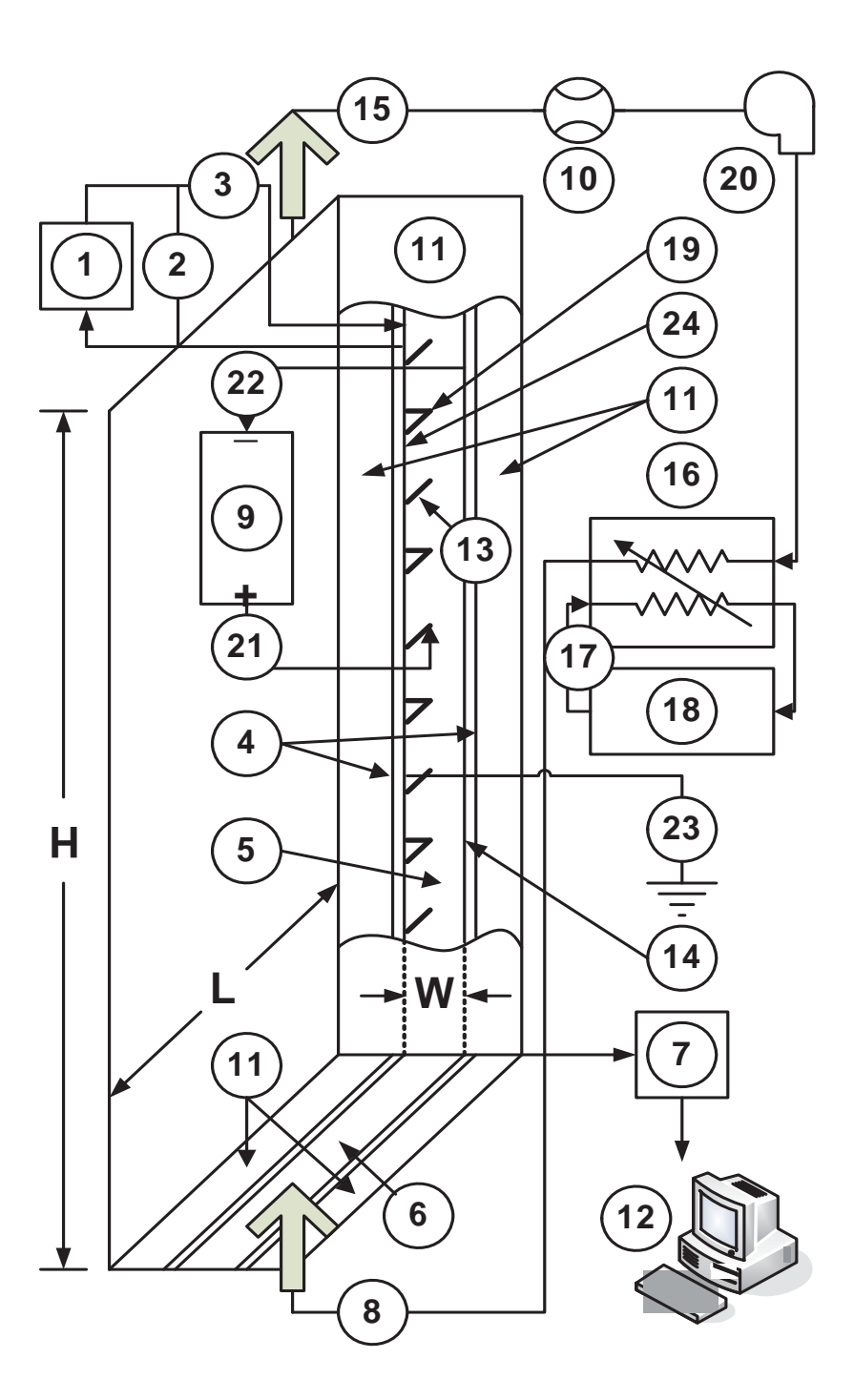


Fig. 4.1 Schematic sketch of the electro-magneto-hydrodynamics apparatus.

# CHAPTER 5 RESULTS AND DISCUSSION

### **5.1 Channel Configuration**

A schematic sketch of a finned channel and its boundary conditions required for the governing equations are illustrated in Fig. 5.1. Assuming that the fin is made from a very high conductive material, thus, the bottom wall and thin fins are maintained at a uniform temperature and the right wall is perfectly insulated. Both left and right sides of a channel are opened. The hot wall and thin fins are electrically grounded and the channel dimensions are 5 cm in height and 40 cm in length. The boundary conditions are expressed as

$$x = 0: \mathbf{v}_{x} = \mathbf{v}_{0}, T = T_{C}$$

$$x = L: P = 0, \frac{\partial \mathbf{v}_{x}}{\partial x} = 0, \frac{\partial \mathbf{v}_{y}}{\partial x} = 0, \frac{\partial^{2} T}{\partial x^{2}} = 0$$

$$y = 0: \mathbf{v}_{x} = 0, \mathbf{v}_{y} = 0, T = T_{H}, V = 0$$

$$y = H: \mathbf{v}_{x} = 0, \mathbf{v}_{y} = 0, \frac{\partial T}{\partial y} = 0, \frac{\partial V}{\partial y} = 0$$
and at the fin:  $\mathbf{v}_{x} = 0, \mathbf{v}_{y} = 0, T = T_{H}, V = 0$ 

The flow and temperature fields are shown in Figs. 5.2 – 5.7. For non-EHD, at low Reynolds number, the strength of primary vortex is weakened due to the fins obstruct the movement of fluid. This is because the convection not being strong compared with conduction and it has the most remarkable effects on the flow field when the fin length or number of fins is rather high. It appears that the stream lines become more packed with the increasing of Reynolds number, thus, the fluid moves faster as forced convection is intensified. On the other hand, conduction through the channel is enhanced with fin but natural convection is suppressed due to the presence of fin. Therefore, for a requirement of maximizing heat transfer, these two phenomena should be analyzed by applying at an appropriate condition. The numerical results of Nusselt number without EHD effect are validated against the bench mark correlation of the forced convection in a channel at the

dimensions of 5 cm in height, 40 cm in length, and Re is in the range of 100 to 2000. The calculated Nusselt numbers agree quite well within a maximum error of 3.16 % at Re = 2000. Moreover, a numerical code is compared with the experiments of EHD effect on the forced convection inside a channel, the controlling parameters are Re =10<sup>2</sup>,  $N_f$  = 6,  $N_e$  = 6, and  $L_f$  = 0.4 (Fig. 5.2). The comparison of average Nusselt number calculated from the numerical code to that obtained from the apparatus is expressed in Table 1, therefore, it is believed that the numerical solutions are really acceptable. All numerical calculations are carried out with the computational grids by grid independence test. A grid sensitivity analysis is conducted, for example, at  $V_0$  = 12.0 kV, Re =10<sup>2</sup>,  $N_f$  = 6,  $N_e$  = 6, and  $L_f$  = 0.4, where  $N_f$  is the number of fins,  $N_e$  is the number of electrodes, and  $L_f$  is the dimensionless fin length (per channel height).

In this study, three states of convergence criterion; study, periodic, and non-periodic are occurred. For  $(V_0 = 12.0 \text{ kV}, \text{Re} = 5 \times 10^2, N_f = 6, N_e = 6 \text{ } (x \text{ is between the fins, } y = 2.5 \text{ cm})$ , and  $L_f = 0.4$ ),  $(V_0 = 8.0 \text{ kV}, \text{Re} = 10^2, N_f = 6, N_e = 6 \text{ } (x \text{ is between the fins, } y = 2.5 \text{ cm})$ , and  $L_f = 0.4$ ),  $(V_0 = 12.0 \text{ kV}, \text{Re} = 10^2 - 5 \times 10^2, N_f = 6, N_e = 6 \text{ } (x \text{ is ahead the fins by } 1.25 \text{ cm}, y = 2.5 \text{ cm})$ , and  $L_f = 0.4$ ),  $(V_0 = 12.0 \text{ kV}, \text{Re} = 10^2, N_f = 6, N_e = 3, \text{ and } L_f = 0.4)$ ,  $(V_0 = 12.0 \text{ kV}, \text{Re} = 5 \times 10^2, N_f = 6, N_e = 11-15, \text{ and } L_f = 0.4)$ ,  $(V_0 = 12.0 \text{ kV}, \text{Re} = 10^3, N_f = 6, N_e = 22-26, \text{ and } L_f = 0.4)$ ,  $(V_0 = 12.0 \text{ kV}, \text{Re} = 10^2, N_f = 11-26, N_e = 6, \text{ and } L_f = 0.4)$ ,  $(V_0 = 12.0 \text{ kV}, \text{Re} = 5 \times 10^2, N_f = 22-26, N_e = 6, \text{ and } L_f = 0.4)$ , the flow field reaches to periodic state in which the maximum period reaches to an approximately of 170 dimensionless time steps. For  $(V_0 = 12.0 \text{ kV}, \text{Re} = 10^2, N_f = 6, N_e = 11-26, \text{ and } L_f = 0.4)$ ,  $(V_0 = 12.0 \text{ kV}, \text{Re} = 5 \times 10^2, N_f = 6, N_e = 18-26, \text{ and } L_f = 0.4)$ , the flow field reaches to non-periodic state. While the other cases reach to steady state.

Fig. 5.2 investigates the stream function contours and temperature distributions (isotherm lines) of the electrohydrodynamic applying in the finned channel while the Reynolds number is varied in the range of 100 - 2000 in which an effect of Joule heating at the wire electrode is neglected ( $V_0 = 12.0 \text{ kV}$ ,  $N_f = 6$ ,  $N_e = 6$ , and  $L_f = 0.4$ ). For applying EHD (electrodes are placed at y = 2.5 cm, y is between the fin), the flow patterns are oscillated due to the interaction between thermal buoyancy force and electrical body force. Moreover, two categories of flow pattern are observed in these figures; steady state (Figs. 5.2(a)-(b)) and periodic state (Figs. 5.2(c)-(d)). There is an effect of secondary flow induced by ionic wind at the wire electrode which causes two of rotating cellular motions occur at each electrode in Figs. 5.2(a)-(b). It can be observed that flow pattern in the

channel is activated by electric field at low Reynolds number. However, it is dominated by a convective regime instead of electric field as Reynolds number increases further to 1000 and 2000 in Figs. 5.2(c)-(d). The cold air is embarked through the left opening, moves along the hot wall and fins, and discharges at the right opening. Consider temperature field at low Reynolds number, the temperature field is affected due to the electric field. A boundary layer heat transfer corresponding to the second convection cells along the channel which enhanced convection and boundary layer flow and heat transfer at a hot wall. The thermal boundary layer at a hot wall is perturbed by the electric field when it extends over the recirculatory region. It can be seen that temperature gradient (line density) at a hot wall becomes higher with the increasing of Reynolds number, that cause high heat transfer coefficient develops along a hot wall. However, flow patterns and temperature distributions remain almost resemble to those of non-electrohydrodynamic phenomenon at a high Reynolds number. The above discussion indicates that the electric field cannot initially distort the entering velocity profile. Fig. 5.3 shows the effect of electrode distance on the flow and temperature fields ( $V_0 = 12.0 \text{ kV}$ , Re = 100,  $N_f = 6$ ,  $N_e = 6$ , and  $L_f = 0.4$ : (a) y = 2.0, (b) y = 1.5, (c) y = 1.0, and (d) y = 0.5). The large vortices cause the heat trap occurring along the channel at a high intensity of electric field strength when electrodes are shifting near the hot wall.

Fig. 5.4 conducts the flow and temperature fields of four different electrode positions; (x is ahead the fins by = 1.25 cm, y = 2.5 cm), (x is on the fin strip, y = 2.5 cm), (x is behind the fins by = 1.25 cm, y = 2.5 cm), and (x is on the fin strip, y = 3.5 cm), while the numbers of fins and electrodes are also kept at six ( $V_0$  = 12.0 kV, Re = 100,  $N_f$  = 6,  $N_e$  = 6, and  $L_f$  = 0.4). It can be observed that the second arrangement (Fig. 5.4(b)) performs a maximum convection from a highest average velocity along a hot wall compared with other arrangement due to the circulation around the fins is relatively stronger and more complete, as a result of which the flow around the fins is with a vortex formed on the fins, while the first arrangement (Fig. 5.4(a)) yields the pair of vortices which reduces the flow structure. The oscillatory stream function and isotherm line contours for various numbers of electrodes as 1, 3, 11, and 26 are expressed in Fig. 5.5 ( $V_0$  = 12.0 kV, Re = 100,  $N_f$  = 6, and  $L_f$  = 0.4). Effect of the number of electrodes plays much important role on the flow pattern of air inside a channel. It can be observed that the number of vortices increases when the number of electrodes reaches a sufficient value in Fig. 5.5(d) which the large

vortices occur especially around the extremes of an electrode strip. The isotherm lines show a formation of the boundary layer heat transfer along a hot wall. As seen that temperature gradient at a hot wall of Fig. 5.5(c) has a highest value, it means that this categories also achieves a maximum heat transfer coefficient. Therefore, it can be concluded that the number of electrodes has more significant at an optimum value. However, it should be compared between the extra received heat transfer and power of electrical energy input for an optimized design.

A non-equivalent number of fins dominates the different flow patterns to occur in the channels of Fig. 5.6 ( $V_0 = 12.0 \text{ kV}$ , Re = 100,  $N_e = 6$ , and  $L_f = 0.4$ : (a)  $N_f = 1$ , (b)  $N_f = 3$ , (c)  $N_f = 11$ , and (d)  $N_f = 26$ ). Temperature contours along the channel of Fig. 5.6(a) is quite similarly with the case of no fin attached from the less remarkable effect by a single fin. The separation points over the fins and the heat trap between the fins are enhanced accordingly with the number of fins. In Fig. 5.7 ( $V_0 = 12.0 \text{ kV}$ , Re = 100,  $N_f = 6$ , and  $N_e = 6$ : (a)  $L_f = 0.1$ , (b)  $L_f = 0.2$ , (c)  $L_f = 0.6$ , and (d)  $L_f = 0.8$ ), a character of the clockwise and counter-clockwise rotating vortices is unaltered, with longer fins bringing about more change to the flow compared with shorter fins. For shorter fins, almost all positions only change the temperature distribution locally and the rest of a hot wall remains unaffected. This is because the primary flow cannot alter too much upon introduction of a short length and the fins only change the velocity distribution locally. It is noticed that for  $L_f > 0.5$  (Fig. 5.7(c) and (d)), recirculating vortices between the fins has more remarkable effects on the flow field.

The average Nusselt number over a period of periodic state or over an entire time span of non-periodic state along the channels for various Reynolds numbers is shown in Fig. 5.8 ( $N_f = 6$ ,  $N_e = 6$ , and  $L_f = 0.4$ ). For non-EHD, placing fins on a hot wall always reduces the heat transfer. The average Nusselt number become smaller with an increasing of the fin length due to the fins obstruct flow and also reduce convective strength. However, the effect of fins becomes less remarkable with a rising of the Reynolds number because a primary flow is enhanced with compensate the blocking effect by the fins. Thus, for high Reynolds number, the flow field is augmented regardless of the length and position of fins. Indeed, EHD augmented flow and heat transfer yield more significant role at a low Reynolds number region and this phenomenon is consequently influenced at a high supplied voltage. The maximum normalized average Nusselt number with  $V_0 = 12.0$  kV and Re = 100 is 8.32. Fig. 5.9 demonstrates the heat transfer enhancement in term of

Nu/Nu<sub>0</sub> with the values of Reynolds number and electrode distance to the hot wall. The enhanced ratio is increased with a small channel height due to the high electric field strength. In Fig. 5.10 ( $V_0 = 12.0 \text{ kV}$ ,  $N_f = 6$ ,  $N_e = 6$ , and  $L_f = 0.4$ ), the electrode arrangement in Fig. 5.4(b) becomes a most remarkable effect with a rising of the convective heat transfer rate due to the fact that it has a minimum thermal boundary layer thickness along a channel.

The enhanced heat transfer coefficient inside the channels has been investigated in Fig. 5.11 as a function of number of electrodes with Raynolds number as a parameter at  $V_0$ = 12.0 kV,  $N_f$  = 6, and  $L_f$  = 0.4. It can be indicated that the enhanced fluid velocity increases with the number of electrodes due to the influence of momentum transfer from the free charges. Augmented Nusselt number reaches a first maximum at an intermediate number of electrodes, reduces slowly, and increases again due to the high intensity of the electric field at higher number of electrodes. This characteristic can be analyzed by considering the isotherm line density at the lower wall of Fig. 5.5. For the case  $N_e = 11$ , the density is found to be higher than other cases due to lower number of vortices and also the smaller heat trap that yields the greatest heat transfer coefficient. Surprisingly, the higher number of electrodes at  $N_e = 26$  can not perform the proportional value of the heat transfer coefficient from which comparable different from that of no fin attached because the optimum number in this study must be depended on the fin geometry. Fig. 5.12 conducts relation between the heat transfer and number of fins at the same fin length ( $N_e = 6$  and  $L_f$ = 0.4). The Nusselt number decreases monotonously with the number of fins due to a low convective heat transfer that occurred at a high number of fins. The effect of fin length on the electrohydrodynamic enhanced heat transfer is conducted in Fig. 5.13 ( $N_f = 6$  and  $N_e =$ 6). Average Nusselt number is also a decreasing function of the fin length because it is dominated by the conduction at a long fin length but which is considerably improved by the electric field when explaining in term of the ratio between EHD per non-EHD.

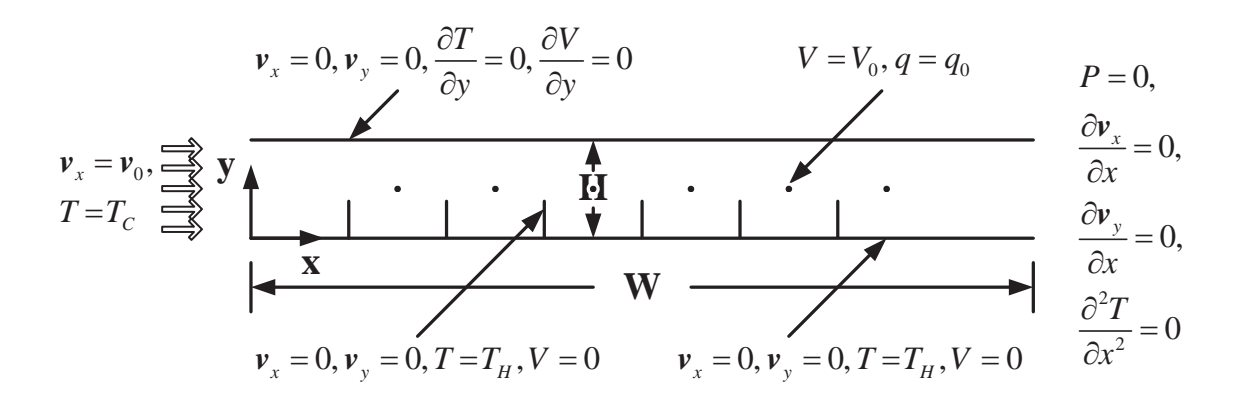


Fig. 5.1 Schematic sketch of the finned channel.

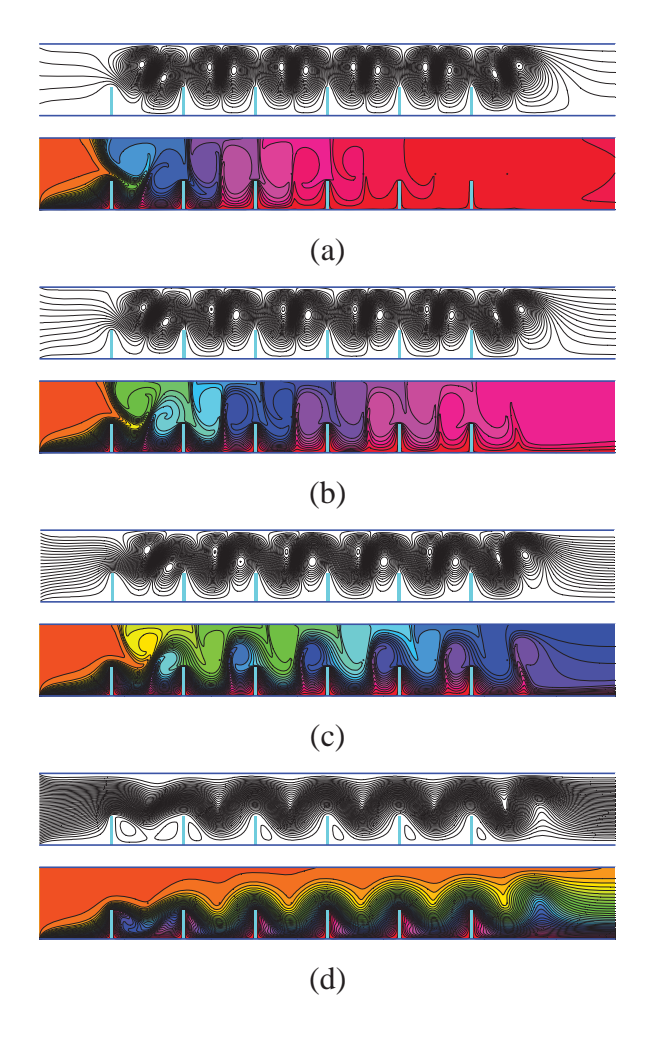


Fig. 5.2 Stream function and isotherm line contours inside the channels for various Reynolds numbers ( $V_0 = 12 \text{ kV}$ ,  $N_f = 6$ ,  $N_e = 6$ , and  $L_f = 0.4$ ): (a) Re =  $10^2$ , (b) Re =  $5 \times 10^2$ , (c) Re =  $10^3$ , and (d) Re =  $2 \times 10^3$ .

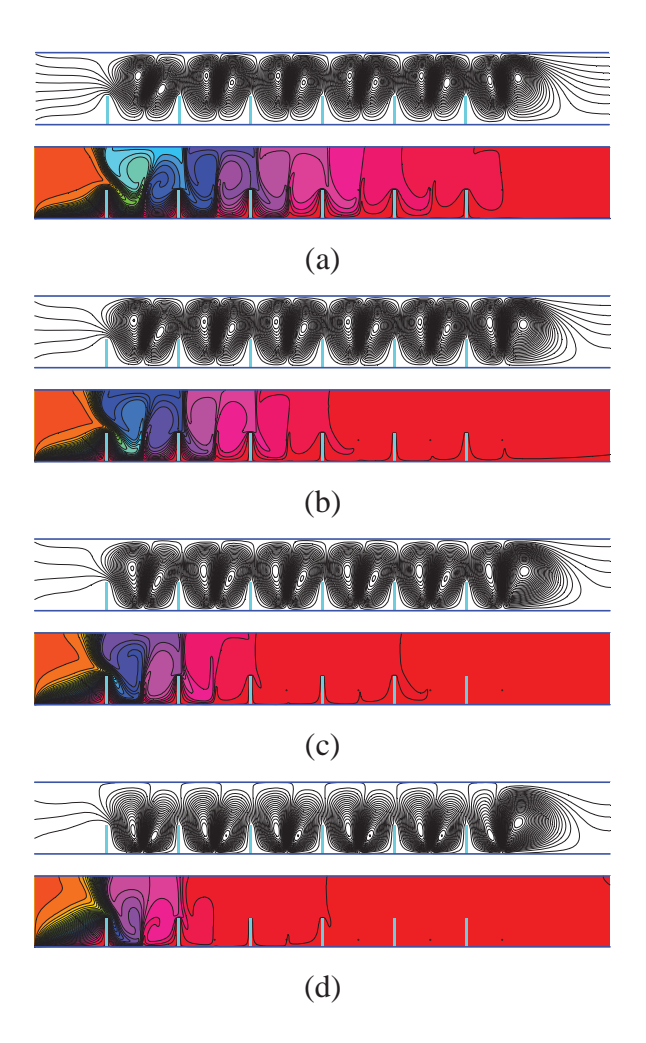


Fig. 5.3 Stream function and isotherm line contours inside the channels for various electrode distance ( $V_0 = 12.0 \text{ kV}$ , Re =  $10^2$ ,  $N_f = 6$ ,  $N_e = 6$ , and  $L_f = 0.4$ ): (a) y = 2.0 cm, (b) y = 1.5 cm, (c) y = 1.0 cm, and (d) y = 0.5 cm.

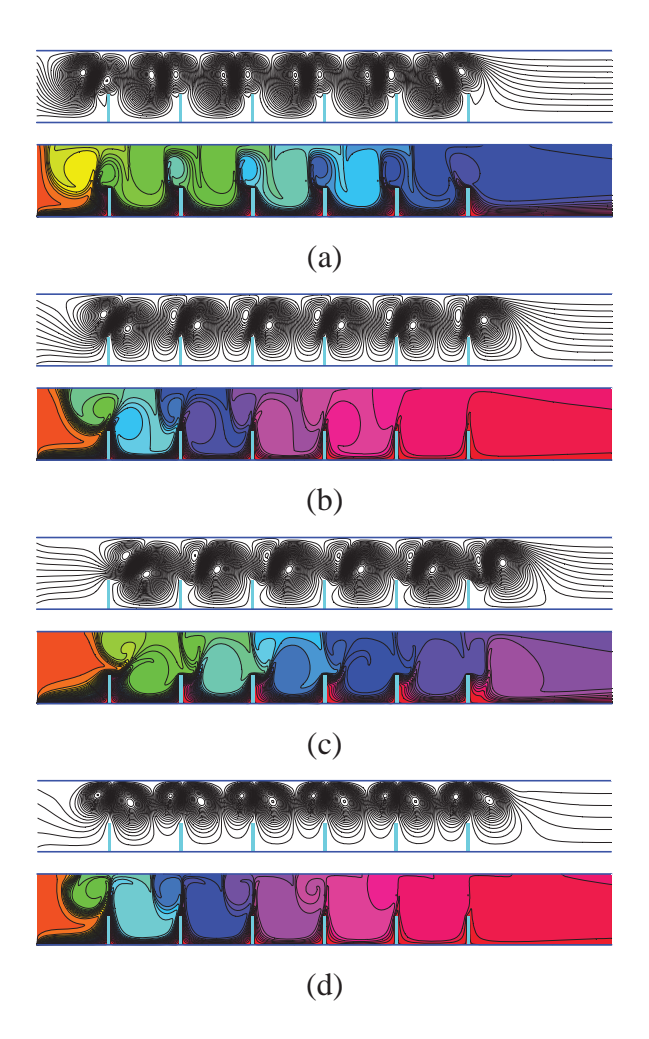


Fig. 5.4 Effect of the electrode arrangement on the flow and temperature fields ( $V_0 = 12.0$  kV, Re =  $10^2$ ,  $N_f = 6$ ,  $N_e = 6$ , and  $L_f = 0.4$ ): (a) x is ahead the fins by 1.25 cm, y = 2.5 cm, (b) x is on the fin strip, y = 2.5 cm, (c) x is behide the fins by 1.25 cm, y = 2.5 cm, and (d) x is on the fin strip, y = 3.5 cm.

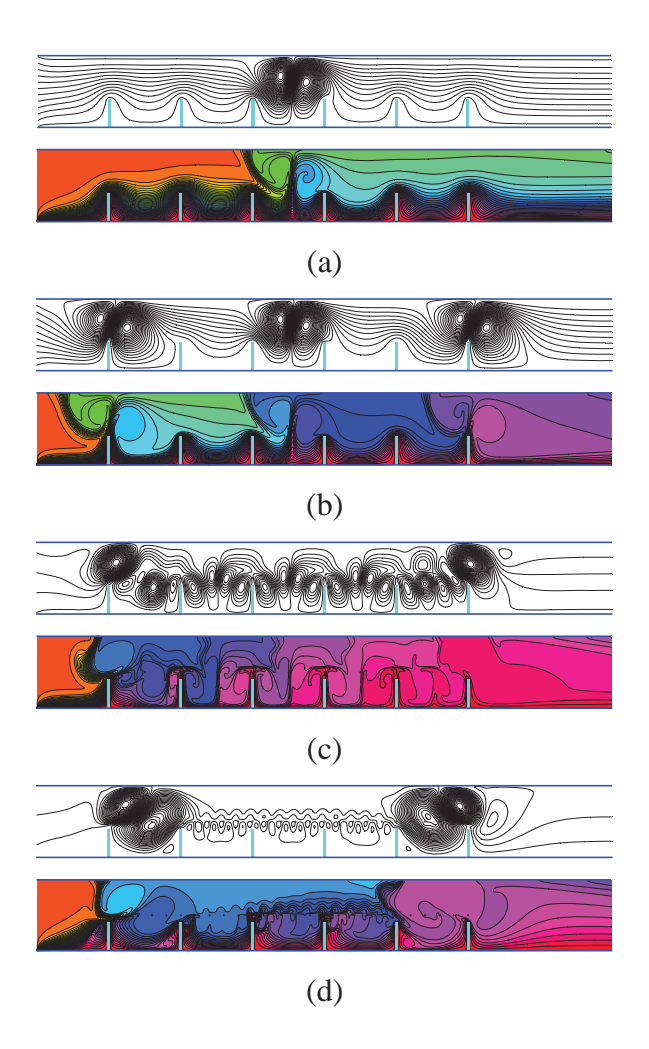


Fig. 5.5 Number of electrodes effect on the flow and temperature fields inside the finned channels ( $V_0 = 12.0 \text{ kV}$ , Re =  $10^2$ ,  $N_f = 6$ , and  $L_f = 0.4$ ): (a)  $N_e = 1$ , (b)  $N_e = 3$ , (c)  $N_e = 11$ , and (d)  $N_e = 26$ .

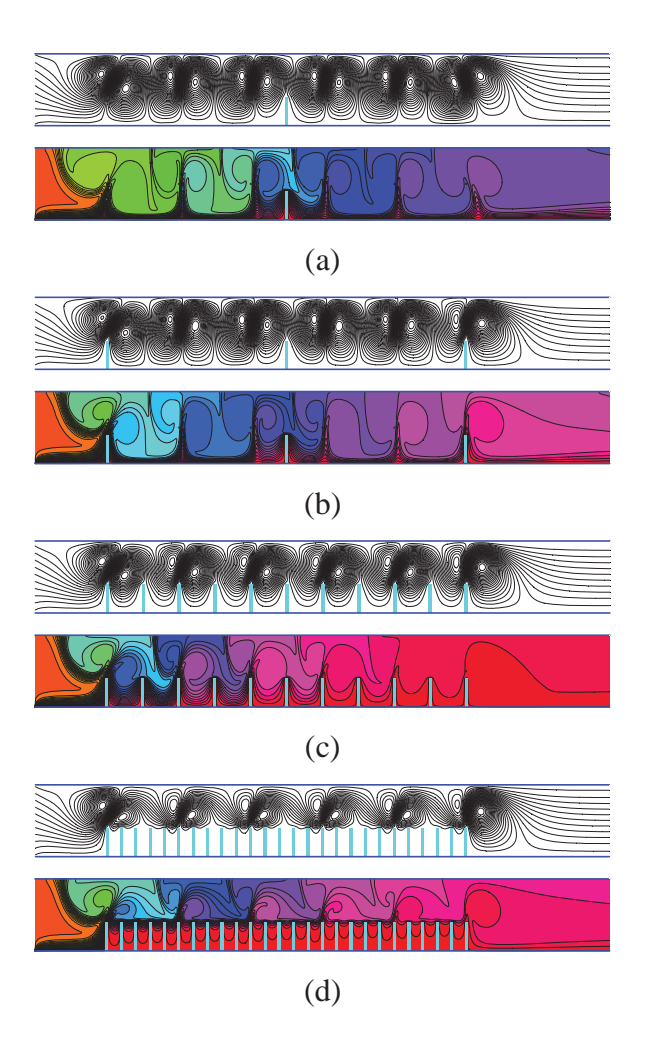


Fig. 5.6 Number of fins effect on the flow and temperature fields inside the finned channels ( $V_0 = 12.0 \text{ kV}$ , Re =  $10^2$ ,  $N_e = 6$ , and  $L_f = 0.4$ ): (a)  $N_f = 1$ , (b)  $N_f = 3$ , (c)  $N_f = 11$ , and (d)  $N_f = 26$ .

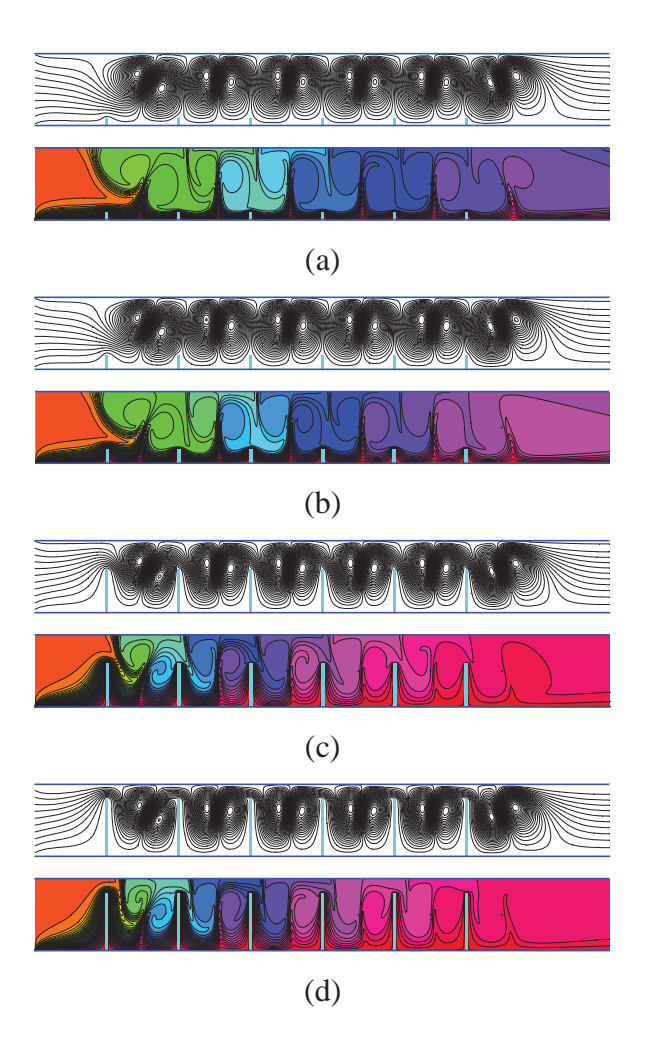


Fig. 5.7 Stream function and isotherm line contours inside the finned channels for various fin lengths ( $V_0 = 12.0 \text{ kV}$ , Re =  $10^2$ ,  $N_f = 6$ , and  $N_e = 6$ ): (a)  $L_f = 0.1$ , (b)  $L_f = 0.2$ , (c)  $L_f = 0.6$ , and (d)  $L_f = 0.8$ .

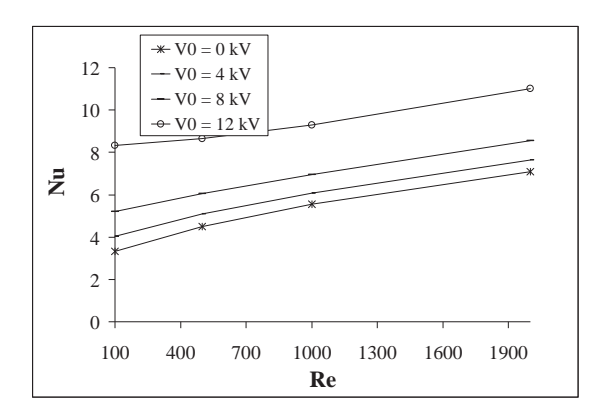


Fig. 5.8 Nusselt number as a function of the Reynolds number ( $N_f = 6$ ,  $N_e = 6$ , and  $L_f = 0.4$ ).

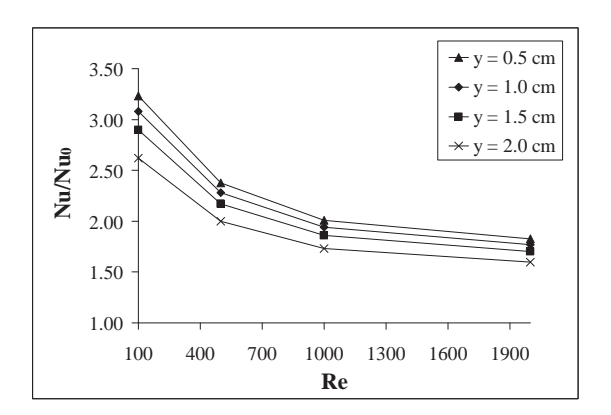


Fig. 5.9 Effect of the electrode distance on the heat transfer ( $V_0 = 12.0 \text{ kV}$ ,  $N_f = 6$ ,  $N_e = 6$ , and  $L_f = 0.4$ ).

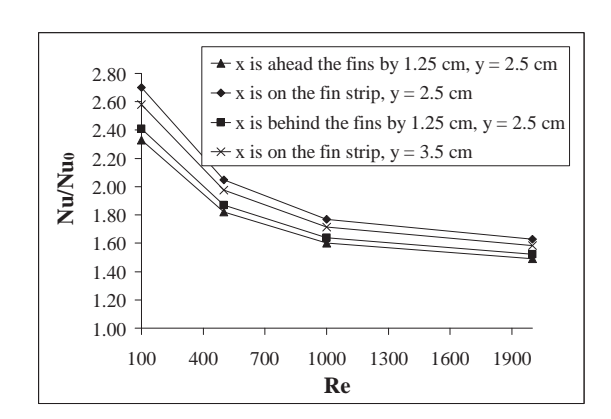


Fig. 5.10 Effect of the electrode arrangement on the heat transfer ( $V_0 = 12.0 \text{ kV}$ ,  $N_f = 6$ ,  $N_e = 6$ , and  $L_f = 0.4$ ).

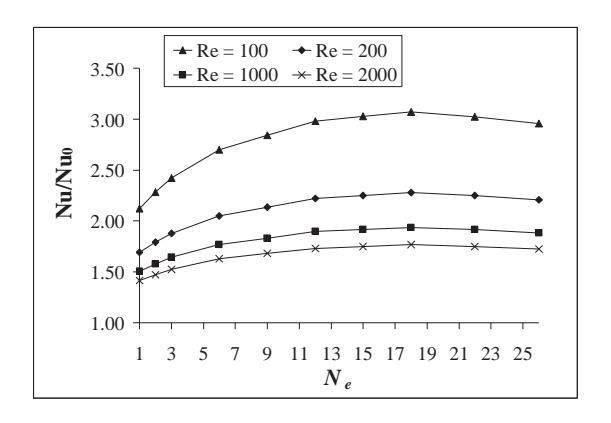


Fig. 5.11 Nusselt number for various number of electrodes ( $V_0 = 12.0 \text{ kV}$ ,  $N_f = 6$ , and  $L_f = 0.4$ ).

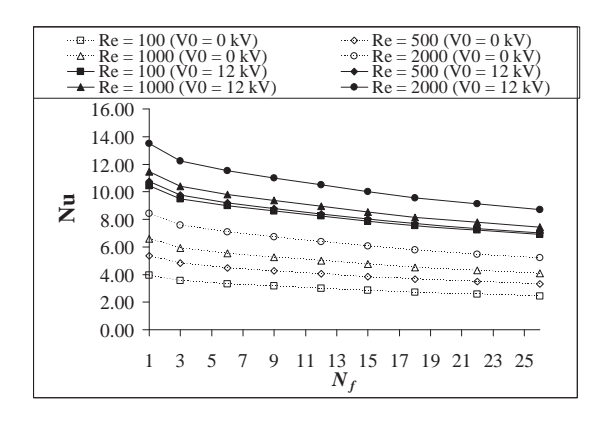


Fig. 5.12 Number of fins effect on the Nusselt number ( $N_e = 6$ , and  $L_f = 0.4$ ).

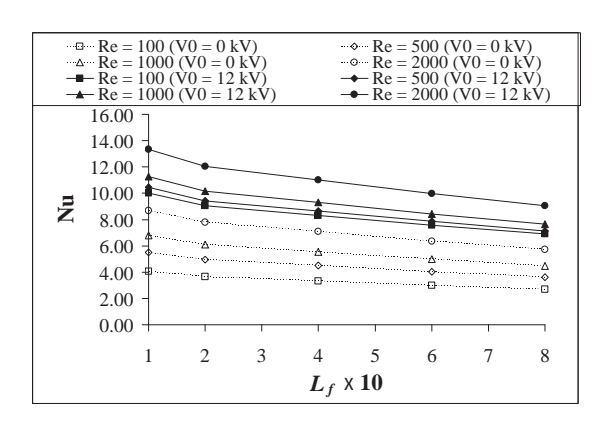


Fig. 5.13 Nusselt number at each fin length ( $N_f = 6$  and  $N_e = 6$ ).

Another schematic sketch of a finned channel and its boundary conditions required for the governing equations are illustrated in Fig. 5.14. Assuming that the fin is made from a very high conductive material, thus, the bottom wall and thin fins are maintained at a uniform temperature and the right wall is perfectly insulated. Both left and right sides of a channel are opened. The hot wall and thin fins are electrically grounded and the channel dimensions are 5 cm in height and 40 cm in length. The boundary conditions are expressed as

$$x = 0: \mathbf{v}_{x} = \mathbf{v}_{0}, T = T_{C}$$

$$x = L: P = 0, \frac{\partial \mathbf{v}_{x}}{\partial x} = 0, \frac{\partial \mathbf{v}_{y}}{\partial x} = 0, \frac{\partial^{2} T}{\partial x^{2}} = 0$$

$$y = 0: \mathbf{v}_{x} = 0, \mathbf{v}_{y} = 0, T = T_{H}, V = 0$$

$$y = H: \mathbf{v}_{x} = 0, \mathbf{v}_{y} = 0, \frac{\partial T}{\partial y} = 0, \frac{\partial V}{\partial y} = 0$$
and at the fin:  $\mathbf{v}_{x} = 0, \mathbf{v}_{y} = 0, T = T_{H}, V = 0$ 

The flow and temperature fields are shown in Figs. 5.15 - 5.20. For non-EHD, at low Reynolds number, the strength of primary vortex is weakened due to the fins obstruct the movement of fluid. This is because the convection not being strong compared with conduction and it has the most remarkable effects on the flow field when the fin length or number of fins is rather high. It appears that the stream lines become more packed with the increasing of Reynolds number, thus, the fluid moves faster as forced convection is intensified. On the other hand, conduction through the channel is enhanced with fin but natural convection is suppressed due to the presence of fin. Therefore, for a requirement of maximizing heat transfer, these two phenomena should be analyzed by applying at an appropriate condition. The numerical results of Nusselt number without EHD effect are validated against the bench mark correlation of the forced convection in a channel at the dimensions of 5 cm in height, 40 cm in length, and Re is in the range of 100 to 2000. The calculated Nusselt numbers agree quite well within a maximum error of 3.16 % at Re = 2000. Moreover, a numerical code is compared with the experiments of EHD effect on the forced convection inside a channel, the controlling parameters are Re =  $10^2$ ,  $N_f = 6$ ,  $N_e = 6$ ,  $L_{fu} = 0.4$ , and  $L_{fl} = 0.4$  (Fig. 5.15). The comparison of average Nusselt number calculated

from the numerical code to that obtained from the apparatus is expressed in Table 1, therefore, it is believed that the numerical solutions are really acceptable. All numerical calculations are carried out with the computational grids by grid independence test. A grid sensitivity analysis is conducted, for example, at  $V_0 = 12.0 \text{ kV}$ , Re  $= 10^2$ ,  $N_f = 6$ ,  $N_e = 6$ ,  $L_{fu} = 0.4$ , and  $L_{fl} = 0.4$ , where  $N_f$  is the number of fins,  $N_e$  is the number of electrodes, and  $L_f$  is the dimensionless fin length (per channel height). In Table 2, a grid size of  $1101 \times 211$  is selected for calculating the velocity and temperature fields in this configuration. Since the number of electrodes or number of fins becomes large (in the horizontal direction), the grid independence test is done by fixing n (number of nodes in vertical the direction) and varying n (number of nodes in the horizontal direction). Nevertheless, it must be fixing n and varying n when the fin length becomes large. A detail of grid sizes used in this study is expressed in Table 3.

In this study, three states of convergence criterion; study, periodic, and non-periodic are occurred. For  $(V_0 = 12.0 \text{ kV}, \text{Re} = 10^2 - 10^3, N_f = 6, N_e = 6 \text{ (x is between the fins, y = }$ 1.5 cm),  $L_{fu} = 0.4$ , and  $L_{fl} = 0.4$ ),  $(V_0 = 8.0 \text{ kV}, \text{Re} = 10^2, N_f = 6, N_e = 6 \text{ (x is between the } 1.5 \text{ cm}))$ fins, y = 1.5 cm),  $L_{fu} = 0.4$ , and  $L_{fl} = 0.4$ ),  $(V_0 = 12.0 \text{ kV}, \text{Re} = 10^2, N_f = 6, N_e = 6 \text{ (x is on } 1.5 \text{ cm}))$ the lower fin strip, y = 2.5 cm),  $L_{fu} = 0.4$ , and  $L_{fl} = 0.4$ ),  $(V_0 = 12.0 \text{ kV}, \text{Re} = 10^2, N_f = 6, N_e)$ = 6 (x is behide the lower fins by 1.25 cm, y = 2.5 cm),  $L_{fu} = 0.4$ , and  $L_{fl} = 0.4$ ), ( $V_0 = 12.0$ kV, Re =  $10^2$ ,  $N_f = 6$ ,  $N_e = 6$  (x is behide the lower fins by 1.25 cm, y = 1.5 cm),  $L_{fu} = 0.4$ , and  $L_{fl} = 0.4$ ),  $(V_0 = 12.0 \text{ kV}, \text{Re} = 10^2, N_f = 6, N_e = 6 \text{ (x is behide the lower fins by 3.75)}$ cm, y = 1.5 cm),  $L_{fu} = 0.4$ , and  $L_{fl} = 0.4$ ),  $(V_0 = 12.0 \text{ kV}, \text{Re} = 5 \times 10^2, N_f = 6, N_e = 6 \text{ (x is } 10^2)$ on the lower fin strip, y = 2.5 cm),  $L_{fu} = 0.4$ , and  $L_{fl} = 0.4$ ),  $(V_0 = 12.0 \text{ kV}, \text{Re} = 10^2, N_f = 6,$  $N_e = 3$  and 11,  $L_{fu} = 0.4$ , and  $L_{fl} = 0.4$ ), ( $V_0 = 12.0$  kV, Re =  $5 \times 10^2$ ,  $N_f = 6$ ,  $N_e = 11$ ,  $L_{fu} = 10.4$ 0.4, and  $L_{fl} = 0.4$ ),  $(V_0 = 12.0 \text{ kV}, \text{Re} = 10^3, N_f = 6, N_e = 26, L_{fu} = 0.4, \text{ and } L_{fl} = 0.4)$ ,  $(V_0 = 12.0 \text{ kV}, \text{Re} = 10^3, N_f = 6, N_e = 26, L_{fu} = 0.4, \text{ and } L_{fl} = 0.4)$ 12.0 kV, Re =  $10^2$ ,  $N_f = 1$ , 11, and 26,  $N_e = 6$ ,  $L_{fu} = 0.4$ , and  $L_{fl} = 0.4$ ), ( $V_0 = 12.0$  kV, Re =  $5 \times 10^2$ ,  $N_f = 26$ ,  $N_e = 6$ ,  $L_{fu} = 0.4$ , and  $L_{fl} = 0.4$ ), the flow field reaches to periodic state in which the maximum period reaches to an approximately of 170 dimensionless time steps. For  $(V_0 = 12.0 \text{ kV}, \text{Re} = 10^2 - 5 \times 10^2, N_f = 6, N_e = 26, L_{fu} = 0.4, \text{ and } L_{fl} = 0.4)$ , the flow field reaches to non-periodic state. While the other cases reach to steady state.

Fig. 5.15 investigates the stream function contours and temperature distributions (isotherm lines) of the electrohydrodynamic applying in the finned channel while the Reynolds number is varied in the range of 100 - 2000 in which an effect of Joule heating at the wire electrode is neglected ( $V_0 = 12.0 \text{ kV}$ ,  $N_f = 6$ ,  $N_e = 6$ ,  $L_{fu} = 0.4$  and  $L_{fl} = 0.4$ ). For

applying EHD (electrodes are placed at y = 2.5 cm, y is between the fin), the flow patterns are oscillated due to the interaction between thermal buoyancy force and electrical body force. Moreover, two categories of flow pattern are observed in these figures; steady state (Figs. 5.15(a)-(b)) and periodic state (Figs. 5.15(c)-(d)). There is an effect of secondary flow induced by ionic wind at the wire electrode which causes two of rotating cellular motions occur at each electrode in Figs. 5.15(a)-(b). It can be observed that flow pattern in the channel is activated by electric field at low Reynolds number. However, it is dominated by a convective regime instead of electric field as Reynolds number increases further to 1000 and 2000 in Figs. 5.15(c)-(d). The cold air is embarked through the left opening, moves along the hot wall and fins, and discharges at the right opening. Consider temperature field at low Reynolds number, the temperature field is affected due to the electric field. A boundary layer heat transfer corresponding to the second convection cells along the channel which enhanced convection and boundary layer flow and heat transfer at a hot wall. The thermal boundary layer at a hot wall is perturbed by the electric field when it extends over the recirculatory region. It can be seen that temperature gradient (line density) at a hot wall becomes higher with the increasing of Reynolds number, that cause high heat transfer coefficient develops along a hot wall. However, flow patterns and temperature distributions remain almost resemble to those of non-electrohydrodynamic phenomenon at a high Reynolds number. The above discussion indicates that the electric field cannot initially distort the entering velocity profile. Fig. 5.16 conducts the flow and temperature fields of four different electrode positions; (x is on the fin strip, y = 2.5 cm), (x is behide the fins by = 1.25 cm, y = 2.5 cm), (x is behind the fins by = 1.25 cm, y = 1.5cm), and (x is behind the fins by = 3.75 cm, y = 1.5 cm), while the numbers of fins at each side and electrodes (at y = 1.5 cm) are also kept at six ( $V_0 = 12.0$  kV, Re = 100,  $N_{fu} = 6$ ,  $N_{fl}$ = 6,  $N_e$  = 6,  $L_{fu}$  = 0.4 and  $L_{fl}$  = 0.4). It can be observed that the third arrangement (Fig. 5.16(c)) performs a maximum convection from a highest average velocity along a hot wall compared with other arrangement due to the circulation around the fins is relatively stronger and more complete, as a result of which the flow around the fins is with a vortex formed on the fins, while the first arrangement (Fig. 5.16(a)) yields the pair of vortices which reduces the flow structure.

In Fig. 5.17 ( $V_0 = 12.0 \text{ kV}$ , Re = 100,  $N_{fu} = 6$ ,  $N_{fl} = 6$ , and  $N_e = 6$ : (a)  $L_{fu} = 0.1$ , (b)  $L_{fu} = 0.2$ , (c)  $L_{fu} = 0.6$ , and (d)  $L_{fu} = 0.8$ ), a character of the clockwise and counter-clockwise rotating vortices is unaltered, with longer fins bringing about more change to the flow

compared with shorter fins. For shorter fins, almost all positions only change the temperature distribution locally and the rest of a hot wall remains unaffected. This is because the primary flow cannot alter too much upon introduction of a short length and the fins only change the velocity distribution locally. It is noticed that for  $L_f > 0.5$  (Fig. 5.17(c) and (d)), recirculating vortices between the lower fins has more remarkable effects on the flow field. The oscillatory stream function and isotherm line contours for various numbers of electrodes as 1, 3, 11, and 26 are expressed in Fig. 5.18 ( $V_0 = 12.0 \text{ kV}$ , Re = 100,  $N_{fu} =$ 6,  $N_{fl} = 6$ ,  $L_{fu} = 0.4$  and  $L_{fl} = 0.4$ ). Effect of the number of electrodes plays much important role on the flow pattern of air inside a channel. It can be observed that the number of vortices increases when the number of electrodes is augmenting from 1 to 11, but the vortices are combining when the number of electrodes reaches a sufficient value in Fig. 5.18(d) which the large vortices occur along the channel length. The isotherm lines show a formation of the boundary layer heat transfer along a hot wall. As seen that temperature gradient at a hot wall of Fig. 5.18(c) has a highest value, it means that this categories also achieves a maximum heat transfer coefficient. Therefore, it can be concluded that the number of electrodes has more significant at an optimum value. However, it should be compared between the extra received heat transfer and power of electrical energy input for an optimized design.

A non-equivalent number of fins dominates the different flow patterns to occur in the channels of Fig. 5.19 (( $V_0 = 12.0 \text{ kV}$ , Re = 100,  $N_e = 6$ ,  $L_{fu} = 0.4$  and  $L_{fl} = 0.4$ ): (a)  $N_{fu}$  and  $N_{fl} = 1$ , (b)  $N_{fu}$  and  $N_{fl} = 3$ , (c)  $N_{fu}$  and  $N_{fl} = 11$ , and (d)  $N_{fu}$  and  $N_{fl} = 26$ ). Temperature contours along the channel of Fig. 5.19(a) is quite similarly with the case of no fin attached from the less remarkable effect by a single fin. The separation points over the fins and the heat trap between the fins are enhanced accordingly with the number of fins. Fig. 5.20 ( $V_0 = 12.0 \text{ kV}$ , Re = 100,  $N_{fu} = 6$ ,  $N_{fl} = 6$ , and  $N_e = 6$ : (a)  $L_{fu}$  and  $L_{fl} = 0.1$ , (b)  $L_{fu}$  and  $L_{fl} = 0.2$ , (c)  $L_{fu}$  and  $L_{fl} = 0.6$ , and (d)  $L_{fu}$  and  $L_{fl} = 0.8$ ) conducts some differential flow patterns compared with the previous results. A pair of vortices appears between the fins (that have one electrode) when the fin length becomes larger.

The average Nusselt number over a period of periodic state or over an entire time span of non-periodic state along the channels for various Reynolds numbers is shown in Fig. 5.21 ( $N_{fu} = 6$ ,  $N_{fl} = 6$ ,  $N_e = 6$ ,  $L_{fu} = 0.4$  and  $L_{fl} = 0.4$ ). For non-EHD, placing fins on a hot wall always reduces the heat transfer. The average Nusselt number become smaller with an increasing of the fin length due to the fins obstruct flow and also reduce convective

strength. However, the effect of fins becomes less remarkable with a rising of the Reynolds number because a primary flow is enhanced with compensate the blocking effect by the fins. Thus, for high Reynolds number, the flow field is augmented regardless of the length and position of fins. Indeed, EHD augmented flow and heat transfer yield more significant role at a low Reynolds number region and this phenomenon is consequently influenced at a high supplied voltage. The maximum normalized average Nusselt number with  $V_0 = 12.0$ kV and Re = 100 is 8.98. Fig. 5.22 shows a comparison of the electrode arrangements effected to the augmented average heat transfer for fin array attached from Fig. 5.16 ( $V_0 =$ 12.0 kV, Re = 100,  $N_{fu}$  = 6,  $N_{fl}$  = 6,  $N_e$  = 6,  $L_{fu}$  = 0.4 and  $L_{fl}$  = 0.4). It is found that when x is behind the fins by = 1.25 cm and y = 1.5 cm, this arrangement performs highest performance because it can enhance the velocity near the fin toward the hot wall of channel. In Fig. 5.23 ( $N_{fu} = 6$ ,  $N_{fl} = 6$ ,  $N_e = 6$ , and  $L_{fl} = 0.4$ ). Generally, average Nusselt number is also a decreasing function of the fin length because it is dominated by the conduction at a long fin length but which is considerably improved by the electric field when explaining in term of the ratio between EHD per non-EHD. However, it is interesting to noted that the maximum heat transfer in this case is happen when  $L_{fu} = 0.2$  from the optimum ratio between passive and active techniques.

The enhanced heat transfer coefficient inside the channels has been investigated in Fig. 5.24 as a function of number of electrodes with Raynolds number as a parameter at  $V_0$ = 12.0 kV,  $N_{fu}$  = 6,  $N_{fl}$  = 6,  $L_{fu}$  = 0.4 and  $L_{fl}$  = 0.4. It can be indicated that the enhanced fluid velocity increases with the number of electrodes due to the influence of momentum transfer from the free charges. Augmented Nusselt number reaches a first maximum at an intermediate number of electrodes, reduces slowly, and increases again due to the high intensity of the electric field at higher number of electrodes. This characteristic can be analyzed by considering the isotherm line density at the lower wall of Fig. 5.18. For the case  $N_e = 11$ , the density is found to be higher than other cases due to lower number of vortices and also the smaller heat trap that yields the greatest heat transfer coefficient. Surprisingly, the higher number of electrodes at  $N_e = 26$  can not perform the proportional value of the heat transfer coefficient from which comparable different from that of no fin attached because the optimum number in this study must be depended on the fin geometry. Fig. 5.25 conducts relation between the heat transfer and number of fins at the same fin length ( $N_e = 6$ ,  $L_{fu} = 0.4$  and  $L_{fl} = 0.4$ ). The Nusselt number decreases monotonously with the number of fins due to a low convective heat transfer that occurred at a high number of fins. The effect of fin length on the electrohydrodynamic enhanced heat transfer is conducted in Fig. 5.26 ( $N_{fu} = 6$ ,  $N_{fl} = 6$  and  $N_e = 6$ ). Average Nusselt number is also a decreasing function of the fin length because it is dominated by the conduction at a long fin length but which is considerably improved by the electric field when explaining in term of the ratio between EHD per non-EHD.

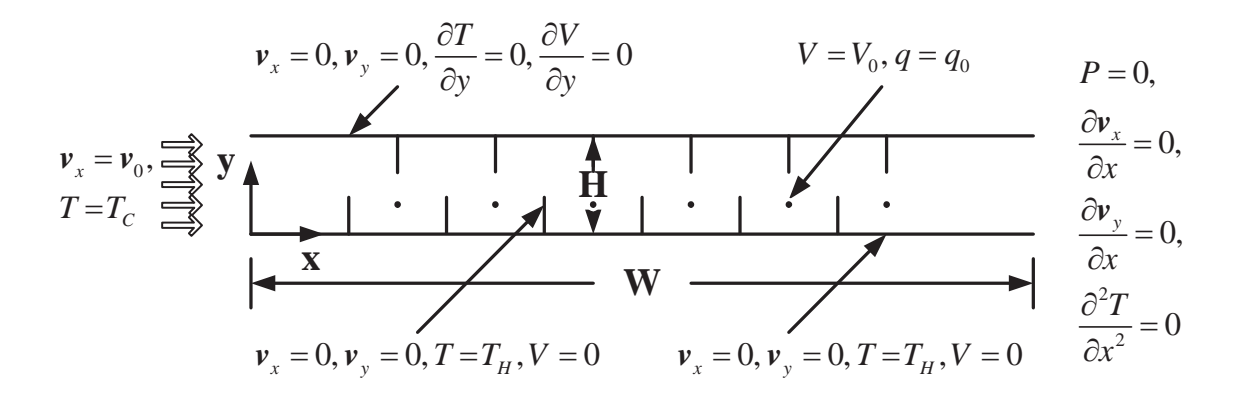


Fig. 5.14 Schematic sketch of the finned channel.

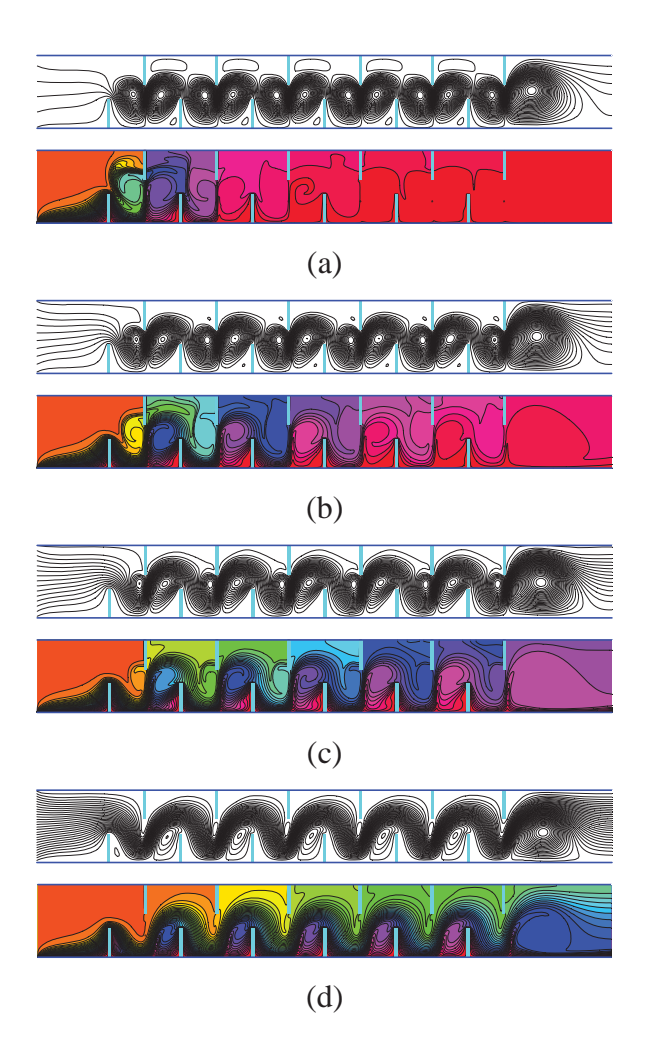


Fig. 5.15 Stream function and isotherm line contours inside the channels for various Reynolds numbers ( $V_0 = 12 \text{ kV}$ ,  $N_f = 6$ ,  $N_e = 6$ ,  $L_{fit} = 0.4$ , and  $L_{fl} = 0.4$ ): (a) Re =  $10^2$ , (b) Re =  $5 \times 10^2$ , (c) Re =  $10^3$ , and (d) Re =  $2 \times 10^3$ .

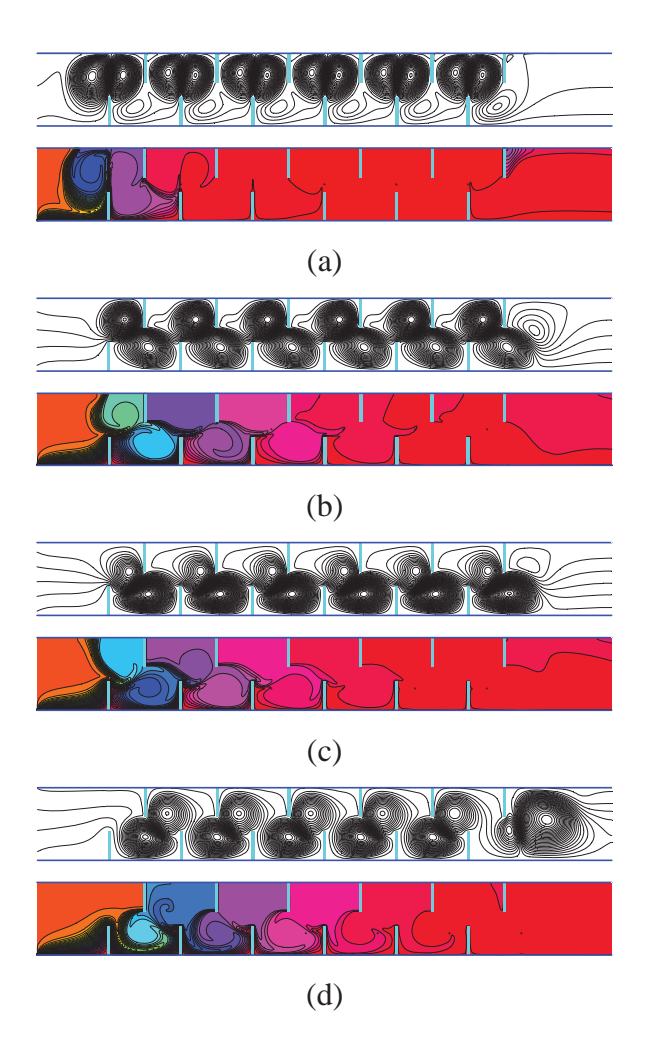


Fig. 5.16 Stream function and isotherm line contours inside the channels for various electrode arrangement ( $V_0 = 12.0 \text{ kV}$ , Re =  $10^2$ ,  $N_f = 6$ ,  $N_e = 6$ ,  $L_{fu} = 0.4$ , and  $L_{fl} = 0.4$ ): (a) x is on the lower fin strip, y = 2.5 cm, (b) x is behide the lower fins by 1.25 cm, y = 2.5 cm, (c) x is behide the lower fins by 1.25 cm, y = 1.5 cm, and (d) x is behide the lower fins by 3.75 cm, y = 1.5 cm.

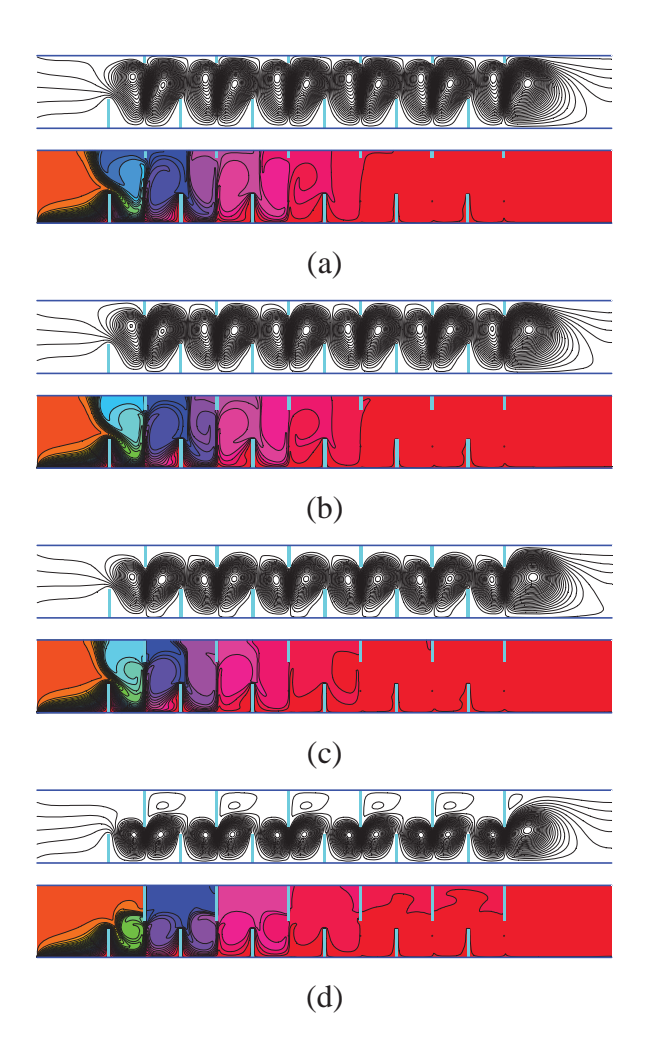


Fig. 5.17 Effect of the upper fin length on the flow and temperature fields ( $V_0 = 12.0 \text{ kV}$ , Re =  $10^2$ ,  $N_f = 6$ ,  $N_e = 6$ , and  $L_{fl} = 0.4$ ): (a)  $L_{fu} = 0.1$ , (b)  $L_{fu} = 0.2$ , (c)  $L_{fu} = 0.3$ , and (d)  $L_{fu} = 0.5$ .

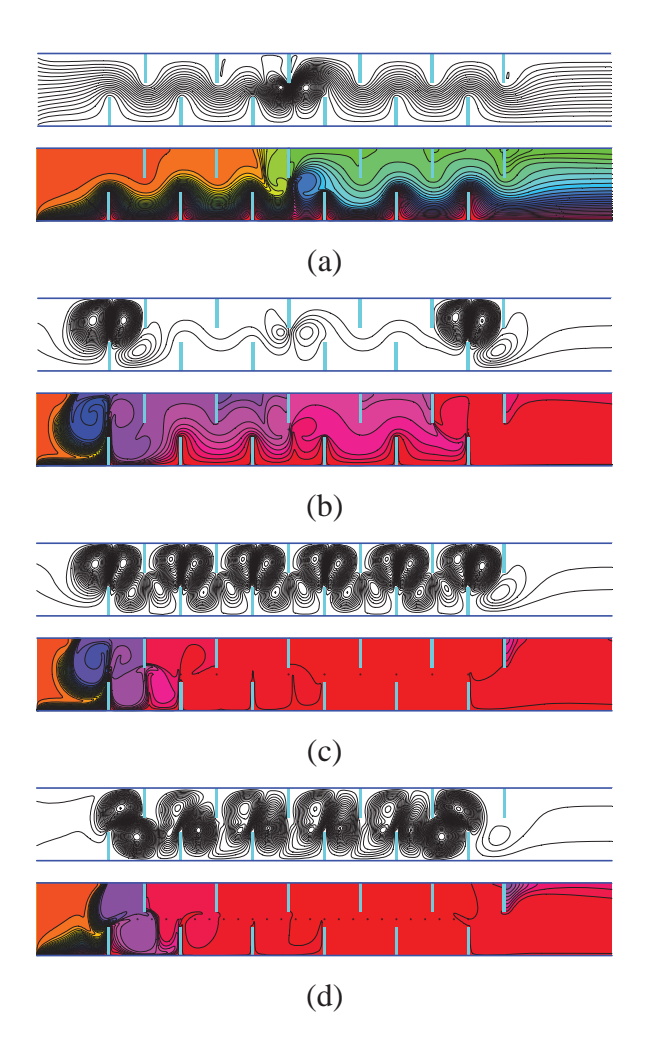


Fig. 5.18 Number of electrodes effect on the flow and temperature fields inside the finned channels ( $V_0 = 12.0 \text{ kV}$ , Re =  $10^2$ ,  $N_f = 6$ ,  $L_{fu} = 0.4$ , and  $L_{fl} = 0.4$ ): (a)  $N_e = 1$ , (b)  $N_e = 3$ , (c)  $N_e = 11$ , and (d)  $N_e = 26$ .

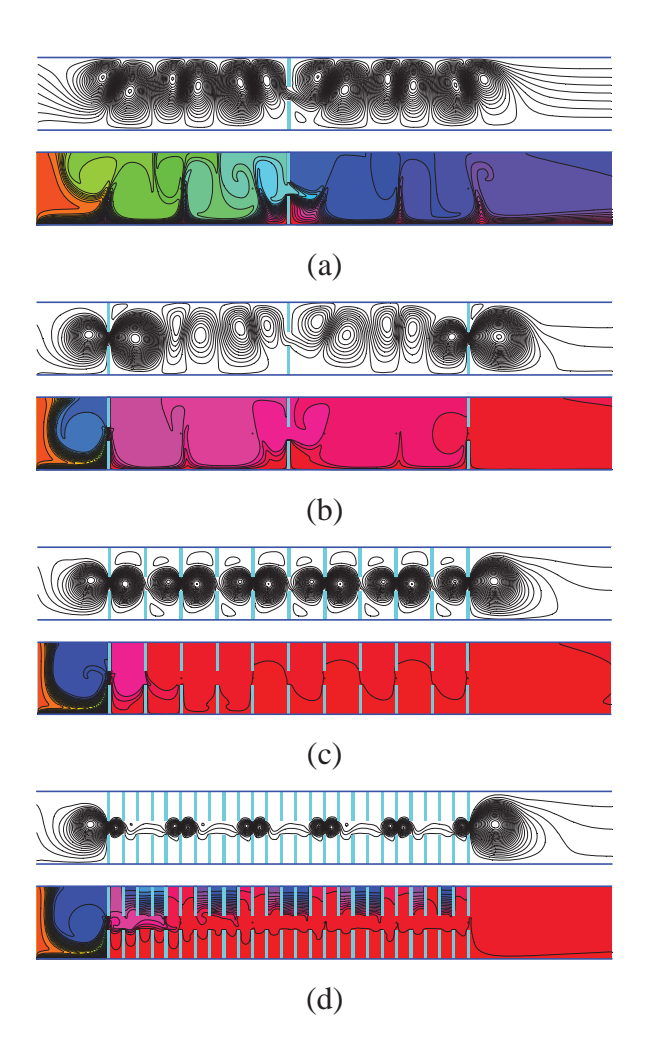


Fig. 5.19 Number of fins effect on the flow and temperature fields inside the finned channels ( $V_0 = 12.0 \text{ kV}$ , Re =  $10^2$ ,  $N_e = 6$ ,  $L_{fu} = 0.4$ , and  $L_{fl} = 0.4$ ): (a)  $N_f = 1$ , (b)  $N_f = 3$ , (c)  $N_f = 11$ , and (d)  $N_f = 26$ .

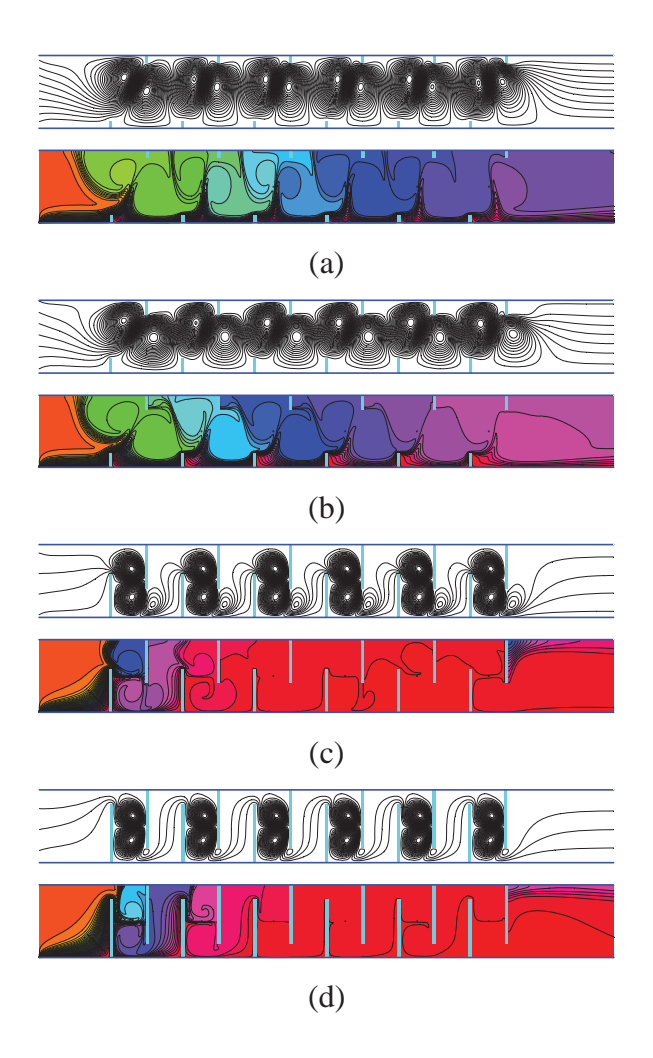


Fig. 5.20 Stream function and isotherm line contours inside the finned channels for various fin lengths ( $V_0 = 12.0 \text{ kV}$ , Re =  $10^2$ ,  $N_f = 6$ , and  $N_e = 6$ ): (a)  $L_{fu}$  and  $L_{fl} = 0.1$ , (b)  $L_{fu}$  and  $L_{fl} = 0.2$ , (c)  $L_{fu}$  and  $L_{fl} = 0.6$ , and (d)  $L_{fu}$  and  $L_{fl} = 0.8$ .

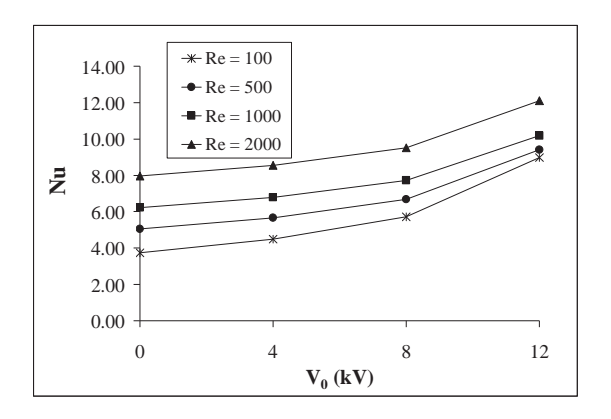


Fig. 5.21 Nusselt number as a function of the Reynolds number ( $N_f = 6$ ,  $N_e = 6$ ,  $L_{fu} = 0.4$ , and  $L_{fl} = 0.4$ ).

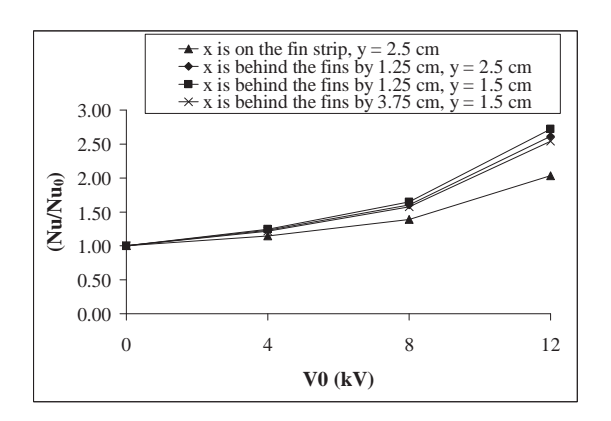


Fig. 5.22 Effect of the electrode arrangement on the heat transfer (Re =  $10^2$ ,  $N_f = 6$ ,  $N_e = 6$ ,  $L_{fu} = 0.4$ , and  $L_{fl} = 0.4$ ).

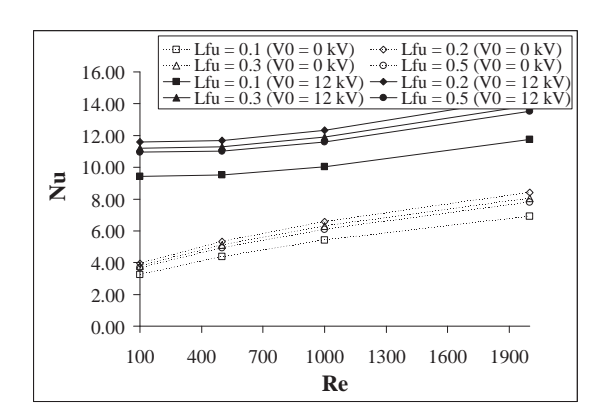


Fig. 5.23 Effect of the upper fin length on the heat transfer ( $N_f = 6$ ,  $N_e = 6$ , and  $L_{fl} = 0.4$ ).

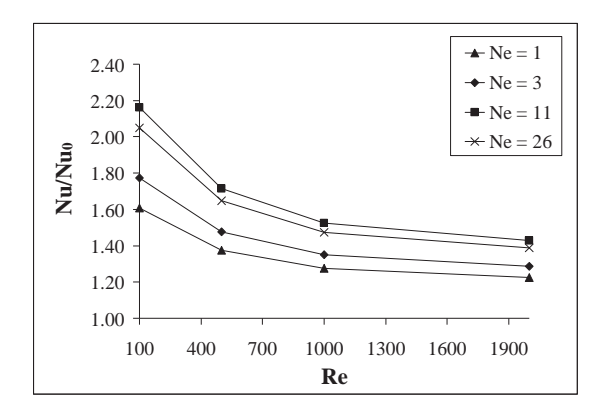


Fig. 5.24 Nusselt number for various number of electrodes ( $V_0 = 12.0 \text{ kV}$ ,  $N_f = 6$ ,  $L_{fu} = 0.4$ , and  $L_{fl} = 0.4$ ).

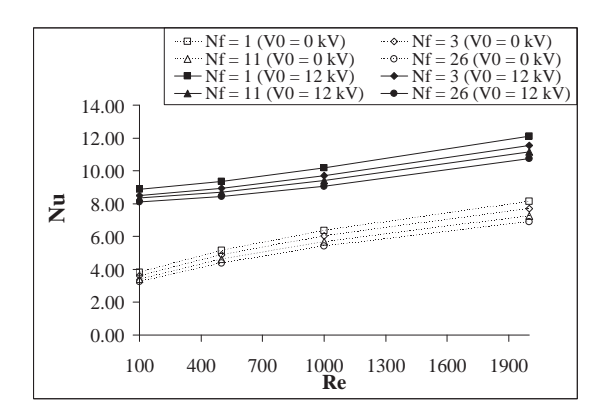


Fig. 5.25 Number of fins effect on the Nusselt number ( $N_e = 6$ ,  $L_{fiu} = 0.4$ , and  $L_{fl} = 0.4$ ).

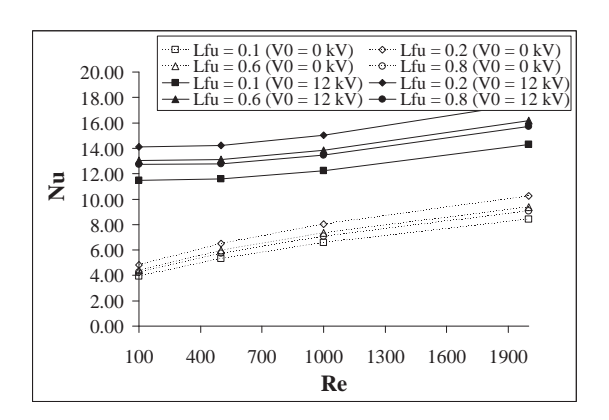


Fig. 5.26 Nusselt number at each fin length ( $N_f = 6$  and  $N_e = 6$ ).

The air convection heat transfer in a square cross-sectional duct confined to a magnetic field is schematically shown in Fig. 5.27. The cold air flows through the duct with the constant surface temperature  $T_{\rm w}$ . The duct is placed in the magnetic field resulting from the permanent magnets.

In the simulation, the side length D of the cross-section of the duct is 0.03 m, while the length L of the duct is 0.15 m. Considering that the size in the axial direction is sufficiently larger than that in the spanwise direction, the magnetic fields assumed to be two dimensional. The relative magnetic permeability of permanent magnet is taken to be 1.05 and the coercive force is set to be  $9.65 \times 10^5$  A/m.

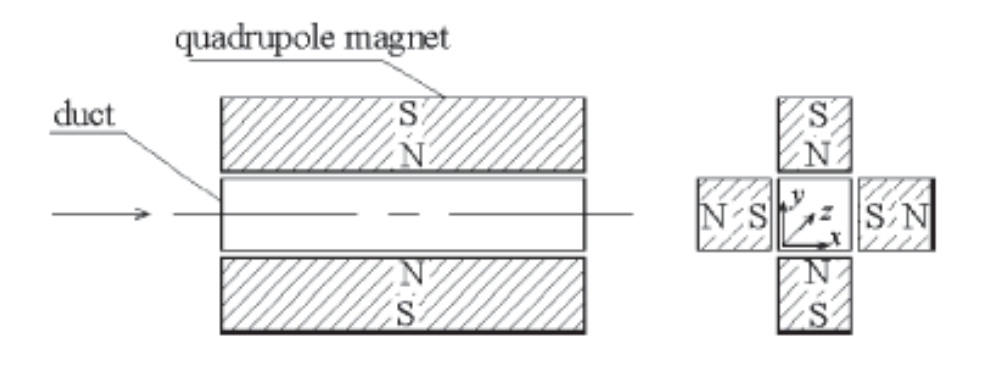


Fig. 5.27 Schematic of air convection heat transfer in a rectangular duct confined to a magnetic field.

The calculated magnetic field intensity over the square cross-section of the duct is shown in Fig. 5.28. The magnetic field intensity exhibits a general profile of a central symmetry about the axis. Fig. 5.29 is the vector plot of the magnetic acceleration. Magnetic acceleration is identical in direction with the magnetic force. Therefore, the air in the magnetic field is subjected to a centrifugal-form magnetic body force in the spanwise direction.

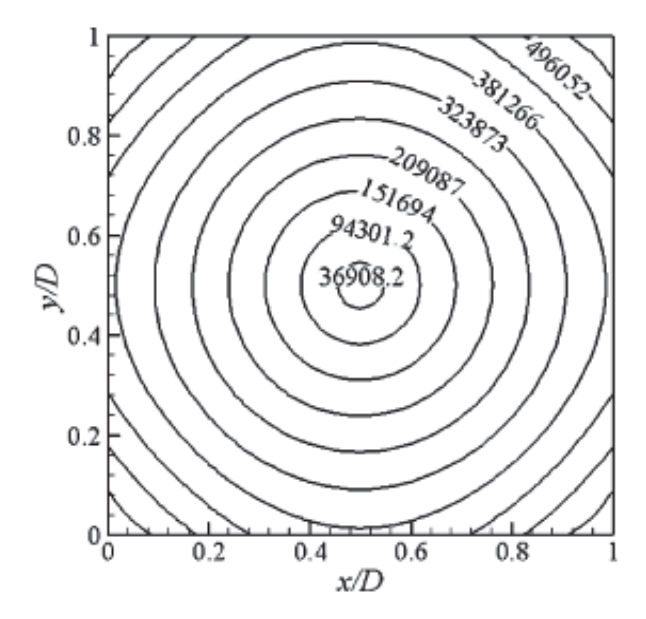


Fig. 5.28 Magnetic field intensity in the cross-section of the duct.

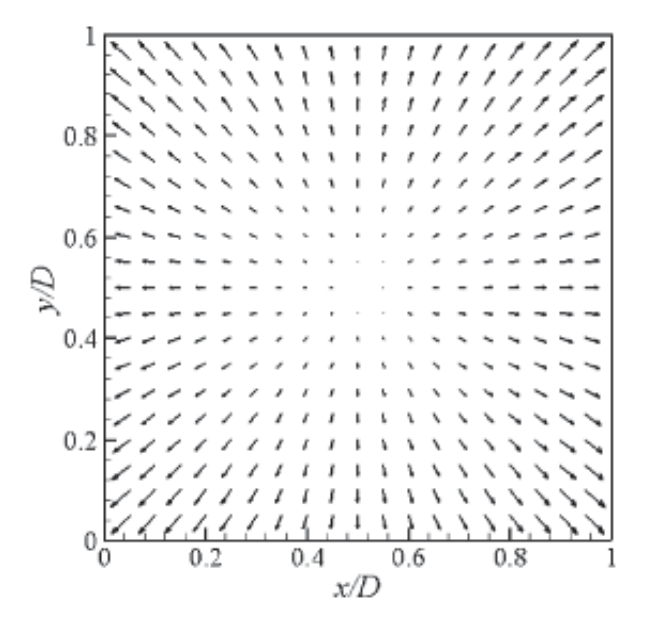


Fig. 5.29 Magnetic acceleration in the cross-section of the duct.

For hydraulic/thermal entrance, the air velocity and temperature are both uniform at the inlet and simultaneously develop as the air proceeds. The magnetic buoyancy force caused by the temperature gradient drives the air flow in the spanwise direction, forming eight longitudinal vortices. Fig. 5.30 illustrates the evolution process of the longitudinal vortices along the axis of the rectangular duct at the wall temperature of 400 K and Reynolds number of 200. In the figure, the lines are the isothermals and the vectors express the spanwise components of velocities. Further, the contour labels denote the air temperatures. The spanwise velocity is zero at the entrance, shows almost no distribution at z/L = 0.0083 (Fig. 5.30a) and a pronounced distribution at larger z/L (Fig. 5.30b-f). Eight central symmetry vortices are found to be formed. Corresponding to the distribution of the spanwise velocity, the isothermals are almost parallel to the duct wall at z/L = 0.0083 (Fig. 5.30a) and indicates more pronounced shape changes at larger z/L (Fig. 5.30b–f). At about z/L = 0.292 as shown in Fig. 5.30c, the velocity of the longitudinal vortices attain its maximum. When the air goes downstream, its temperature increases further and the temperature profile in the cross-section tends to be uniform, therefore, the velocities of the longitudinal vortices will be decreased since the magnetic buoyancy force becomes weak.

For the laminar hydrodynamic entrance, friction coefficients are plotted on Fig. 5.31 in term of f Re and Re, where f is the friction coefficient and Re the Reynolds number, respectively. They are expressed as

$$f = \frac{\Delta p}{\frac{1}{2}\rho V^2 \frac{L}{D}}$$

$$Re = \frac{wD}{v}$$

The product of the f and Re increases monotonously with increasing the Reynolds numbers without the magnetic field. When the magnetic field is added, the f Re presents very different changing trends. For wall temperatures higher than 350 K, as the Re is increased, the f Re initially decreases, after reaching the minimum at a certain Re, turns to increase. This can be clarified as such a result that the effect of the longitudinal vortices becomes relatively weak with increasing the Reynolds number (axial component of velocity) and it leads to a decrease for the friction coefficient. As the Reynolds number continues to

increase, the high axial component of velocity will result in the increase of the friction coefficient. So f Re begins to increase when the Reynolds number develops to a certain value with the magnetic field present.

The bulk air temperatures along the axis of the duct for the wall temperature of 400 K are shown in Fig. 5.32. As the uniform inlet velocity increases, that is, with increasing the Reynolds number, the bulk temperatures decrease. It shows that the air goes downstream rapidly before it can be heated adequately for the high Reynolds numbers. By application of the magnetic field, the bulk temperatures are markedly increased. It indicates that more heat has been transferred to the air and the convection heat transfer is enhanced due to the longitudinal vortices. Also as shown in Fig. 5.32, the outlet bulk temperature for the Reynolds number of 400 with the magnetic field present is higher than that for the Reynolds number of 200 without the magnetic field. For other cases, the outlet bulk temperature develops in much the same manner, that is, the outlet bulk temperature of air for a higher Reynolds number in the presence of the magnetic field is larger than that for a lower Reynolds number with no magnetic field present. The bulk temperature changing trends as the air proceeds can partially show that the convection heat transfer is enhanced by application of the magnetic field.

Fig. 5.33 shows the Nusselt numbers plotted as a function of the Reynolds numbers and wall temperatures. The Nusselt number is defined as

$$Nu = \frac{q}{4L\Delta Tk}$$

where q denotes the heat transfer rate through the wall,  $\Delta T$  denotes the log-mean temperature difference between the wall and air. For the same Reynolds numbers, the Nusselt numbers of air convection heat transfer in the magnetic field are increased compared with those of convection heat transfer with the magnetic field absent. And moreover, the Nusselt numbers with the magnetic field present are related to the wall temperatures, however, they are independent of the wall temperatures for the convection heat transfer with no magnetic field present. The Nusselt numbers increase with increasing the wall temperatures at the same Reynolds numbers. It can be explained from the momentum equation. The last term in the right hand side denotes the buoyancy force induced by the magnetic field. The higher the wall temperature, the higher the air

temperature and the larger the magnetic buoyancy force acting on the air. Consequently, the velocity component in the spanwise direction will increase and more heat will be transferred from the wall to air. The dependence of the Nusselt numbers on the Reynolds numbers with the magnetic field present can be found very different from that without the magnetic field from Fig. 5.33. With increasing the Reynolds numbers, the Nusselt numbers increase monotonously with no magnetic field present. However, when the magnetic field is applied, the Nusselt number shows unlike rules. For wall temperatures higher than 350 K, as the Reynolds number increases, the Nusselt number increases at first, then reaches its local maximum at a certain Re, and then decreases, finally it turns to increase again. For wall temperatures lower than 350 K, the Nusselt number increases all along with increasing the Reynolds numbers. The combined effect of the longitudinal vortices and the axial flows results in the above results. For high wall temperatures and low Reynolds numbers, the axial flows play a key role in the heat transfer enhancement as the Reynolds number increases, though the longitudinal vortices will become weak and lead to a reduced heat transfer enhancement with increasing the Reynolds number, the integrated action of air flows in the spanwise and axial directions will still enhance the heat transfer process. When the axial component of velocity (Reynolds number) continues to increase, the longitudinal vortices become much weaker, that is, the air goes downstream quickly before it can flow sufficiently in the spanwise direction. In this case the heat transfer enhancement will be reduced to some extent by the combined effect of the axial and spanwise flows. As the axial component of velocity increases further, the longitudinal vortices are difficult to form, but the powerful mainstream will work to enhance the heat transfer, so the Nusselt number increases again with increasing the Reynolds number. At Re = 2000, the convection heat transfers with the magnetic field present and absent have little differences.

As mentioned above, the application of the magnetic field brings not only the enhanced heat transfer but also the increase of the friction coefficient, that is, the going up of the power cost. The following performance evaluation criterion PEC is used to investigate the combined hydrodynamic and thermal effect.

$$PEC = \frac{Nu / Nu_0}{f / f_0}$$

Here,  $Nu_0$  and  $f_0$  are the Nusselt number and friction coefficient without the magnetic field, respectively; Nu and f are the Nusselt number and friction coefficient with the magnetic field present, respectively. At the same Reynolds number,  $f/f_0$  denotes the ratio of the power cost and  $Nu/Nu_0$  represents the heat transfer enhancement ratio.

Fig. 5.34 is the PEC variations with the Reynolds numbers and wall temperatures. Except the PEC of the convection heat transfer at the 320 K wall temperature, the other PEC values are more than unity. It shows that by application of the magnetic field to the hydraulically and thermally developing flow, the air convection heat transfer is really enhanced. Also shown in Fig. 5.34 is that at Re = 200, the PEC with the 400 K wall temperature is lower than that with the 380 K wall temperature, and the PEC with the 380 K wall temperature is lower than that with the 350 K wall temperature. It shows that at high wall temperatures, the friction coefficient increasing rate is higher than the Nusselt number increasing rate with increasing the wall temperature. As the Reynolds number increases, the PEC decreases. At the same Reynolds numbers, the PEC of the convection heat transfer increases with increasing the wall temperature because the wall temperature increase brings a higher Nusselt number increasing rate than the friction coefficient increasing rate. At the wall temperature of 400 K and Reynolds number of 400, PEC attains its maximum of about 1.11, the heat transfer enhancement achieves its best effect.

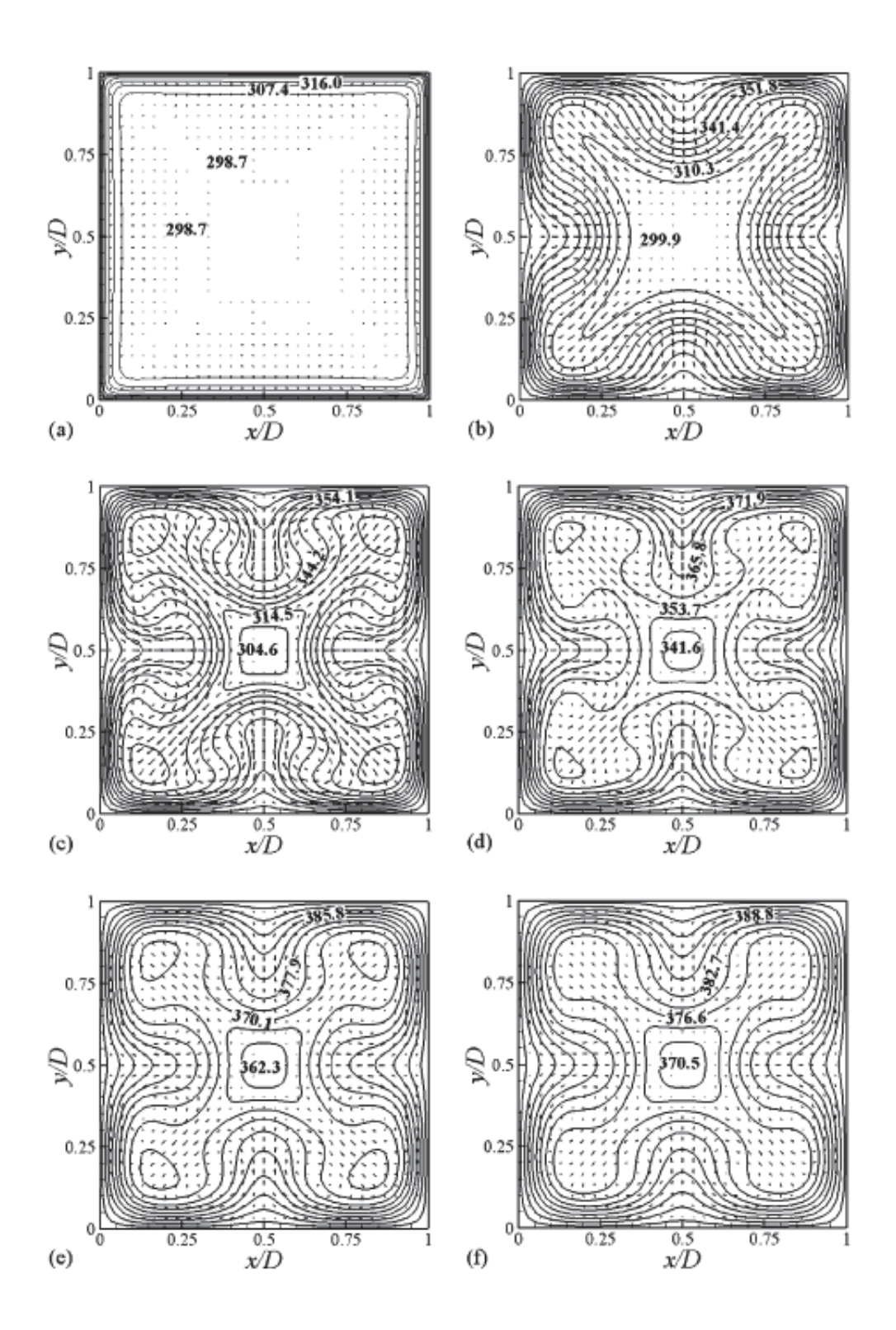


Fig. 5.30 The velocity and temperature fields at different cross-sections of the duct by application of the magnetic field at wall temperature of 400 K and Reynolds number of 200 for hydraulically and thermally developing flow. (a) z/L = 0.0083, (b) z/L = 0.192, (c) z/L = 0.292, (d) z/L = 0.492, (e) z/L = 0.792, (f) z/L = 0.992.

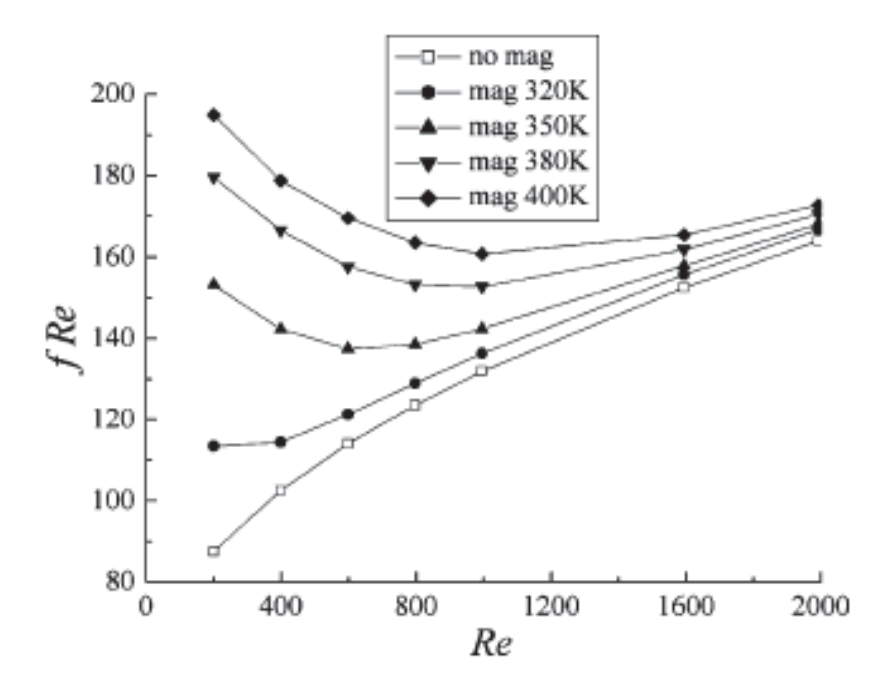


Fig. 5.31 Friction coefficients for hydraulically and thermally developing flow.

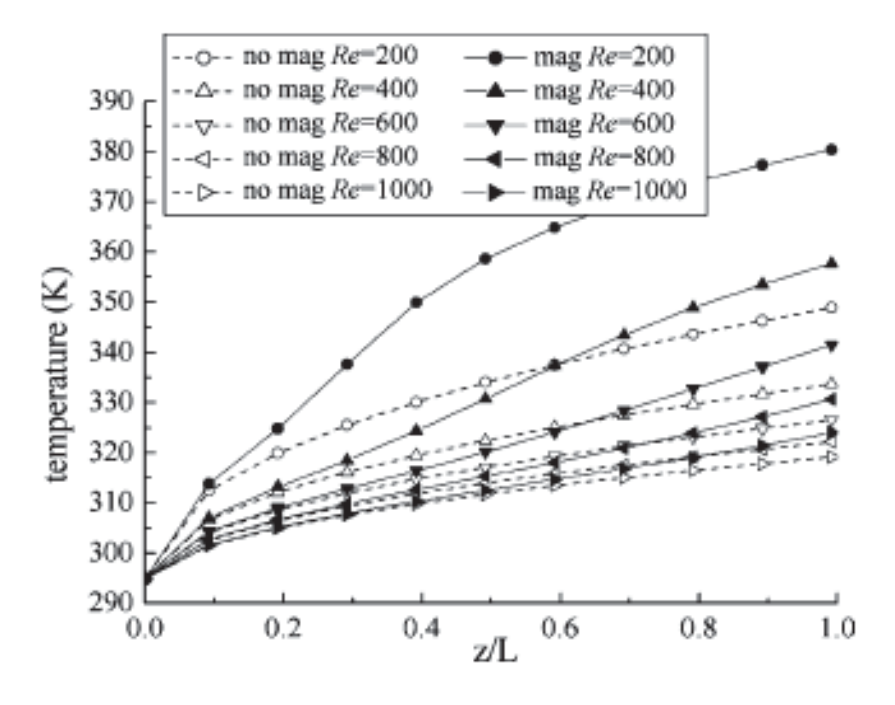


Fig. 5.32 Variations of the bulk air temperatures along the axis of the duct at wall temperature of 400 K for hydraulically and thermally developing flow.

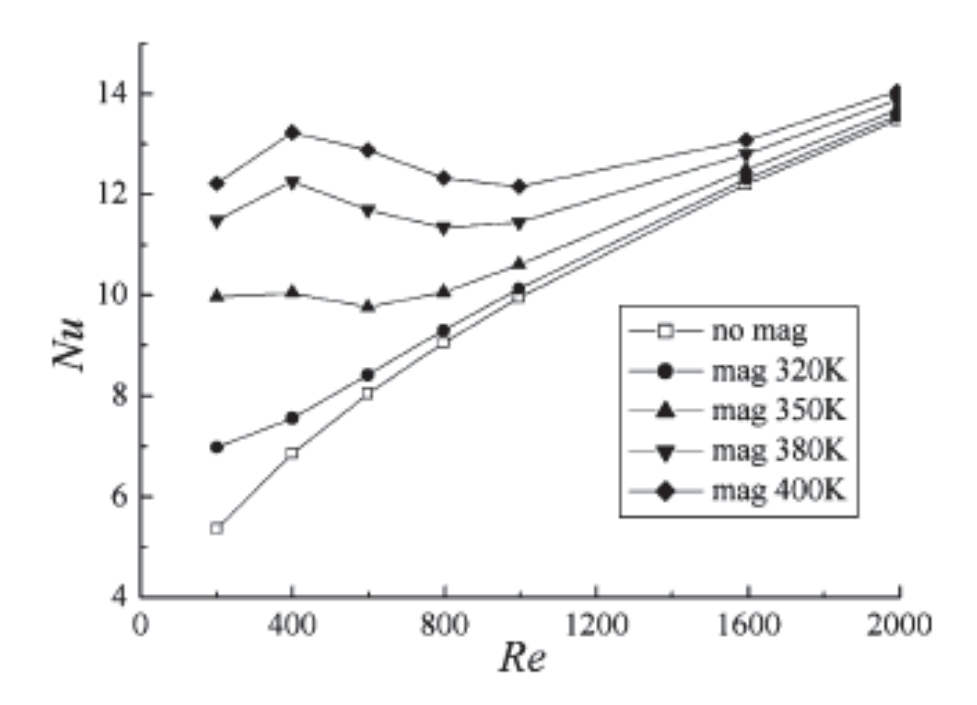


Fig. 5.33 Variations of Nusselt numbers with Reynolds numbers and wall temperatures for hydraulically and thermally developing flow.

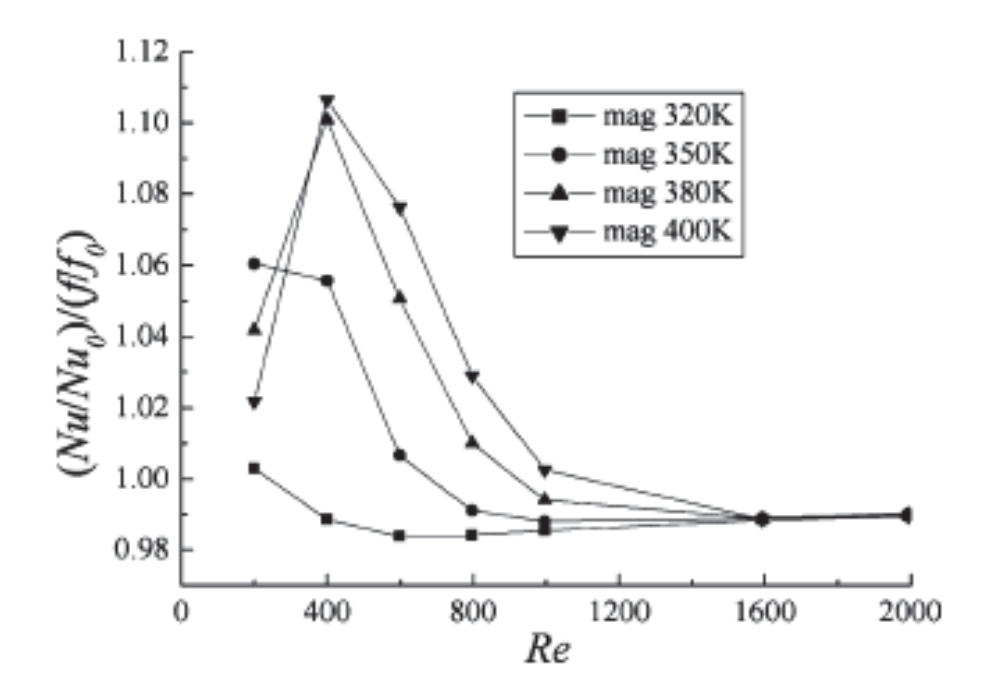


Fig. 5.34 Comprehensive heat transfer enhancement ratio for hydraulically and thermally developing flow.

When the centrifugal-form magnetic body force acts on the air flows that the velocity and temperature profiles are fully developed, the spanwise flows will also occur. The isothermals and the spanwise components of velocities are plotted on Fig. 5.35. Since the temperature field has been fully developed before the magnetic field is applied, the magnetic buoyancy force resulting from the temperature gradient will drive spanwise flows in the beginning. As shown in Fig. 5.35a is that the longitudinal vortices can form once the magnetic field acts on the air. This is different from the hydraulically and thermally developing flow in which no spanwise flows occur in the beginning. But at this case, the velocity is very low and no more heat is brought to the air from the wall, therefore the temperature profile in the cross-section changes little and presents the concentric distribution as same as the fully developed temperature without the action of any body force. When the air flows downstream, the spanwise component of velocity begins to increase and the longitudinal vortices can be clearly observed. At about z/L = 0.392, the velocity of the longitudinal vortices attains its maximum and then it decreases. It shows that the compound effect of the magnetic buoyancy force and the external means works to drive air flows at z/L = 0.392 to the utmost extent in the spanwise direction. Moreover, the magnetic buoyancy force decreases and the longitudinal vortices get weak.

Fig. 5.36 gives the friction coefficients plotted in the form of f Re =  $\phi$  (Re). For the fully developed flows without any body force, this value remains constant of 57. By application of the magnetic field, the longitudinal vortices result in the increased friction coefficients. As the Reynolds number increases, f Re decreases because the longitudinal vortices become weak. However, f Re increases with increasing the wall temperatures because the longitudinal vortices become more powerful at high wall temperatures.

The Nusselt number for the fully developed flows with no magnetic field present also remains constant. With application of the magnetic field, the Nusselt number increases due to the longitudinal vortices. The dependence of the Nusselt numbers on the Reynolds numbers and wall temperatures are illustrated in Fig. 5.37. As the Reynolds numbers increase, the Nusselt numbers of air convection heat transfer with the magnetic field present decrease and approach to the Nusselt number with no magnetic field present. It shows that the enhancement of convection heat transfer due to the longitudinal vortices becomes weak with increasing the Reynolds numbers. However, as the wall temperature increases, the Nusselt numbers will become increased. At Re = 200 and wall temperature

of 400 K, the Nusselt number increases from 2.98 without the magnetic field to 10.3 with the magnetic field present and increases by 246%.

The comprehensive heat transfer enhancement ratio PEC is plotted as the function of the Reynolds numbers and the wall temperatures as shown in Fig. 5.38. The changing tendencies are almost the same as those for hydraulically and thermally developing flow. But this value for the fully developed flow is always higher than unity, that is, the application of the magnetic field can all the time be valid for the heat transfer enhancement. And furthermore, this value is higher than that for the hydraulically and thermally developing flow at the same Reynolds number and wall temperature. At Reynolds number of 400 and the 400 K wall temperature, this heat transfer enhancement ratio changes from 1.11 for the developing flow to 1.27 for the fully developed flow. It shows that the application of the magnetic field to the hydraulically and thermally fully developed flow is more effective.

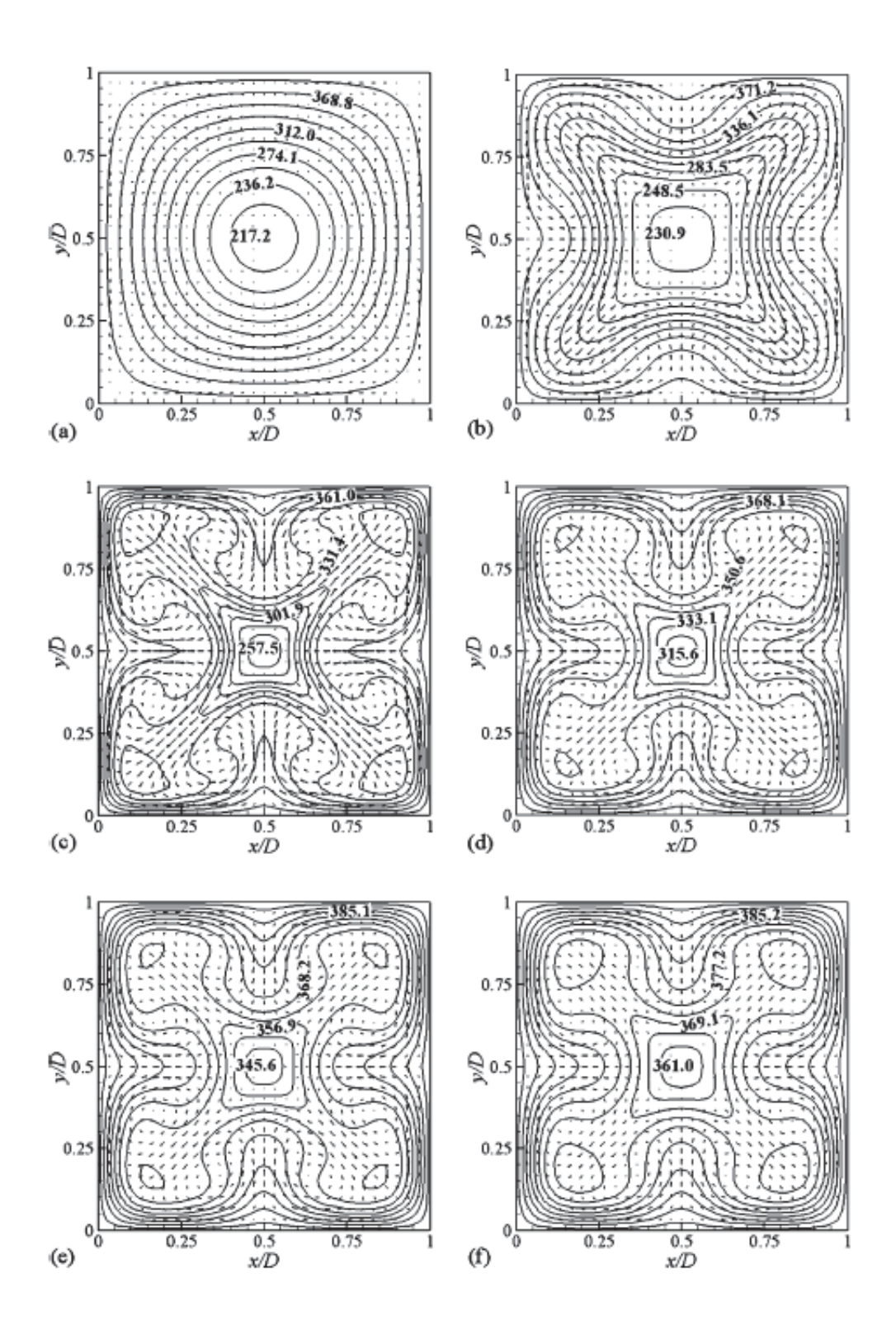


Fig. 5.35 The velocity and temperature fields at different cross-sections of the duct by application of the magnetic field at wall temperature of 400 K and Reynolds number of 200 for hydraulically and thermally fully developed flow. (a) z/L = 0.0083, (b) z/L = 0.192, (c) z/L = 0.292, (d) z/L = 0.492, (e) z/L = 0.792, (f) z/L = 0.992.

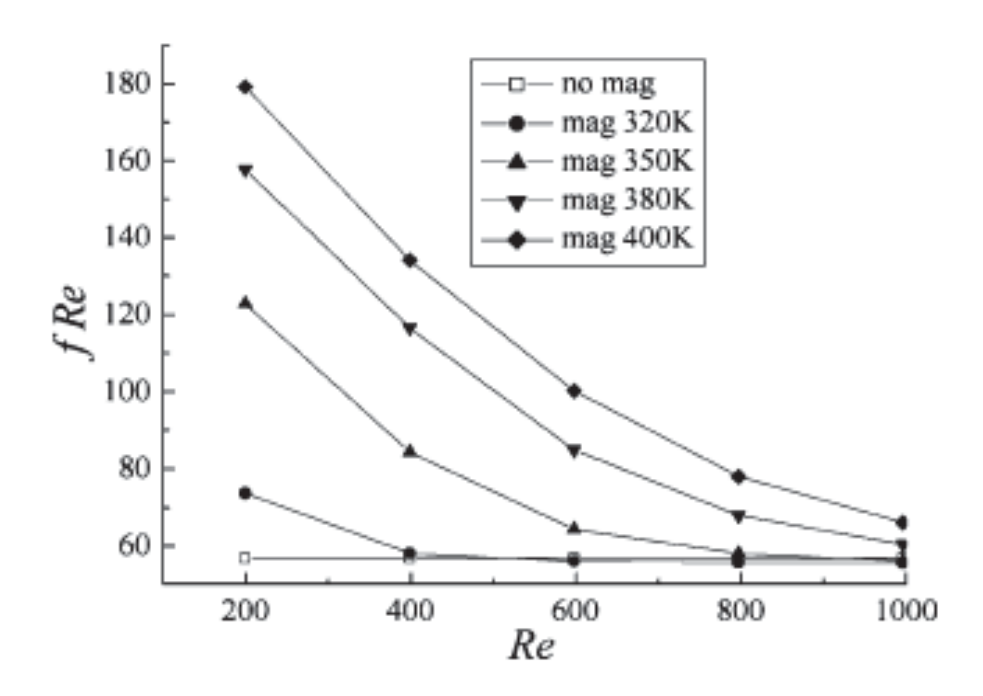


Fig. 5.36 Friction coefficients for hydraulically and thermally fully developed flow.

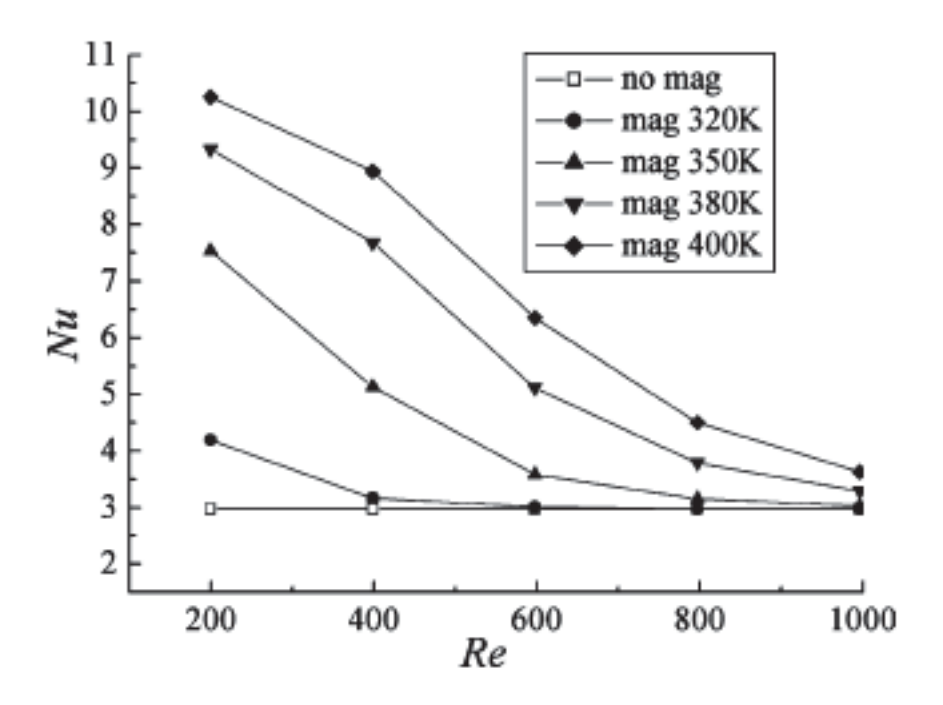


Fig. 5.37 Variations of Nusselt numbers with Reynolds numbers and wall temperatures for hydraulically and thermally fully developed flow.

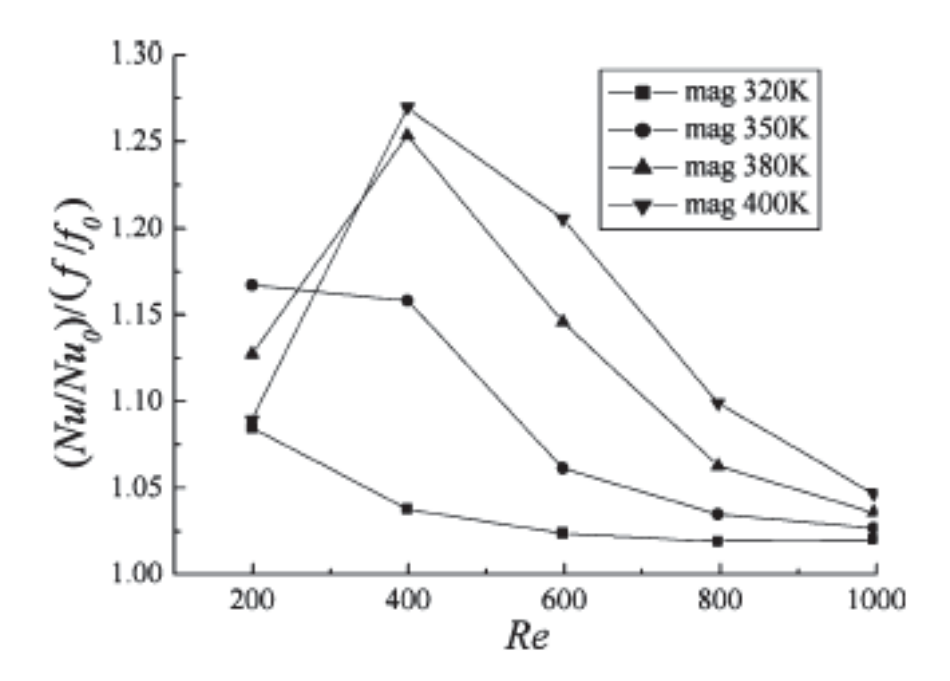


Fig. 5.38 Comprehensive heat transfer enhancement ratio for hydraulically and thermally fully developed flow.

The spanwise flows will also occur due to the gravitational buoyancy force if the duct is placed horizontally. The evolution of the longitudinal vortices resulting from the gravitational buoyancy force along the axis of the duct at wall temperature of 400 K and Reynolds number of 200 for hydraulically and thermally developing flow is shown in Fig. 5.39. Two longitudinal vortices that exhibit lateral symmetry can be found as the air proceeds. The isothermals also present lateral symmetry, which is different from the convection heat transfer with magnetic field. The spanwise velocity shows almost no distribution and the temperature is almost uniform at z/L = 0.0083 (Fig. 5.39a). As the air proceeds, the natural convection form in the spanwise direction and the spanwise velocity shows a pronounced distribution at z/L = 0.192 (Fig. 5.39b). As the air temperature increases, the spanwise velocity will decrease due to the reduced gravitational buoyancy force. Fig. 5.40 shows the comparison of friction coefficients and Nusselt numbers between these two cases at wall temperature of 400 K for hydraulically and thermally developing flow. The friction coefficients and Nusselt numbers for the convection heat transfer with magnetic field are both higher than those for the convection heat transfer with gravitational buoyancy force. For hydraulically and thermally fully developed flow, the longitudinal vortices will also present lateral symmetry, the flow and heat transfer are almost as same as those for hydraulically and thermally developing flow.

The comparison between the effects of magnetic and gravitational buoyancy force on convection heat transfer shows that they have different functions for air flow and heat transfer. In addition, gravitational buoyancy force can not arise in space vehicles, but the convection heat transfer can still be enhanced by using magnetic field in microgravity environment.

If the rectangular duct is placed vertically, the longitudinal vortices can not arise from the natural convection. It shows that the formation of the longitudinal vortices due to the natural convection is dependent on the orientation of the duct, however, the longitudinal vortices can arise from the magnetic buoyancy force all the time, no matter the duct is placed vertically or horizontally.

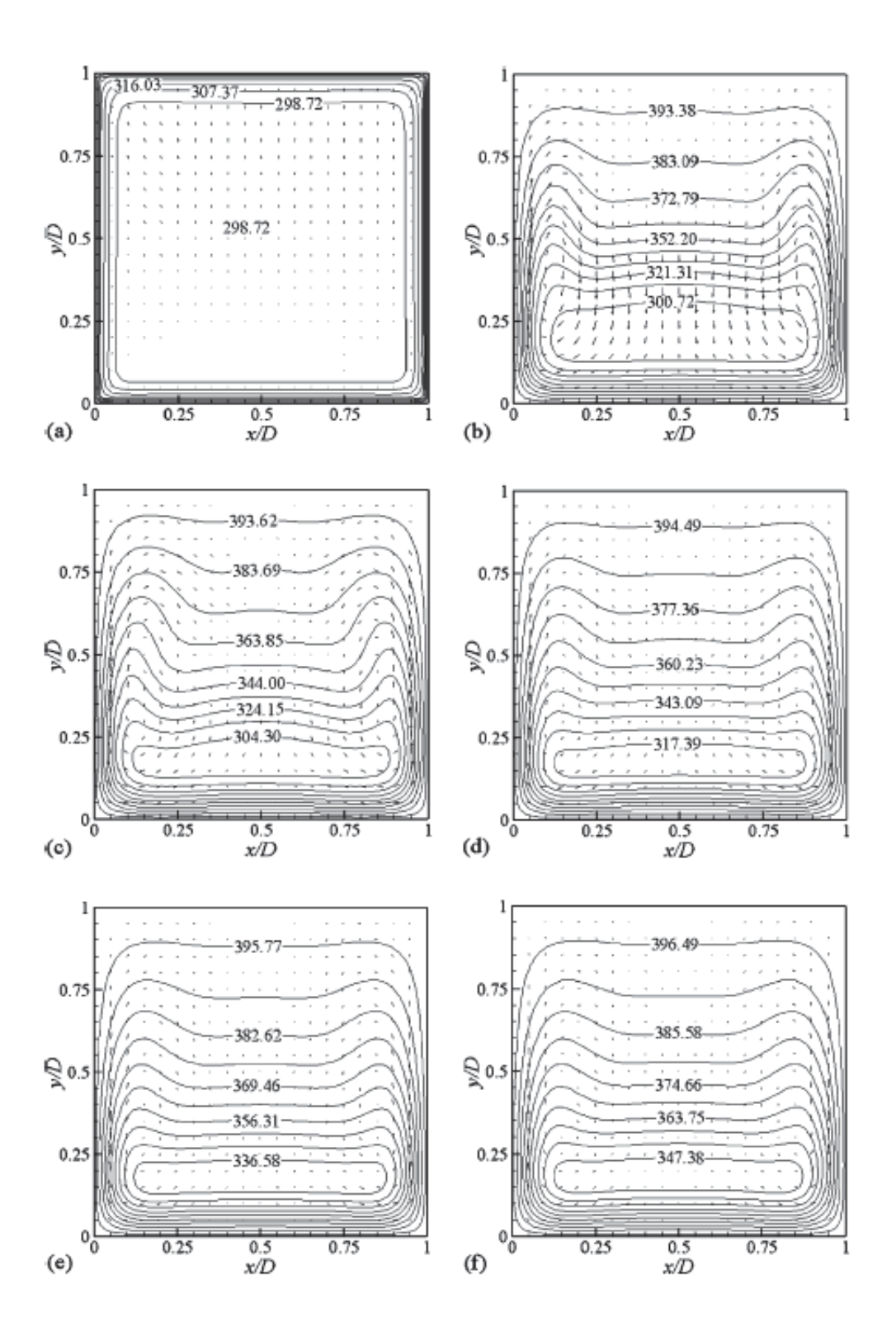


Fig. 5.39 The velocity and temperature fields resulting from the gravitational buoyancy force at different cross-sections of the duct at wall temperature of 400 K and Reynolds number of 200 for hydraulically and thermally developing flow. (a) z/L = 0.0083, (b) z/L = 0.192, (c) z/L = 0.292, (d) z/L = 0.492, (e) z/L = 0.792, (f) z/L = 0.992.

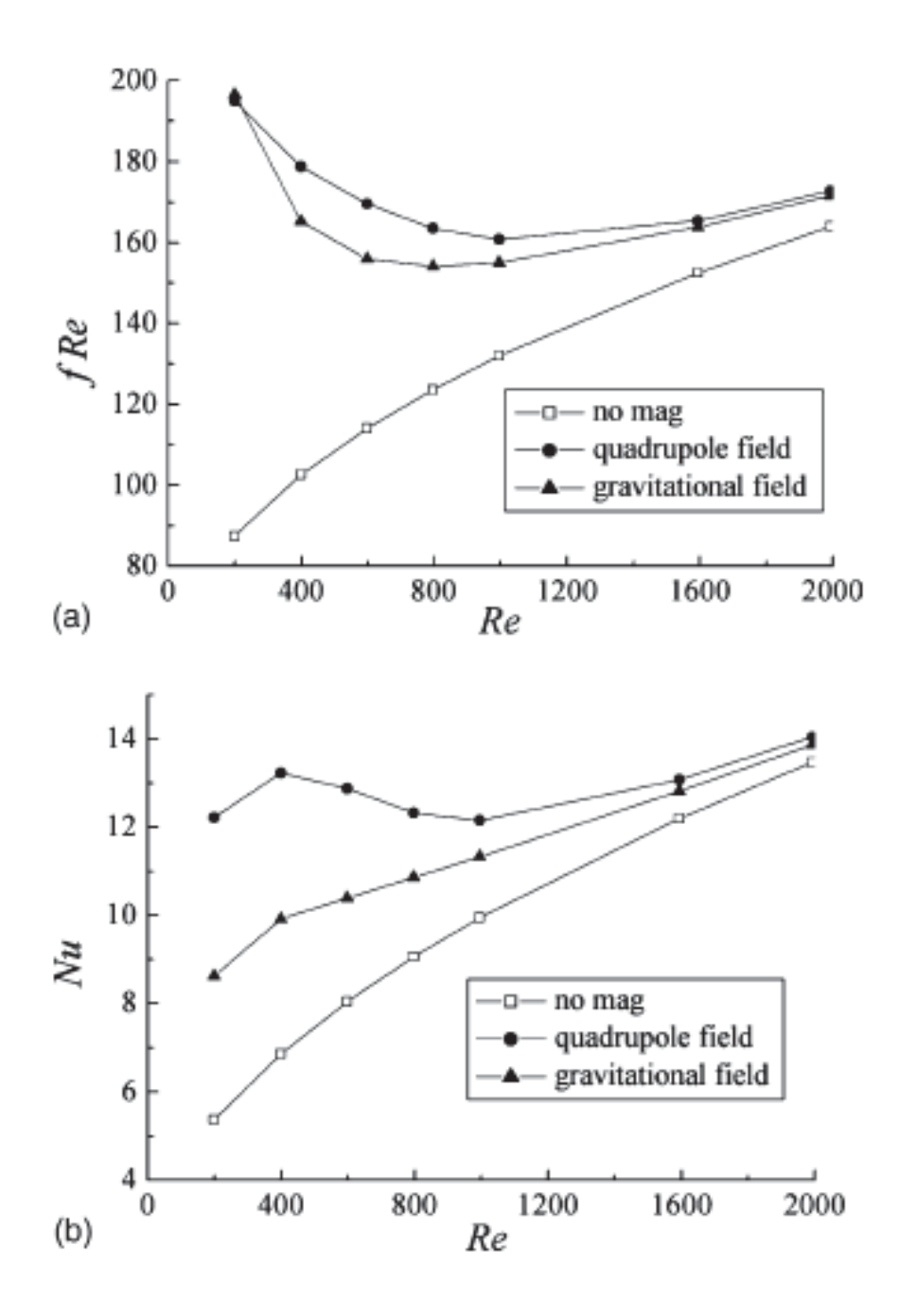


Fig. 5.40 Comparison between effects of magnetic and gravitational buoyancy force on convection heat transfer at wall temperature of 400 K for hydraulically and thermally developing flow: (a) friction coefficients and (b) Nusselt numbers.

The laminar flow and heat transfer characteristics of air convection for the hydraulically and thermally developing and fully developed flows on which the magnetic field acts were numerically investigated. For these two cases, eight longitudinal vortices form in the cross-section of the duct as air proceeds and the convection heat transfer is therefore enhanced due to the spanwise flows.

For hydraulically and thermally developing flow, the temperature field is uniform and the longitudinal vortices resulting from the magnetic buoyancy force can not form in the beginning. As the air proceeds, the longitudinal vortices develop gradually in the spanwise direction. For high wall temperatures, the f Re initially decreases, and then increases instead of the monotonous increase with no magnetic field present, the Nusselt numbers also exhibit different changing trends from those without the action of the magnetic field. The comprehensive heat transfer enhancement ratios for which the power loss and the enhanced heat transfer are all taken into account show that the application of the magnetic field to the hydraulically and thermally developing flow can enhance the convection heat transfer except for the convections at low wall temperatures.

When the magnetic field acts on the air flows that the velocity and temperature profiles have been fully developed, the longitudinal vortices form immediately whereas this spanwise flow is very weak. As the air continues to flow, the longitudinal vortices become powerful. After reaching the maximum spanwise velocities, they turn to decrease. The f Re decreases with increasing the Reynolds numbers and decreasing the wall temperatures. The variations of the Nusselt numbers with the Reynolds numbers and wall temperatures are the same as the changing trends of f Re. Although the f Re and the Nusselt number are all increased by application of the magnetic field, the Nusselt number enhancing rate is higher than the friction coefficient enhancing rate. The comprehensive heat transfer enhancement ratio is therefore always higher than unity, and is larger than that for the developing flow at the same Reynolds numbers and wall temperatures.

The present studies proposed a new approach for air convection heat transfer enhancement by application of the magnetic field. The results show that it can enhance the convection heat transfer for both hydraulically and thermally developing and fully developed flows. But for the fully developed flows, it is more effective.

## 5.2 Enclosure Configuration

The enclosure domain and boundary conditions are conducted in Fig. 5.41 The right thermally conducting plate is maintained at a uniform heat flux, and the left thermally conducting plate is maintained at a uniform temperature of 300 K. Both upper and lower plates are thermal insulators. All plates are electrically grounded, and the enclosure has a size of  $5 \times 40 \text{ cm}^2$ . Fig. 5.42 shows the stream function contours obtained by applying the EHD effect while the Rayleigh number is varied between 10<sup>4</sup> and 10<sup>8</sup>. In the latter cases, the effect of Joule heating at the wire electrode is negligible ( $V_0 = 17.5 \text{ kV}, N = 7$ ). There is an effect of the secondary flow induced by the ionic wind at the wire electrode, which causes four rotating cellular motions at each electrode in Fig. 5.42(a). The Rayleigh number is next increased further, until the fluid inside the enclosure is dominated by the effect of Rayleigh number instead of the electric field. The flow patterns are oscillatory due to the interaction between the thermal buoyancy force and electrical body force. Two categories of oscillation -- the periodic state of Figs. 5.42(a) and (b), and the non-periodic state of Figs. 5.42(c)-(e) -- are observed in these figures. Fig. 5.43 presents the temperature fields (isotherm lines) inside the enclosures defined in Fig. 5.42. The thermal boundary layer is perturbed by the electric field when it extends over the recirculation region. It can be seen that the temperature gradient, represented by the line density, at the right plate becomes larger with an increasing Rayleigh number, resulting in a high heat transfer coefficient. It can be concluded that for low Rayleigh number, the flow and temperature fields have been substantially affected by an electric field. However, the effect of EHD is diminished at high Rayleigh number which is an indication of no significant change in heat transfer enhancement.

The oscillatory stream function and isotherm line contours for 3, 7, 13, 26, and 51 electrodes are shown in Figs. 5.44 and 5.45 ( $V_0 = 17.5 \text{ kV}$ , Ra =  $10^6$ ). Altering the number of electrodes causes different flow patterns to occur in the enclosure. The number of vortices is seen to increase when the number of electrodes is augmented from 3 to 13, but remains relatively constant as the number of electrodes increases to 26 and 51. Large vortices appear at the upper and lower zones of the enclosures of Figs. 5.44(d) and (e), especially around the extremes of the electrode strips, due to the low pressure region. The temperature gradient along the right plate of Fig. 5.45(e) is highest in comparison to other configurations that cause the maximum heat transfer coefficient to be a maximum. One can

thus conclude that the effect of the number of electrodes is more significant at larger number values. This effect should be considered together with the extra heat transfer per unit input power of electrical energy for optimization.

A comparison of the average heat transfer enhancement over a cycle of the periodic state, or over the entire time span of the non-periodic state, along an enclosure is shown for various Rayleigh numbers in Fig. 5.46 (N = 7). The latter is evaluated using the ratio of the average Nusselt number in the presence of an electric field to that without an electric field. The results show that EHD enhancement of flow and heat transfer plays an important role in regions of low Rayleigh number, while convective heat transfer is consequently dependent on the relation between Rayleigh number and supply voltage. Fig. 5.47 demonstrates the relationship between heat transfer enhancement and number of electrodes for  $V_0 = 17.5$  kV. The enhancement ratio reaches a minimum at an intermediate number of electrodes (the combination between oscillatory cells occurs here) and increases again due to the high intensity of the electric field at higher numbers of electrodes. This phenomenon can be described by considering the isotherm line density at the right plate of Fig. 5.45(a). For the case N = 3, the density is found to be higher than for N = 7 due to the lower number of vortices and also the smaller heat trap that yields a higher heat transfer coefficient. Since the number of electrodes is rather high at N = 13, 26, and 51, many vortices are formulated along the domain of enclosure, and they combine when the number of electrodes is large, even though there is good turbulent mixing. The flow and temperature fields are recirculating and oscillating, especially around the top and bottom zones of the enclosure. Therefore, the heat transfer coefficient is augmented due to the larger ionic wind effect. Thus, the optimum number of electrodes installed in an enclosure is significantly affected.

The enhanced ratio between average fluid velocity inside the enclosure and various numbers of electrodes, averaged along the computational domain and over a period or an entire time span, is investigated in Fig. 5.48 for  $V_0 = 17.5$  kV. The velocity enhancement increases monotonically with the number of electrodes. A comparison between Figs. 5.47 and 5.21 shows that the velocity enhancement does not display a similar tendency and the heat transfer enhancement, instead increasing further with number of electrodes, while the augmentation to heat transfer shows a minimum value at an intermediate number of electrodes.

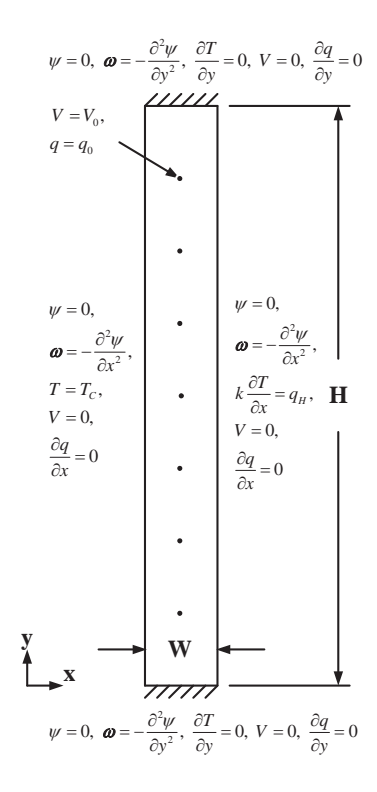
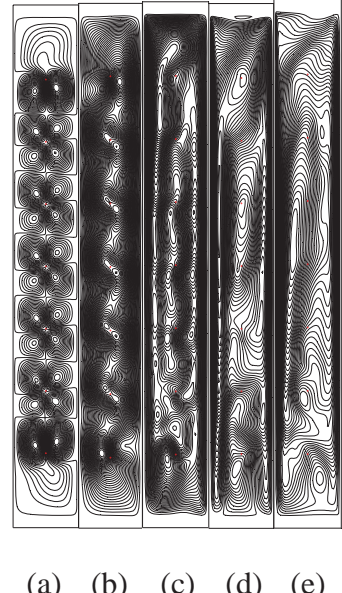


Fig. 5.41 Boundary conditions and generated grid.



(a) (b) (c) (d) (e)

Fig. 5.42 Stream function contours inside enclosure for various Rayleigh numbers ( $V_0 =$ 17.5 kV, N = 7): (a) Ra =  $10^4$ , (b) Ra =  $10^5$ , (c) Ra =  $10^6$ , (d) Ra =  $10^7$ , and (e) Ra =  $10^8$ .

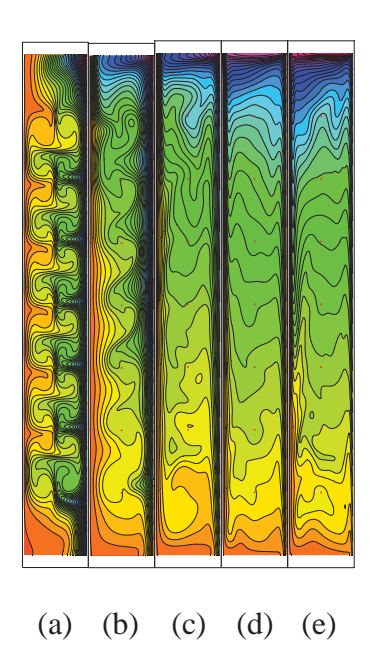


Fig. 5.43 Temperature distributions inside enclosure for various Rayleigh numbers ( $V_0 =$ 17.5 kV, N = 7): (a) Ra =  $10^4$ , (b) Ra =  $10^5$ , (c) Ra =  $10^6$ , (d) Ra =  $10^7$ , and (e) Ra =  $10^8$ .



(a) (b) (c) (d) (e)

Fig. 5.44 Stream function contours inside enclosure for various numbers of electrodes ( $V_0$ = 17.5 kV, Ra =  $10^6$ ): (a) N = 37, (b) N = 7, (c) N = 13, (d) N = 26, and (e) N = 51.

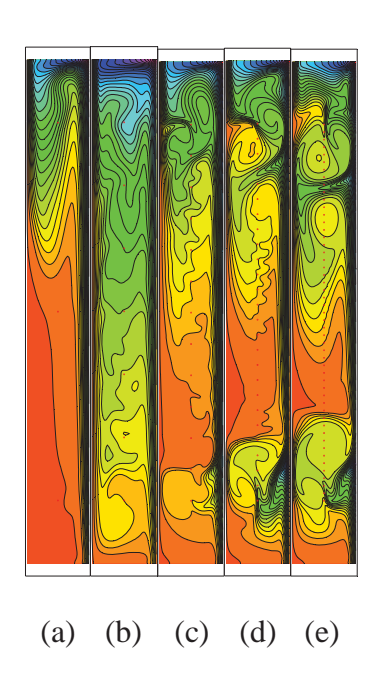


Fig. 5.45 Temperature distributions inside enclosure for various numbers of electrodes ( $V_0$ = 17.5 kV, Ra =  $10^6$ ): (a) N = 37, (b) N = 7, (c) N = 13, (d) N = 26, and (e) N = 51.

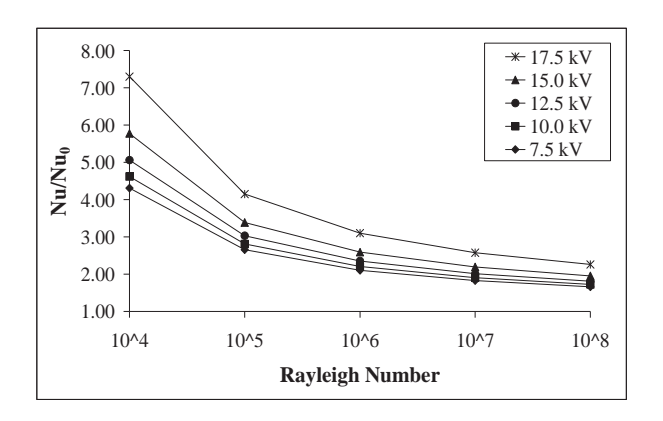


Fig. 5.46 Heat transfer enhancement in relation to supply voltage (N = 7).

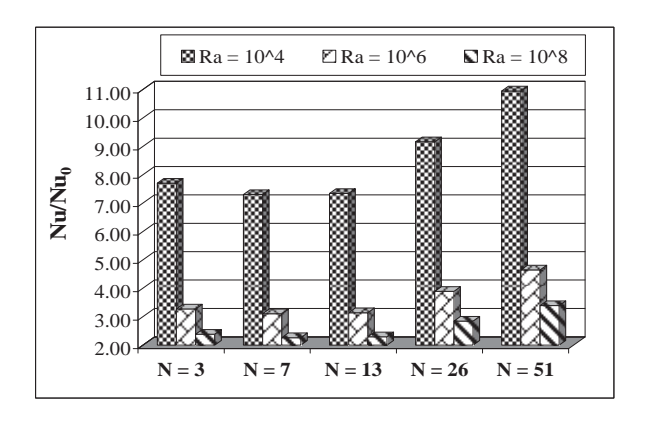


Fig. 5.47 Effect of number of electrodes to the heat transfer augmentation ( $V_0 = 17.5 \; kV$ ).

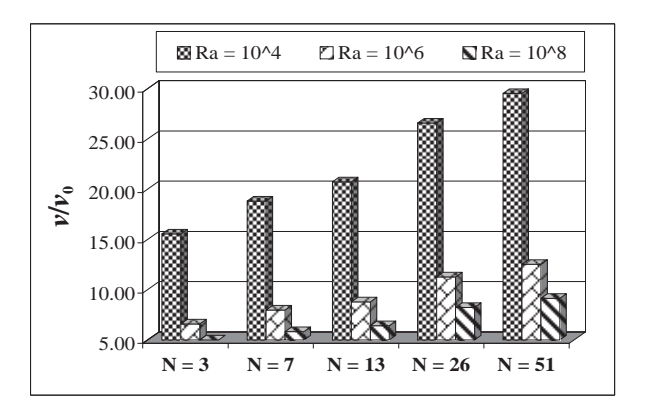


Fig. 5.48 Average velocity enhancement for various numbers of electrodes ( $V_0 = 17.5 \text{ kV}$ ).

Fig. 5.49 investigates the stream function and isotherm line contours inside the cavities with multiple fins attached uniformly on the left plate ( $V_0 = 12.0 \text{ kV}$ ,  $N_f = 7$ ,  $N_e =$ 1,  $L_f = 0.25$ , and  $W \times H = 15 \times 15 \text{ cm}^2$ ): (a) Ra =  $10^4$ , (b) Ra =  $10^5$ , (c) Ra =  $10^7$ , and (d) Ra = 10<sup>8</sup> while the Rayleigh numbers is varied from 10<sup>4</sup> to 10<sup>7</sup>, in which the effect of Joule heating at the wire electrode is neglected. Since the Boussinesq approximation is adopted in this study, the energy equation does affect the momentum equation. For non-EHD, the fluid creates a clockwise rotating cellular motion. At low Rayleigh number, the strength of the primary vortex is weakened due to the fins obstruct movement of the fluid. This is because the convection not being strong compared with conduction and it has the most remarkable effects on the flow field when they are placed at the middle of the left plate. It appears that the stream lines become more packed with the increasing of Rayleigh number, thus, the fluid moves faster as natural convection is intensified. For applying EHD (an electrode is positioned at the center of enclosure), there is an effect of the secondary flow induced by the ionic wind at the wire electrodes, which causes two rotating cellular motions in Fig. 5.49(a). In next cases, where the Rayleigh number is increased further, fluid inside the enclosure is dominated by the effect of Rayleigh number instead of the electric field. The flow patterns are oscillated due to the interaction between the thermal buoyancy force and electrical body force. The thermal boundary layer is perturbed by the electric field when it extends over the recirculation region. It can be concluded that for low Rayleigh number, the flow and temperature fields have been substantially affected by the electric field. However, the effect of EHD is diminished at high Rayleigh number which can be indicated that no significant change in the heat transfer enhancement.

Fig. 5.50 conducts the flow and temperature fields with the multiple fins attached while the electrodes are placed at the middle (electrode strip is installed at the middle of enclosure in x direction and each electrode is positioned on the line of fin length in y direction), extreme (electrode strip is installed near the end of fin in x direction and each electrode is positioned on the line of fin length in y direction), top-extreme (electrode strip is installed near the end of fin in x direction and each electrode is positioned between the line of fin length in y direction), and top (electrode strip is installed at the middle of fin length in x direction and each electrode is positioned between the line of fin length in y direction) arrangements, respectively, in which the numbers of fins and electrodes are kept the same at seven ( $V_0 = 12.0 \text{ kV}$ ,  $R_0 = 10^6$ ,  $N_f = 7$ ,  $N_e = 7$ ,  $N_e = 7$ ,  $N_e = 10.25$ , and  $N_e = 10.25$ ,

fin length), (c) (x = 4.6875 cm, y is between the line of fin length), and (d) (x = 1.875 cm, y is between the line of fin length). It can be observed that the top arrangement positioned yields the multiple vortices which reduce the flow structure, while the extreme arrangement performs a maximum average velocity from the high velocity along the hot plate compared with other arrangements. For temperature field, it can be observed that the extreme arrangement still obtains the highest temperature gradient along the hot wall.

A non-equivalent number of fins causes different flow patterns to occur in the enclosure of Fig. 5.51 ( $V_0 = 12.0 \text{ kV}$ , Ra =  $10^6$ ,  $N_e = 1$ ,  $L_f = 0.25$ , and  $W \times H = 15 \times 15$ cm<sup>2</sup>): (a)  $N_f = 2$ , (b)  $N_f = 4$ , (c)  $N_f = 9$ , and (d)  $N_f = 15$ . It can be observed that the separation over the fin appears especially at the top zone of the enclosure. As seen that temperature gradient along the left plate of Fig. 5.51(a) is highest compared with other categories that may results in maximum heat transfer coefficient. In Fig. 5.52 ( $V_0 = 12.0$ kV, Ra =  $10^6$ ,  $N_f$  = 1,  $N_e$  = 2, and  $W \times H$  =  $15 \times 15$  cm<sup>2</sup>): (a)  $L_f$  = 0.0625, (b)  $L_f$  = 0.125, (c)  $L_f = 0.5$ , and (d)  $L_f = 0.75$ , the enclosure is divided in upper and lower zones which each zone has one electrode located at the center. The presence and the character of the primary clockwise rotating vortex is unaltered, with a longer fin bringing about more changes to the flow compared to a shorter fin. It is noticed that for  $L_f \ge 0.5$  (Fig. 5.52(b) and (c)), many recirculating vortices are found above the fin and under the top insulated wall. The longer fin has more remarkable effects on the flow fields. Comparing Figs. 5.52(a) and (b) along fin at most positions only changes the temperature distribution locally and the rest of the enclosure remains unaffected. This is because the primary vortex has not altered too much upon introduction of a short fin and the fin only changes the velocity distribution locally.

The average Nusselt number along the enclosures for various Rayleigh numbers is shown in Fig. 5.53 ( $V_0 = 12.0 \text{ kV}$ ,  $N_f = 7$ ,  $N_e = 1$ ,  $L_f = 0.25$ , and  $W \times H = 15 \times 15 \text{ cm}^2$ ). For non-EHD, placing fins on the left plate always reduces the heat transfer on the left plate. The average Nusselt number of the left plate becomes smaller with an increasing of the fin length due to the fins obstruct flow and also reduce convective strength. However, the effect of fins becomes less remarkable with the rising of the Rayleigh number because the primary flow is enhanced with compensate the effect of blocking by the fins. Thus, for high Rayleigh number, the flow field is augmented regardless of the length and position of fins. Therefore, it is found that EHD augmented flow and heat transfer play much important role at the low Rayleigh number region, and this phenomenon is consequently influenced at the high supplied voltage.